
Electronic Thesis and Dissertation Repository

4-19-2016 12:00 AM

A Novel Minimally Invasive Tumour Localization Device

Doran Avivi
The University of Western Ontario

Supervisor
Dr. Michael Naish
The University of Western Ontario

Graduate Program in Biomedical Engineering
A thesis submitted in partial fulfillment of the requirements for the degree in Master of
Engineering Science
© Doran Avivi 2016

Follow this and additional works at: <https://ir.lib.uwo.ca/etd>



Part of the [Biomedical Devices and Instrumentation Commons](#)

Recommended Citation

Avivi, Doran, "A Novel Minimally Invasive Tumour Localization Device" (2016). *Electronic Thesis and Dissertation Repository*. 3705.
<https://ir.lib.uwo.ca/etd/3705>

This Dissertation/Thesis is brought to you for free and open access by Scholarship@Western. It has been accepted for inclusion in Electronic Thesis and Dissertation Repository by an authorized administrator of Scholarship@Western. For more information, please contact wlsadmin@uwo.ca.

A Novel Minimally Invasive Tumour Localization Device

Doran Avivi

Master Thesis, 2016

Biomedical Engineering Graduate Program

The University of Western Ontario

Abstract

Lung cancer is one of the leading causes of death by cancer. The usual treatment is surgical resection of tumours. However, patients who are weak or have poor pulmonary function are deemed unfit for surgery. For these patients, a minimally-invasive approach is desired. A major problem associated with minimally-invasive approaches is tumour localization in real time and accurate measurement of tool–tissue forces.

This thesis describes the design, analysis, manufacturing and validation of a minimally-invasive instrument for tumour localization, named Palpatron. The instrument has an end effector that is able to support two previously designed jaws, one containing an ultrasound sensor and the other a tactile sensor. The jaws can move with two degrees of freedom to palpate tissue and rotate about the central axis of the instrument. The Palpatron has uncoupled jaw motion that allows for optimal alignment of sensors to improve data acquisition. The instrument can be easily assembled and disassembled allowing it to be cleaned and sterilized. The mechanism is articulated using push rods, each actuated by a motor. A semi-automatic control system was created for palpation. It is composed of a microcontroller that controls four motors via serial communication. In addition, the Palpatron has the ability to prevent tissue damage by measuring tool–tissue forces.

Finite element analysis was used to guide material selection for designed components. Grade 5 titanium was selected for end-effector links to provide a factor of safety of 1.2 against yielding under a 10 N point load at the tip of a jaw. The design was fabricated and validated by conducting experiments to test articulation and load carrying capacity. An 8-N force was applied to the instrument, which was successfully supported. The semi-automatic control system was used to perform basic maneuvering tasks to verify jaw motion capabilities. With positive testing results, the Palpatron forms the next step towards a comprehensive robotic-assisted palpation technology.

Acknowledgements

I would like to thank my supervisor Dr. Michael Naish for his continual help, support and guidance throughout my thesis project. He was always able to provide me with the necessary advice and input that ensured a steady progress throughout my project. I would also like to thank the University Machine Services for their assistance with manufacturing of the Palpatron. I would like to specifically thank Chris Vandelaar for assisting me with the manufacturing process and offering his knowledge and expertise which have tremendously helped my progress in the project. I could not have completed this project without the generous help of Ian Vinkenvleugel, Josh Taylor, and Clayton Cook who helped trouble shoot my numerous problems with the wire EDM machine and ensured an enjoyable working environment. I would also like to extend my gratitude to Paul Sheller and Stephen Mallinson at the Engineering Finance Stores for their help with processing my orders and other financial related matter. I would also like to thank the staff at the Electronics Shop who helped me with selecting electronic components for my prototype. I also thank the CSTAR team for their help and assistance, especially Abelardo Escoto for his great suggestions, and support since the start of my project.

A very special thanks goes to Ilia Tyker without whom I would not have been able to complete the control system for the Palpatron. I also thank Omar Fahmy for helping with the custom PCB design. In addition, I thank the financial support of the Natural Sciences and Engineering Research Council and Western University for my research.

Most importantly, I would like to thank my wonderful parents, my grandmother, my uncle, and my girlfriend, Anna Tyker. I cannot thank you enough for your love, support, and encouragement throughout my graduate studies. I could not have made it without all of you in my life.

Contents

Abstract	i
Acknowledgements	ii
Table of Contents	iii
List of Figures	vii
List of Tables	xii
Nomenclature and Acronyms	xiii
1 Introduction	1
1.1 Motivation	1
1.2 Current Treatment Technologies	3
1.3 Project Goals	5
1.4 Significant Challenges	6
1.5 Contributions	8
1.6 Organization of Thesis	9
2 Literature Review	11
2.1 Haptic Feedback	11
2.1.1 Kinaesthetic Feedback	12
2.1.2 Tactile Feedback	14

2.2	Grasper Instrument Designs	16
2.2.1	Manual Graspers	16
2.2.2	Articulated Wrist Graspers	17
2.3	Tumour Localization Instruments	18
2.3.1	Axially Palpating Instruments	18
2.3.2	Optics-based Instruments	21
2.3.3	Grasper-type Palpating Instruments	22
2.4	Robotic-Assisted Devices	23
2.5	Summary and Conclusions	27
3	Tool Design and Analysis	29
3.1	Design Requirements and Constraints	29
3.2	Design Specifications	30
3.3	Concept Selection and Evaluation	32
3.3.1	Articulated Wrist Design	32
3.3.2	Multiple Link Design	36
3.3.3	Support Shaft and Handle Design	45
3.3.4	Final Design	50
3.4	Finite Element Analysis and Material Selection	52
3.5	Machining Process	59
3.6	Conclusions	62
4	Electronics and Control System Design	64
4.1	Semi-Automated Control	64
4.1.1	Actuator Selection	64
4.1.2	Control Implementation	66
4.1.2.1	Hardware	66
4.1.2.2	Software	67
4.1.3	Quantifying Jaw Backlash and Hysteresis	71
4.2	Forward Kinematics	75

4.3	Inverse Kinematics	77
4.4	Conclusions	79
5	Prototype Testing and Validation	81
5.1	Experimental Setup	81
5.2	Load Carrying Capacity and Strain Measurement	83
5.2.1	FEA Model Validation	87
5.3	Palpation Abilities	89
5.4	Conclusions	92
6	Conclusions and Recommendations	94
6.1	Summary	94
6.2	Concluding remarks	95
6.3	Recommendations	96
6.3.1	Mechanical Design	96
6.3.2	Control System	97
6.3.3	Testing and Validation	97
	References	99
	Appendices	104
A	Diassembly Instructions	104
B	Finite Element Model Setup	109
B.1	Linkage FEA Model	109
B.2	Support Shaft FEA Model	112
B.3	Push Rod FEA Model	113
C	Derivations for Kinematic Equations	115
C.1	Forward Kinematics	115
C.1.1	Forward Kinematic Model Summary	119

C.1.2 Forward Kinematic Model Validation	120
C.2 Inverse Kinematics	123
C.2.1 Inverse Kinematic Model Validation	124
Vita	125

List of Figures

1.1	Deaths due to cancer and other causes in Canada.	1
1.2	MIS versus open chest surgery.	2
1.3	Types of lung cancer surgical resection.	3
1.4	Use of trocars in an MIS	4
2.1	Rosen <i>et al.</i> grasper system overview.	13
2.2	Laparoscopic grasper prototype, by Tholey <i>et al.</i>	14
2.3	An endoscopic grasper with a Babcock tip.	17
2.4	Driving mechanism of a wrist joint.	18
2.5	Tactile sensing probe with a 60-element pressure sensor at its distal end.	19
2.6	Overlaid tactile information onto endoscope footage.	21
2.7	Grasper-type palpating instrument design.	23
2.8	Tactile pin feedback.	25
2.9	Tissue stiffness distribution map.	26
2.10	Robotic setup for palpating tissue.	26
2.11	Force-feedback-enabled minimally-invasive surgery instrument.	27
3.1	Coordinate system for wrist motion.	32
3.2	Hooke joint structure.	33
3.3	Bevel and spur gear system design.	34
3.4	Previous design of twisting mechanism for the end effector.	35
3.5	Floating controls concept.	35

3.6	Ideal grasping orientations.	37
3.7	Hybrid cable–push–rod link mechanism.	37
3.8	Close up view of rollers and jaws.	38
3.9	Improved linkage mechanism.	38
3.10	Linkage mechanism with an extended support shaft.	39
3.11	View of linkage mechanism with shaft transparent.	39
3.12	Linkage mechanism with intermediate link supports.	40
3.13	Detailed view of linkage mechanism with supports.	40
3.14	Final jaw linkage design.	41
3.15	Linkage actuation mechanism with push rods.	42
3.16	Exploded view of jaw linkage components.	42
3.17	Maximum parallel jaw opening.	43
3.18	Maximum jaw opening.	43
3.19	Jaw tilt at a fully opened position.	43
3.20	60 degree jaw sweep.	44
3.21	Single jaw motion.	44
3.22	Support shaft components: base, sleeve and top cover.	45
3.23	Support shaft connection to handle.	46
3.24	Quarter turn sleeve design.	46
3.25	Rear view of quarter turn design.	46
3.26	Push rod guide set up.	46
3.27	Guide cross-section.	47
3.28	Motor and lead screw assembly at the proximal end of the tool.	47
3.29	Push rod keyway covers.	48
3.30	Push rod keyways with covers removed.	48
3.31	Keyway access slots in the base of the support shaft.	48
3.32	Mounting of motors.	49
3.33	Instrument handle with controls.	50
3.34	Instrument handle attachment mechanism.	50

3.35 CAD render of final tool design.	51
3.36 Linkage mechanism prototype, scaled in size by a factor of four.	51
3.37 FEA model of jaw with a 10 N load.	52
3.38 FEA stress results at a 40 degree jaw opening.	53
3.39 Close up of FEA at a 40 degree jaw opening.	53
3.40 Close up of FEA at a minimum jaw opening.	54
3.41 FEA model of jaw with a 10 N side load.	54
3.42 Side load FEA results.	55
3.43 Side load FEA results with a modified stress map scale.	55
3.44 Reaction forces from SolidWorks.	57
3.45 Results from FEA on support shaft. The top cover, base and sleeve are combined into one part.	57
3.46 Results from FEA on push rods.	58
3.47 Results from FEA on pins.	59
3.48 CNC mill machining a link.	60
3.49 Lathe setup for machining tool support shaft.	60
3.50 Small links machined with wire EDM.	61
3.51 Jaw holder machined with wire EDM and CNC mill.	61
3.52 Machined keyway and key.	61
3.53 Wire EDM setup.	62
4.1 Jaw control sequence.	69
4.2 Custom printed circuit board layout.	71
4.3 Shaft and jaw deflection measurement setup.	72
4.4 Jaw deflection measurement setup.	72
4.5 Captive pins that hold the sleeve of the instrument.	73
4.6 Effects of jaw load on angular position of the jaw.	74
4.7 Sideways jaw loading setup with an inwards applied load.	75
4.8 Coordinate system for jaw mechanism.	76

4.9	Kinematic model of jaw mechanism.	76
4.10	Detailed kinematic model of jaw mechanism.	77
5.1	Strain gauge locations.	82
5.2	Experimental setup for strain measurements.	82
5.3	Scatter plot of strain at incremental loading conditions for Gauge 1.	84
5.4	Strain reading from P3 at incremental loading conditions for Gauge 2.	84
5.5	Link configuration and asymmetric jaw design.	85
5.6	Strain readings from Gauge 1 with incremental side loads on the jaw.	86
5.7	Strain readings from Gauge 2 with incremental side loads on the jaw.	86
5.8	FEA strain results from applying a normal load of 7 N.	87
5.9	FEA strain results from applying a side load of 4 N.	88
5.10	Effects of mesh refinement on stress singularities.	89
5.11	Jaw lifting a 700 g mass.	90
5.12	Squeezing of a rubber ball to 4 N.	90
5.13	Grasping a wood wedge with a declining slope.	91
5.14	Slot and wooden block.	91
5.15	Grasping a wood wedge with an inclining slope.	91
A.1	Tool in operation mode.	104
A.2	Tool with jaws closed.	104
A.3	Removal of set screws located at distal end of tool.	105
A.4	Removal of sleeve retainer.	105
A.5	Rotation of sleeve.	106
A.6	Sleeve at a slight offset.	106
A.7	Sleeve rotated so that wires are covered.	106
A.8	Removal of sleeve.	107
A.9	Top cover is removed to allow removal of keyways.	107
A.10	Keyway covers removed by sliding.	107
A.11	Removal of keys.	107

A.12 Disassembled device.	108
B.1 Lateral load applied to jaw.	110
B.2 Normal load applied to jaw.	110
B.3 Main pin constraints.	111
B.4 Push-rod links constraints.	111
B.5 Pin constraints that prevent lateral movement of the pins during simulation.	112
B.6 Fixture location on the support shaft used in FEA.	112
B.7 Load direction and location on the support shaft.	113
B.8 Location of guides along the push rod.	113
B.9 Location and direction of loads applied to the push rod in the FEA.	114
C.1 Coordinate system for jaw mechanism.	115
C.2 Kinematic model of jaw mechanism.	116
C.3 Detailed kinematic model of jaw mechanism.	116
C.4 Graphical solution in SolidWorks.	121

List of Tables

3.1	Summary of DOF available in state-of-the-art hand-held palpation and grasper devices.	31
3.2	Design specifications and targets derived from design requirements.	31
4.1	Joystick control summary.	70
4.2	Summary of variables and constants that can be used to solve the kinematic equations.	78
5.1	A comparison of tool performance to design targets.	93
C.1	Summary of variables and constants that can be used to solve the kinematic equations.	120
C.2	Summary of constants and variables used in kinematic model validation.	122
C.3	Range of angles and push rod positions.	122

Nomenclature and Acronyms

Acronyms

2D	Two-Dimensional
3D	Three-Dimensional
CAD	Computer Aided Design
DC	Direct Current
DOF	Degrees of Freedom
GUI	Graphical User Interface
MIS	Minimally Invasive Surgery
OS	Operating System
PC	Personal Computer
PCB	Printed Circuit Board
PIC	Programmable Interface Controller
PVDF	Polyvinylidene Fluoride
qc	Quadrature Counts
rpm	Revolutions Per Minute
SS	Stainless Steel

Greek Letters

θ An angle between linkages

θ_h Desired angle of palpation

Latin Letters

l	Length of a link
h_1	Desired thickness of palpation
$h_{1,x}$	Desired horizontal position of jaw midpoint

Chapter 1

Introduction

1.1 Motivation

Two in five Canadians develop cancer within their lifetime. Cancer accounts for 30% of deaths in Canada every year (Figure 1.1), and of all such deaths, lung cancer accounts for a quarter and is the leading cause of death by cancer. It is estimated that about 196,000 Canadians developed cancer in 2015, and that 78,000 of those died of cancer, a slight increase from 2014 and consistent with the increasing trend of lung cancer deaths over the years. In both sexes, lung cancer is responsible for 27% of the premature deaths caused by cancer [1].

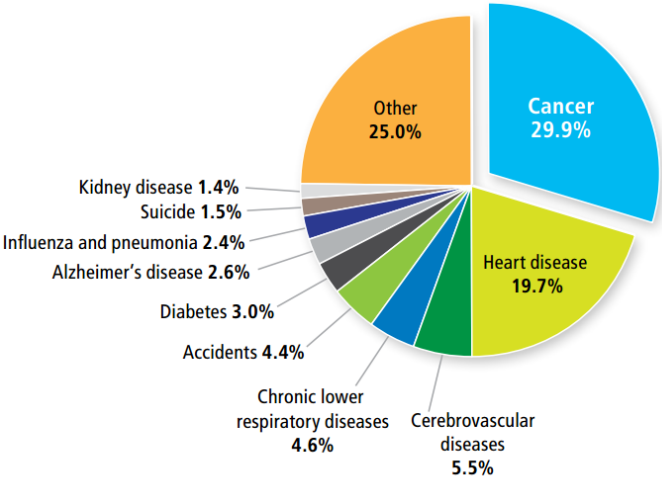


Figure 1.1: Proportion of deaths due to cancer and other causes in Canada in 2011 [1].

When a patient is diagnosed with lung cancer, surgical resection of the entire lung or lobe is often the treatment of choice. However, many patients who are weak or have poor pulmonary function are deemed unfit for surgery, particularly with conventional open-chest procedures [2] (Figure 1.2). Open surgeries and complete lobe or lung resection are associated with high morbidity and reduced quality of life. Preserving lung function and reducing the trauma of open-chest surgery can be accomplished by using minimally-invasive techniques that use a number of small incisions, long slender instruments, and a camera to visualize internal structures. MIS remains a technically challenging procedure as accurately locating tumours and identifying their size is often difficult in real time.

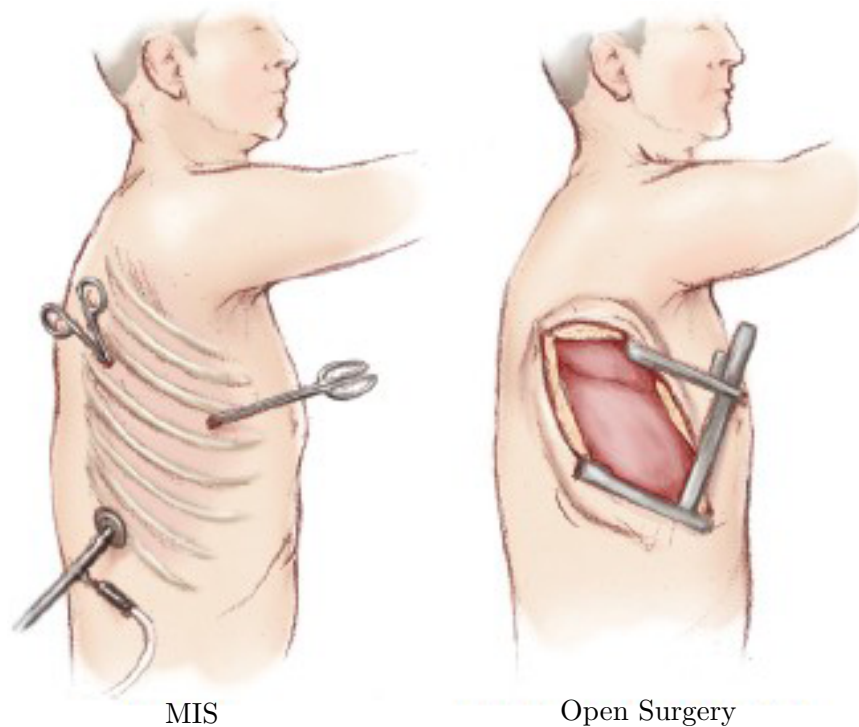


Figure 1.2: MIS versus open chest surgery [3].

Imaging techniques such as magnetic resonance imaging or computed tomography scanning are crucial for identifying the presence of lesions preoperatively. During open surgery, the surgeon relies on direct palpation of the tissue to confirm tumour location and size [4]. Tumours are commonly stiffer than the surrounding tissue, which allows for easy identification. However, during MIS the positions of tumours often change with respect to the pre-operative scan due to tissue shift from

lung collapse in addition to respiratory and cardiac motion. The conditions for identifying tumour locations and consistency are worsened by the inability to directly palpate tissue due to the small size of the incisions, typically 5 to 12 mm wide. Instead, minimally-invasive instruments are used to probe the surface of an organ to determine the position and size of a tumour.

1.2 Current Treatment Technologies

The most common treatments for lung cancer are surgical resection (Figure 1.3), chemotherapy, radiation therapy, brachytherapy, ablation therapy and photodynamic therapy [5]. Most cancer therapies often combine two or more treatments. However, the focus of this thesis is on the localization of tumours during surgical resection. Since tumours differ in their consistency from the surrounding healthy tissue, tumours can be identified with relative ease during open surgery. Since some patients are deemed unsuitable for extensive surgeries, they require MIS.

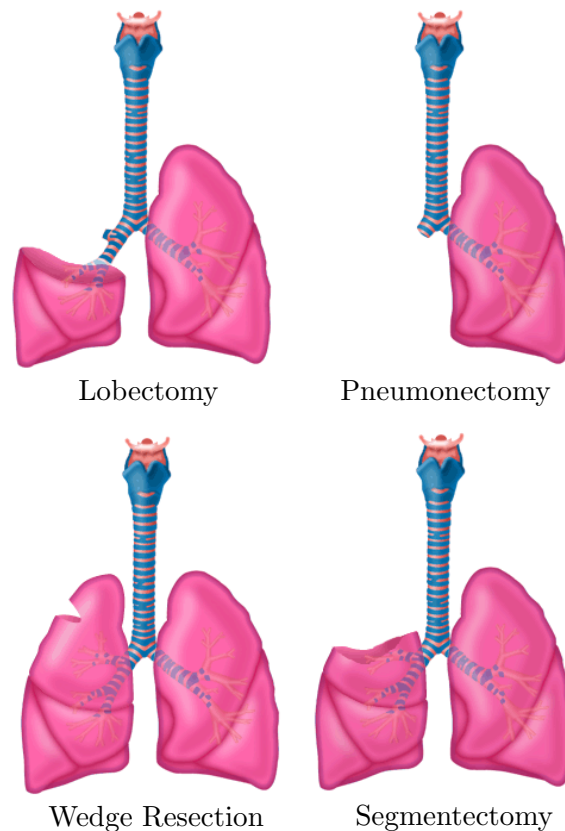


Figure 1.3: Types of lung cancer surgical resection [6].

MIS requires the surgeon to create a number of small incisions used to provide access for hand operated surgical tools to the internal organs of a patient. The surgical tools are composed of long slender rods equipped with cameras and graspers to provide surface visualization of internal structures and to excise tumours. Some minimally-invasive instruments are also equipped with sensors that are able to provide partial haptic feedback to the user. Haptic feedback will be discussed in more detail in Chapter 2. Although there are many benefits to MIS over open surgery, palpation under MIS conditions is inherently difficult to perform due to complex instrument movement, a lack of direct vision of the surgical area, a loss of tool–tissue force perception due to friction and elastic effects of the tissue at the trocar (Figure 1.4), and the complete loss of touch. A standard Babcock grasper can be used to palpate tissue. Using the grasper, the surgeon can attempt to determine tissue stiffness by feeling the force exerted on the instrument handle, or by visually inspecting the tissue via an endoscopic camera. However, if the surgeon palpates too hard with the instrument, it can lead to permanent tissue damage.

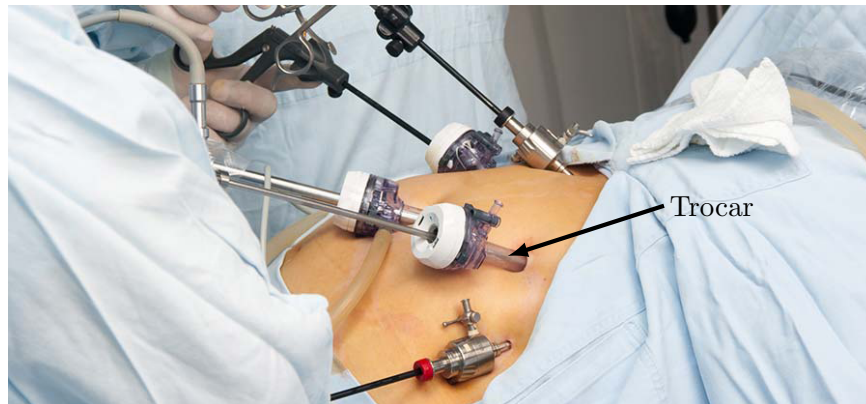


Figure 1.4: Use of trocars in an MIS, modified from [7].

Several minimally-invasive instruments have been developed to assist with tumour localization. Most recent work involves the use of capacitance– or piezoresistance–based sensors placed on a hand operated instrument composed of a long slender rod that, in some cases, is equipped with small jaws that can rotate in one direction. Such instruments are able to measure the applied pressure distribution on tissue, and help identify irregularities in the tissue [8]–[9]. However, the limitations of these instruments lie in the difficulty of applying consistent pressure to the tissue and measuring it, which are required to properly identify tumours.

Current minimally-invasive instruments are significantly inferior to direct manual palpation and can result in tissue damage. Experiments involving tissue palpation that were conducted with and without force feedback and have shown that excessive palpation forces are often applied when no force feedback is available [9]. Incorrect tumour detection is another issue that arises from inaccurate force feedback because it is difficult to differentiate tumours from other hard underlying tissue or bone without direct human palpation. As a result, in some cases, the conversion to open surgery is required to minimize internal tissue damage and allow for tissue palpation by hand. Furthermore, these approaches, in relation to lung cancer, remain technically challenging for accurate tumour localization and in particular for precise determination of its 3D size and consistency. Therefore, there is a need for a minimally invasive tool that can mimic manual palpation and provide accurate information about tumour location and morphology. Such an instrument will greatly improve current minimally invasive tumour treatments, minimize post-operative morbidity and improve patients' quality of life. The problems presented here have inspired much of the ongoing research today into improved MIS instruments and has motivated the design of the tumour localization device presented in this thesis, named the Palpatron.

1.3 Project Goals

The objective of this research is to develop and validate a hand-held instrument for use in minimally-invasive cancer surgery and therapy that enhances currently available minimally-invasive approaches. The proposed device integrates specialized mechatronic tools, tactile data, ultrasound images and tool-tissue interaction forces in order to localize tumours and visualize tumour structure in real time by palpating tissue. It is expected that by using the proposed sensing modalities, a surgeon's natural sense of touch can be mimicked under MIS conditions.

By building a fully functional prototype of the tool, the feasibility of using the proposed instrument in a clinical setting can be evaluated and serve as a starting point for future developments. The prototype will be designed and constructed to meet the size and performance constraints associated with operation in minimally-invasive surgical environments. The focus of this work will be on the lung, however, its use can be extended to other soft tissues. The instrument will also

incorporate improvements to a previously developed minimally-invasive palpation instrument that used resistance-based force sensors to automatically control two jaws with the goal of localizing tumours [10]. This work will include the design, development, manufacturing, and testing of the mechanical components and mechanisms necessary for a fully functional prototype. It will also include the selection and integration of actuators and the development of a control system necessary for proper tool operation. The proposed device has two jaws, each with two DOF of jaw movement, in addition to a third rotational DOF about the longitudinal axis of the instrument. The jaws are detachable and are equipped with ultrasound and tactile sensors. Jaw motion is controlled by motors that are housed in the handle of the instrument. The tool is also able to provide kinaesthetic feedback using strain gauges that measure tool-tissue interaction forces.

1.4 Significant Challenges

One of the main challenges associated with designing tools for MIS is the size constraint. The tools need to fit through a 12-mm diameter hole, if not smaller. The size constraint complicated many aspects of the design, especially manufacturing and material selection. A small hole diameter required components to be small and limited the thickness of the links that support the tool jaws to a range of 0.8 to 1 mm. The loads being supported by the links were very high as compared to their thickness and required very strong materials. It was a challenge to design parts that meet the size and strength requirements while using materials that are readily available in the market. The small size of the links also complicated the fabrication and assembly process of the design prototype as size tolerances became very significant. The designed parts needed to be machined very accurately, thus increasing construction and manufacturing time. Ultimately, the inability to meet the required tolerances during the fabrication process caused significant jaw backlash and play in the prototype.

The size constraint also made it a challenge to provide room for electrical wires to pass through the main shaft of the instrument. Sensors on the jaws required electrical wires to pass from the handle to the jaws of the instrument. Push rods used to actuate the jaws further constrained the amount of space available for wires. It was also challenging to fit the push rods, wires and the links

within the 12-mm shaft while maintaining double shear on components of the mechanism. Double shear is important as it prevents bending of components under heavy loads. Although space was limited, the designed mechanism still functioned accurately.

Another main constraint in the design required the use of previously designed jaws. Since the jaws could not be changed, it was difficult to incorporate them into the new design, and this led to a very mechanically disadvantageous jaw actuation mechanism. Modification of the jaws to account for better load distribution would greatly improve the functionality of the design. Currently, forces from the jaws are magnified tenfold due to the nature of the jaw design. This configuration inevitably increased the stresses at the motors and the links supporting the jaws.

Furthermore, the ability to sterilize and clean the end effector of the instrument was a key requirement for the design. Sterilization techniques were hard to implement due to the need for a mechanism that allowed the instrument to be sterilized without taking the entire tool apart. To combat this problem, a quick-release mechanism was implemented at the proximal end of the instrument. The quick-release mechanism allowed for easy assembly by reducing the number of assembly components, thus reducing assembly time. Unfortunately, this mechanism proved to be difficult to design as it required the removal of most mechanical fasteners.

Aside from mechanical design issues, creating reliable controls for the device was also a challenge. Several months were spent implementing serial communication between a PIC and EPOS2 motor controllers. A PIC is a programmable microcontroller that is able to process signals from an external source, interpret the data, and relay information to the EPOS2 controllers that control the motors of the instrument. The implemented communication algorithm is not perfect due to bugs in the code that resulted in timing out of the serial communication and loss of instrument control.

In order to allow for the future implementation of automated jaw control, the forward and inverse kinematic equations for jaw motion were derived. Due to the complexity of the actuating mechanism geometry, it was impossible to apply theories for simple robotic end effectors to the designed mechanism. Complex mathematical equations were derived instead, which could not be simplified enough to create closed form equations. The derived equations may prove to be a problem in the future as they can only be numerically solved, possibly causing delays in instrument

control.

1.5 Contributions

The device presented in this paper establishes one of the first steps towards a comprehensive device that is able to accurately and effectively palpate tissue and localize tumours. This project builds on previous work to create a device that is easier to use and manufacture, is sterilizable, can provide haptic feedback, and has independent jaw movement. The innovations in the proposed design are further explained below:

Ease of use: The handle of the instrument is equipped with floating joysticks that are able to rotate around the handle of the instrument. This ensures constant alignment of instrument controls with the user's hand.

Assembly & Manufacturing: The Palpatron is designed to be easily assembled and disassembled, something that was not considered in previous minimally-invasive tool designs. The instrument has very few mechanical fasteners; the only mechanical fasteners are between the tool's motors and their mounts, all other parts are fastened together using pins, keyways and clips. In addition, parts were simplified so that basic manufacturing methods can be used, making it easier to create accurate parts and improve tool precision.

Sterilization: This is the first minimally-invasive palpator that incorporates both ultrasound and haptic feedback, and has the ability to be easily disassembled so that parts of the instrument in contact with live tissue can be sterilized and cleaned without the need to take the entire instrument apart.

Haptic Feedback: The Palpatron has the ability to measure tool-tissue forces in a linear manner that can be combined with tactile data to provide the user with better tool control. Knowing tool-tissue forces ensures optimal palpation results from sensors and can reduce tissue damage.

Dexterity: The Palpatron is the first minimally-invasive device in which independent jaw movement is implemented. Independent movement allows for better alignment of the end effector with

tissue, and produces better data readings by allowing more of the surface of jaw-sensors to be in contact with tissue. Independent motion also provides the user more freedom to manipulate and palpate tissue.

1.6 Organization of Thesis

This thesis is divided into six chapters that progress through the design, analysis and validation of the Palpatron. A description of each chapter follows below:

Chapter 1 Introduction: This chapter presents the scope of the project and the motivation behind the presented work. Some of the current treatment technologies and their downfalls are presented. The challenges and contributions of the work are also outlined in this chapter.

Chapter 2 Literature Review: This chapter presents research on minimally-invasive surgical tools and tumour localization devices. This chapter is divided into three sections, each exploring prior literature regarding specific topics: haptic feedback, grasper instruments and robotics-assisted devices. The advantages and disadvantages of current and past technologies are presented and discussed. Throughout the literature review, mechanical designs are described and evaluated based on their advantages and disadvantages.

Chapter 3 Tool Design and Analysis: The design and manufacturing process of the prototype is described in this chapter. This chapter starts by presenting the design requirements and constraints and then presents the concepts that were generated from the design requirements. Next, the final design is presented and discussed. Each main component of the design is explained and the design choices behind each component are described. A thorough description of the finite element analysis performed on the most relevant parts of the system is presented together with justifications for materials selected for the components of the device. Finally, the manufacturing process of a prototype is briefly described.

- Chapter 4** Electronics and Control System Design: An overview of the electronic components, such as the motors and microcontrollers, is provided. A brief description of the software developed for manual control of the device is also presented. The requirements for the selection of the actuators and microcontrollers are described. Next, tool backlash and hysteresis are analyzed and quantified. Lastly, the forward and reverse kinematics equations for the end effector are derived.
- Chapter 5** Prototype Testing and Validation: In this chapter, the testing methods for the design and test results are presented. The test results are used to validate the FEA model created in Chapter 3. In addition, the load carrying capacity and the palpation abilities are tested.
- Chapter 6** Conclusions: This chapter summarizes the work presented in this thesis and offers recommendations for modifications and improvements to the current design to bring it to its full potential.

Chapter 2

Literature Review

This chapter explores current technologies for minimally-invasive tools that have been designed for tissue palpation and manipulation. The review will focus on mechanical design and feedback methods of various minimally-invasive surgical instruments.

2.1 Haptic Feedback

With the advancement of surgeries towards minimally-invasive techniques, the sense of touch has been lost due to the use of slender graspers and tools instead of the surgeon's hands. While using traditional minimally-invasive tools, the surgeon loses almost all haptic perception of the manipulated tissue. Most importantly, the perception of tissue stiffness is lost [11], and perceived forces are misleading as they are heavily influenced by friction and backlash within the instrument and the trocar [12]. Mimicking human finger sensation, in an intuitive manner, has been a challenge for many years.

Haptic feedback can be described as the human's sense of touch. Haptic feedback is divided into two categories of sensation: tactile and kinaesthetic feedback [13]. Haptic feedback is important as it can allow surgeons to determine tissue properties without physical manipulation, thereby allowing the surgeon to differentiate between healthy and unhealthy tissue. In addition, when it comes to identifying tumours, lumps or other texture abnormalities, such features cannot be identified via visual feedback alone. Most importantly, unnecessary damage to tissue can be

prevented with accurate tool–tissue force feedback [14].

2.1.1 Kinaesthetic Feedback

Kinaesthetic feedback deals with calculating the sum of forces applied to the end effector of an instrument. Various instruments have been designed to facilitate this type of measurement by placing strain gauges and other sensors along an instrument's shaft and links. In kinaesthetic feedback, forces are measured indirectly; sensors do not come in direct contact with the area of palpation. Forces are estimated based on signals generated by the deformation of the instrument during operation. One of the first designs that incorporated kinaesthetic feedback is a modified Babcock grasper by Bicchi *et al.* [11]. This tool employed a strain gauge mounted near the handle of the instrument to sense grasping forces. However, the position of the strain gauge caused severe nonlinear friction effects and the tool had backlash that prevented it from providing accurate force readings.

In later years, Rosen *et al.* [15] demonstrated the ability of a grasper with force feedback to restore some of the sense of touch that is lost during minimally-invasive surgery (Figure 2.1). The researchers conducted comparative tests between a standard Babcock grasper, a motorized Babcock grasper, and a gloved finger. The motorized grasper was a 1-DOF system that is controlled by a master–slave system. The master is controlled by the user and the slave gets corresponding commands from a computer. This device was one of the first to successfully implement haptic feedback and was able to apply a peak compressive force of 8 N. The master controller module conveyed the forces detected by the grasper to the hand of the user. Forces were calculated based on motor currents. As the jaws gripped tissue, an actuator at the master controller resisted motion. The results of this study showed that devices with force-feedback were significantly better than the standard grasper at determining tissue stiffness, but not as good as a gloved hand [16].

Rosen *et al.* [17] later created a second generation of their motorized grasper which was able to apply a grasping force of up to 26 N and weighed only 700 g. The new design used a brushed DC motor to drive the Babcock grasper through a pulley system. Range of motion for the Babcock jaws was 54.3 degrees, with a resolution of approximately 0.0113 degrees per encoder count. When fully opened, the two grasping surfaces were 26.3 mm apart. The new design also incorporated

a double-beam planar force sensor that was mounted within the pulley system. The device was computer controlled using a PID position controller, and the entire device was able to fit through a standard 10 mm trocar.

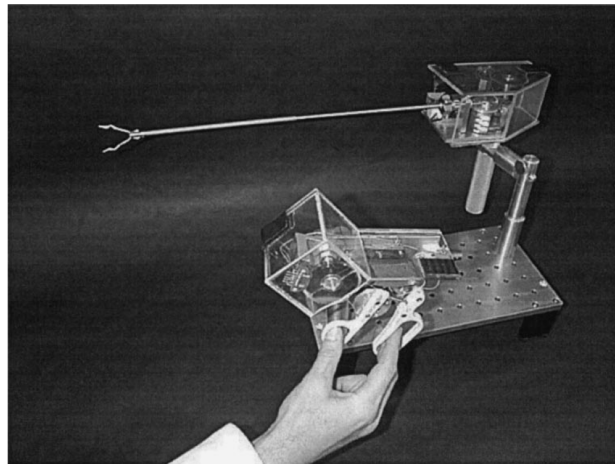


Figure 2.1: Rosen *et al.* grasper system overview © 1999 IEEE [15].

Elaborating on the work of Rosen, Dargahi *et al.* [18] took the Babcock grasper design one step further by providing the user with a visual form of force feedback. An array of light emitting diodes (LEDs) near the handle of the instrument lit up sequentially as the grasping force increased. Grasping forces were measured based on strain gauge sensors mounted on the back of the grasper jaws. This method reduced nonlinearities in force measurements experienced by researchers in the past.

Within the same year, Tholey *et al.* [19] revolutionized the grasper tool by creating a motorized, cable-driven grasping device with tri-directional force sensing capabilities (Figure 2.2). Their device had low friction and very small backlash. It used two piezoresistive sensors to measure lateral forces at the jaws of the device. A thin-film force sensor was used to measure normal forces, allowing for the measurement of shear forces on tissue. Knowing the forces in all three axes provides the user with the ability to identify tumours while sliding the grasper over a tissue sample. This device was also one of the few systems that integrated a closed loop control system and an automatic grasping function. The instrument demonstrated a high degree of accuracy when comparing actual probe forces to those measured by the jaws sensors. However, having bulky sensors mounted on the jaws and exposed wires prevented the tool from being suitable for minimally-invasive surgery.

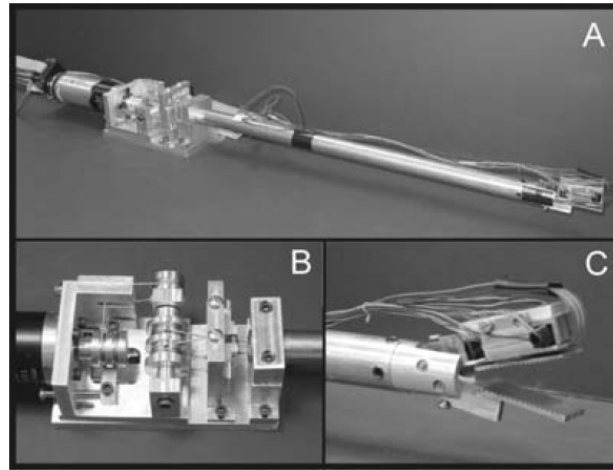


Figure 2.2: A) Laparoscopic grasper prototype, by Tholey *et al.*, consisting of a DC motor, cable-driven pulley system, and grasping jaws. B) Cable Tensioning mechanism. C) The end effector of the grasper; one jaw equipped with sensors and one without sensors [19].

From the research presented in this section, it can be noted that kinaesthetic feedback is efficient at sensing grasping forces but has nonlinear measurements. Implementing kinaesthetic feedback is problematic as it is hard to determine exactly how much loading is being applied to each jaw and whether or not each jaw is in fact fully contacting the tissue. Furthermore, bulk forces highly depend on tool design. For example, if jaws are used, calibration for bulk forces will depend on angular position of the jaws, which may require complicated calibration algorithms. On the other hand, tactile sensors can be used to simplify sensor calibration by being in direct contact with tissue. Tactile sensors can also be used to determine the underlying texture or shape of the palpated tissue.

2.1.2 Tactile Feedback

Kinaesthetic information is useful in minimally-invasive tumour localization techniques, but has inherent limitations, including the need to palpate tissue to similar depths in order to attain meaningful feedback. As was discovered by Yen *et al.* [20], palpation to a specific depth from the tissue surface followed by force measurement, detected changes in tissue stiffness more accurately than palpation to a predetermined force followed by depth measurement. The use of tactile sensors can mitigate many of the shortcomings of kinaesthetic feedback as well as provide more information regarding tissue structure. Tactile sensors are usually an array of pressure sensors that are able to

measure gradients in pressure across a surface. A pressure map can then be created that shows the stiffness distribution across the surface of the palpated tissue. Tactile feedback, unlike kinaesthetic feedback, pertains to the sensation of shapes and textures [13]. Various sensors have been developed including optical, elastomer, capacitive, piezoresistive, and polyvinylidene fluoride (PVDF) film based sensors. The main disadvantage with tactile sensors is their complicated manufacturing process for minimally-invasive surgery due to small size constraints [21].

One of the earliest tactile sensors designed was by Pawluk *et al.* [22]. They created a high sensitivity pressure sensor that was able to mimic the touch of a finger. The design used an array of perpendicular copper strips separated by thin pieces of silicone dielectrics. As pressure on the array increased, the capacitance of the array decreased. This sensor formed the basis for many of the tactile sensors available today. In later years, elastomer-based tactile sensors were also designed and proved suitable for minimally-invasive surgery [23]. However, the sensors were prone to hysteresis, creep, noise, and crosstalk. As a result, other materials, such as piezoresistive, were used instead [24].

Dargahi *et al.* [25] developed one of the first devices that incorporates tactile sensing. They developed a modified, minimally-invasive, surgical grasper equipped with PVDF as the sensing medium, which had four sensing elements. The sensor was placed on the jaws of a surgical grasper. The use of only four sensing elements made the design compact, strong, and relatively cheap. However, since there was no array structure, the device could only sense pressure changes in one dimension, which was a big limitation in this design. The ability to sense in two dimensions is crucial for efficient formation of pressure maps [25]. Similarly to Dargahi, Sedaghati *et al.*, [26] also attempted to develop a PVDF based tactile sensor for use in MIS. Their design used two sets of film that allowed for force sensing on a particular element of the array and the overall force on the sensed object. This provided a combination of tactile and kinaesthetic information. Unfortunately, the sensing elements were very fragile, and the size of their design made it unsuitable for MIS. In order to create a robust design, Schostek *et al.* [27] developed a sensor made up of an array of spherical electrodes. Although similar to pressure sensors, this sensor was waterproof and had comparable operating characteristics to the human finger. Through their experiments, they determined that their device could palpate and grasp with forces as high as 60 N.

Unlike previous designs, Roham *et al.* designed a tactile probe for measuring the modulus of elasticity of soft tissues [28]. The probe was constructed using a force sensing resistor and a polymeric film that decreased in resistance as the applied force increased. The group demonstrated that such a device has a performance comparable to industrial elasticity measuring machines. However, they did not test their device in an MIS environment.

These preliminary, basic tactile sensors and instruments presented in this section, opened the door for the design of tumour localization instruments that incorporate both tactile and kinaesthetic feedback.

2.2 Grasper Instrument Designs

Various instruments have been designed for the purpose of providing users with haptic feedback. Some designs incorporate manual actuation while others use motors to automate tissue manipulation during minimally-invasive surgery.

2.2.1 Manual Graspers

A range of manual, hand-held graspers have been designed. Many companies sell such instruments for commercial use. Most graspers have scissor-like handles that require physical input from the user to operate (Figure 2.3). Such graspers have a long slender shaft at the end of which two jaws are able to move in up to six degrees of freedom. Jaw movement is facilitated by push rods or cables. Single jaw movement is dependent on the position of the other jaw, thus jaws cannot move independently of one another. Such graspers have many physical constraints including restricted motion and fixed approach angles. While using manual graspers, the user also has a loss of depth and tactile perception [15].

Actuated graspers have also been designed to improve instrument handling. Mirbagheri *et al.* designed an actuated endoscopic grasper for manipulation of large internal organs [29]. The designed instrument is a small three fingered grasper. The instrument could pass through a 10 mm trocar and then be opened inside the abdomen to grasp body organs as large as 80 mm in diameter.

Unlike previously designed graspers, this grasper incorporated push rods for jaw actuation rather

than metal cables. Future work is still required to fabricate the device and evaluate its performance.



Figure 2.3: An endoscopic grasper with a Babcock tip [30].

2.2.2 Articulated Wrist Graspers

In order to improve tool control and reduce motion restrictions, several designs have been implemented to add wrist-like motion to MIS instruments. In 2004, Seibold *et al.* developed a gimbal joint system (Figure 2.4). This joint is bilaterally actuated by four cables in two DOF with 90 degrees of motion allowance. Their design also incorporated haptic feedback and a six DOF force-torque sensor based on a strain-gauge-instrumented Stewart platform. The sensor is suitable for MIS, and can be placed at the distal end of the instrument to directly measure tool-tissue interaction forces [31]. Meer *et al.* later proposed another compact wrist design for minimally-invasive surgery that uses small ball joints to allow motion in all directions. Their design ensured sufficient room for electronic wires, fiber optics and fluidic tubes to pass through the joint. The compact wrist is a generic concept that comprises of at least two vertebrae: plastic plates and balls. Metal wires drive the position of each vertebra which enable two DOF in any direction between -85 degrees and 85 degrees [32].

As an improvement to Meer's design, Berkerlman *et al.* designed a wire-driven flexible spine grasper. Unlike cable-driven rotational joints in the instrument wrists, the actuation method proposed by Berkerlman *et al.* is easier to fabricate and does not place actuation cables under

small bending radii. The articulated instrument provided two DOF in wrist motion and a single DOF for grasper actuation. Due to friction and hysteresis in the gripper actuation wire, they were not able to provide the user with stable and useful force feedback pertaining to gripping tasks [12].

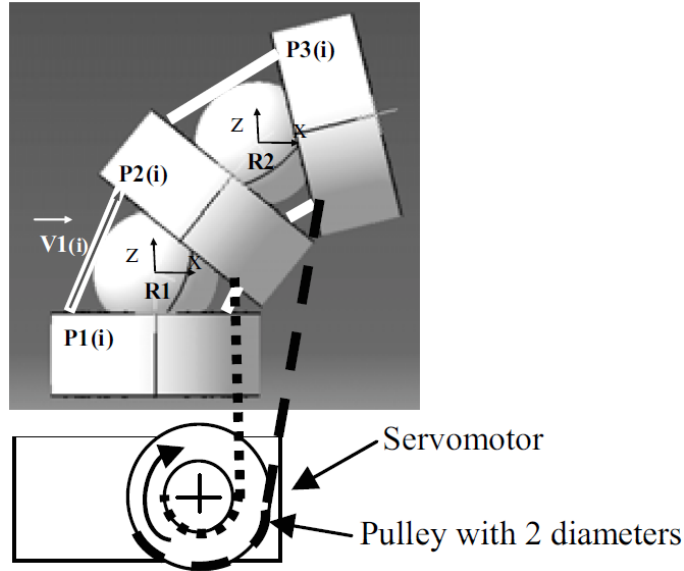


Figure 2.4: Driving mechanism of a wrist joint consisting of three servomotors and three pulleys © 2005 IEEE [32].

2.3 Tumour Localization Instruments

Tumour localization instruments combine kinaesthetic and tactile feedback to determine the location of tumours based on changes in tissue stiffness.

2.3.1 Axially Palpating Instruments

Axially palpating instruments are some of the simplest tumour localization instruments that palpate tissue in a one DOF motion. One of the first instruments designed, was a hand-held tactile probe that was used to identify tumours in breast tissue, called the Tactile Tumour Detector. The design used a force sensing resistor and was validated using phantom tissue. Experimental results were very similar to the results obtained from a finite element model [33].

In a separate study, Takashima *et al.* [34] designed an axially palpating instrument that can be attached to any endoscope. The attachment, an infrared filter, used image processing algorithms that allowed images to be converted into tactile forces. However, this design was not perfect as data processing was slow and prone to many sources of noise which made the instrument unreliable.

One of the most promising axially palpating instruments was designed by Perri *et al.* [35]. They designed a tactile sensing system, consisting of a probe (Figure 2.5) and a visualization interface for tactile feedback. Their system provided a real-time pressure map measured from the surface of tissue. They were able to locate tumours under MIS conditions with a 31% increase in accuracy as compared to an endoscopic grasper with no haptic feedback, manual palpation and an ultrasound transducer.

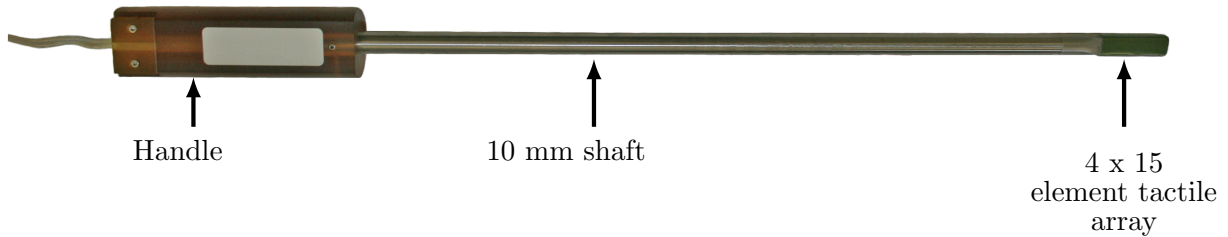


Figure 2.5: Tactile sensing probe with a 60-element pressure sensor at its distal end [35].

To improve the dexterity of axially palpating instruments, Miller *et al.* [36] designed a tactile sensing device with an articulated wrist. The device consisted of a capacitive array sensor mounted on a cylindrical minimally-invasive surgical probe with a rotational joint at its distal end. The joint was controlled by a knob and the additional DOF allowed for a wider range of palpation angles. The device was integrated with an endoscope to provide live video. Using optical tracking, tactile information was overlaid onto footage of the endoscope in the form of a pseudo-color map of the measured pressure distribution (Figure 2.6). The user could locate hard nodules in tissue by scanning the tactile device over the surface of a tissue and observing the spatial variation in contact pressures. Results from instrument validation indicated that, compared to using a rigid rod, subjects could localize lumps in lung phantoms more quickly and accurately. However, the performance of the designed probe depended heavily on the technique of the user, and it was discovered that there was significant damage to lung tissue post localization. Therefore, such a

tool would be unusable in practice.

Axial palpation of tissue is only feasible when there is a stiff backbone to support tissue palpation. For more complicated situations such as lung or thoracic surgery, tissue cannot always be palpated axially. Furthermore, the shape of the palpating probe can influence the measured tactile data, as demonstrated by McCreery *et al.* [13]. To attempt to address these shortcomings, grasper-like palpators and optical-based instruments have been designed.

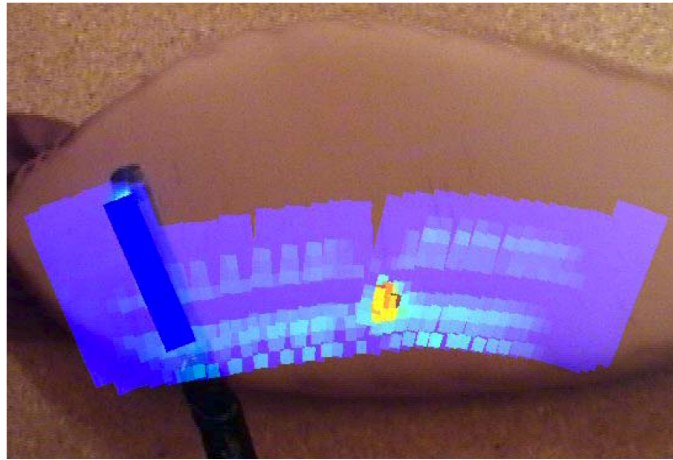


Figure 2.6: Overlaid tactile information onto endoscope footage. Yellow and red areas indicate an embedded lump © 2007 IEEE [36].

2.3.2 Optics-based Instruments

In 1983, a patent was filed for an ultrasound equipped endoscope. The ultrasound transducer was connected with links to the main endoscope shaft, creating a parallelogram joint. This provided the transducer with one rotational DOF, similar to the bending of the wrist [37]. Further improving the 1 DOF system, Cundari *et al.* [38] designed a device, similar to an axially palpating probe, which uses two stereotactic x-ray imaging transducer. The imaging transducers were hinged on the distal end of the instrument and were able to rotate in one DOF, similar to a grasper, but without coupled jaw movement. Tumour location was determined based on the angular position of the sensors. Although this device was designed to facilitate more efficient tumour biopsy procedures, its concepts can be extended toward tumour localization.

West *et al.* [39] designed one of the first optical-based tumour localization devices that incorporated tactile feedback. They mounted a tactile sensor oriented in the same direction as an

ultrasound transducer. The tactile sensor was composed of an array of pressure sensors, arranged along the outer perimeter of the ultrasound sensor. The pressure sensors provided a topographic view of the tissue, identifying the stiffness distribution of tissue while the imaging sensors provided a cross-sectional slice of the tissue. With the slices and topographic views, the tissue could be viewed in three dimensions. The only limitation of this instrument is that it was designed for palpating breast tumours, and is not directly applicable to MIS.

Further supporting the effectiveness of ultrasound at localizing tumours, Hyung *et al.* [40] showed how ultrasound can be used to identify tumours when they are too deep to palpate. The team researched a tumour localization technique that uses one endoscopic and one laparoscopic ultrasound transducers. The researchers were able successfully localize and remove two submucosal tumours in two human cases. Although this work was not conducted in a minimally-invasive environment and operated on non-palpable tissue, it shows how imaging techniques can help localize tumours. The effectiveness of ultrasound at localizing tumours has encouraged the development of palpating instruments that incorporate both haptic and visual feedback.

2.3.3 Grasper-type Palpating Instruments

Grasper-type palpators grasp tissue in a similar fashion to human fingers and provide the user with a better ability to manipulate tissue. To date, only one grasper-type tool, designed by Kurowski [41], has shown a strong potential for accurately localizing tumours. Kurowski designed a cable operated instrument that included an end effector with two DOF. The design also included an ultrasound transducer and a tactile sensor that allowed for the automatic palpation of tissue. Automatic control helps increase the accuracy of force feedback by ensuring sensor contact, and prevents tissue damage by uniformly distributing pressure onto tissue. The final design (Figure 2.7) can support a load of 20 N, over double the weight of an average human lung, with a factor of safety of four. Escoto *et al.* [42] later conducted *ex vivo* experiments with the designed tool. Tumour pathology was simulated by embedding iodine-agar phantom tumours of varying shapes and sizes into porcine liver tissue. The device was then used to palpate the tissue to localize and visualize the simulated tumours. Their results showed that the device localized 87.5% of the tumours with an average deviation of 3.42 mm from the tumour center.

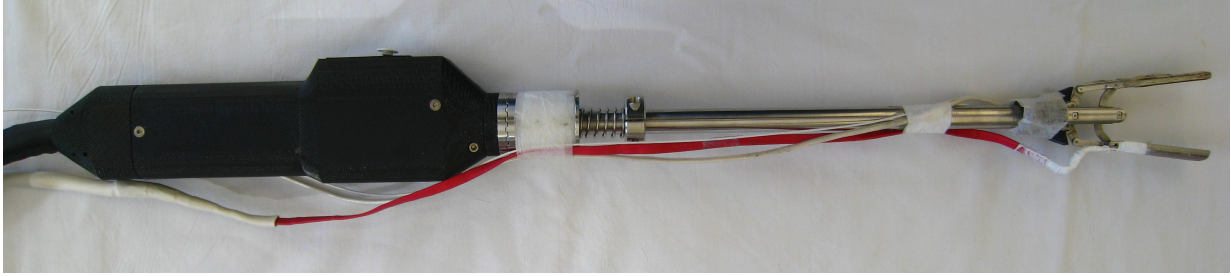


Figure 2.7: Grasper-type palpating instrument design by [10] and [42].

Similarly to the design by Kurowski, most actuated palpating instruments that exist today use cables to transmit motor movement to the end effector. Although not directly related to tumour localization, one of the few minimally-invasive tools found in literature that uses push rods is a design by Mauricio N. Leroy [43]. Mauricio designed a tool for needle guidance that uses push rods to control needle orientation and an ultrasound jaw. His design approach to jaw actuation can be extended to grasper-type palpator design.

2.4 Robotic-Assisted Devices

Several academic institutions have been developing robotic surgical systems that are able to provide the user with haptic feedback, such as the UW RAVEN II, the MIT Black Falcon, NASA-JPL RAMS system, the UCLA LapRobot [44]. However, only two systems have been approved by the FDA for clinical applications, the da Vinci and Zeus [45]. The da Vinci is an MIS robot composed of a master, a slave, and a control tower. The surgeon sits at an ergonomic workstation equipped with stereo video, which functions as the master. The master has hand controllers that are able to translate hand and wrist motions to the slave system. The slave is a large, heavy unit which sits next to the patient's bed. It has three to four arms that hold a variety of laparoscopic instruments. The end effectors are equipped with an EndoWrist[®], an articulated joint system that provides seven DOF. The standard da Vinci scopes and surgical instruments can pass through a standard 12 mm trocar [12].

Similarly, the Zeus platform uses an Automated Endoscopic System for Optical Positioning (AESOP). The AESOP was designed by Dr. Louis Kavoussi in 1994, and is the first FDA approved robotic surgical system with a voice controlled robotic arm. The robotic arm can be used to hold

and position laparoscopic instruments. The Zeus uses two additional units similar to the AESOP to grasp other surgical instruments and all three units are attached to the operating table. The surgeon is seated at a master, similar to the da Vinci. However, the Zeus has egg-shaped controllers that are not as intuitive or easy to use as the da Vinci controllers [12].

While using the da Vinci or Zeus, very minimal force feedback is available to surgeons. The user has no contact sensation from their hands and must judge any forces applied to tissue based on tissue deformation seen in video feedback or based on their surgical experience. In addition, these surgical systems are large and expensive and require the layout of operating rooms to be modified in order to accommodate them. Using such systems also increases surgery time as all parts of the robotic system must be enclosed in sterile drapes before each surgery. The large surgical manipulators partially obstruct access and visibility of the patient for surgical staff. In addition, training and specialized procedures are necessary for the setup and use of the systems. These systems mainly rely on actuation by cable tendons, which is their main source of weakness as the cables are prone to wear, stretching, and variable tension and friction [12].

With the advancement of haptic feedback technologies, many low-profile robotic-assisted platforms have been designed. Hu *et al.* [46] developed a robotic-assisted master–slave grasper with real-time tactile feedback that is relayed through a PHANToM haptic interface device (Sensable Technologies, Woburn, MA). Strain gauges on the instrument grasper were used to sense the grasping force. Experiments proved that feedback solely from strain gauges was sufficient to determine tissue stiffness. Although this design makes strides towards a comprehensive tumour localization device, it lacks tactile sensors which are required to achieve accurate and comprehensive palpation feedback.

In contrast, Feller *et al.* [47] used a capacitive tactile sensor to attempt to implement haptic feedback in a robotic-assisted device. They attempted to provide the sensation of palpation on the user’s finger by using an array of densely packed, vertically moving pins (Figure 2.8). The displacement of the pins was proportional to the sensed tactile pressure. The tactile sensor was mounted to a robotic arm that was tele-operated by one hand through a PHANToM. The other arm was used to feel the haptic feedback with one finger. Results from the experiment showed that this setup can accurately localize tumours. However, the tests were not conducted under MIS

environments nor does the design meet MIS size constraints. Within the same year, Ottermo *et al.* [48] were able to design a device that consolidated the tactile feedback and tool control into one unit. The device developed by Ottermo *et al.* was a remote palpation device that used a 30 element piezoelectric tactile sensor and a tactile display array at the master controller. This design eliminated the need to use two hands to control and feel, as was previously required.



Figure 2.8: Tactile pin feedback © 2004 IEEE [47].

A different approach to tactile feedback was later explored by McCreery *et al.* [13]. They designed a rod attached to a force-torque sensor (ATI Industrial). The rod was used to axially palpate tissue by mounting it to a Mitsubishi PA10-7C robot. It was determined that a peak palpation force of 1.6 N occurred when palpating to constant depths. In order to improve the axially palpating probes, Liu *et al.* designed a probe with a roller at its distal end [49]. This allowed the probe to roll over the tissue, facilitating an easier method for the formation of a force map to determine tissue stiffness distribution (Figure 2.9).

In an attempt to evaluate the performance of tactile probes, Trejos *et al.* [50] used a commercially available tactile sensor to determine its ability at creating texture profiles of tissue. Their experiments showed that under robotic-assisted palpation (Figure 2.10), the maximum pressure of palpation decreased by 35% and the frequency of successful tumour localizations increased by 50% when compared to manual palpation. Their work also identified that the optimal applied force for robotic-assisted palpation is 4 N, when a sensor area of 240 mm² is used. Their results showed that tactile data is highly dependent on the applied force, and the ability of an instrument to apply a consistent palpation force greatly affects its tumour localization performance. Therefore, automated palpation would increase the accuracy and reliability of tumour detection [50]. The use

of tactile feedback alone to localize tumours has shown to be successful, but the combination of kinaesthetic and tactile feedback are still necessary to accurately represent the touch sensation.

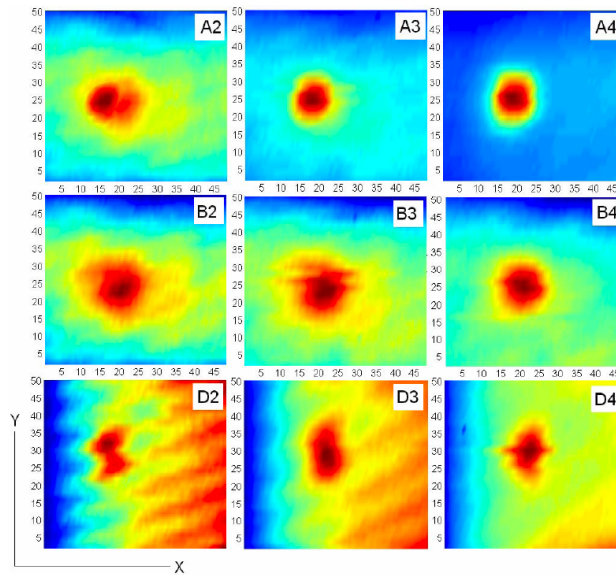


Figure 2.9: Tissue stiffness distribution map © 2008 IEEE [49].

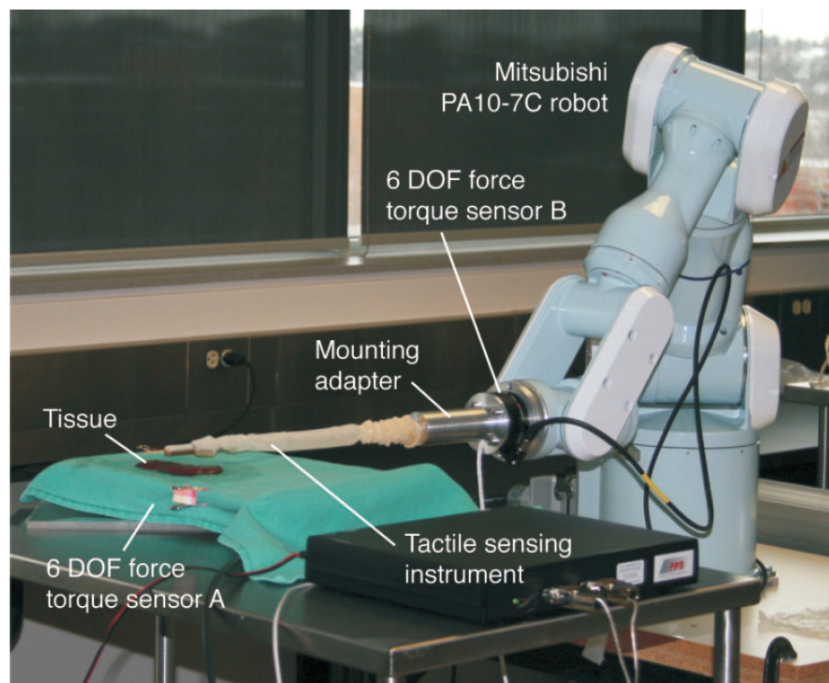


Figure 2.10: Robotic setup for palpating tissue [50].

Although not directly related to tumour localization, a robotic-assisted grasper system with force feedback was designed by Dalvand *et al.* [51] that is able to measure normal grasping forces as well as lateral interaction forces without any sensors mounted on the tip jaws (Figure 2.11). The proposed instrument is also able to change the grasping direction during surgical operation using a gear train mechanism and is one of the few instruments to implement push-rod actuated jaws. Their experimental results verify the ability of their instrument to accurately measure grasping forces and characterize artificial tissue samples of varying stiffness. However, the sterilizability of the instrument and sensors need to be improved before the tool can be used in surgeries.

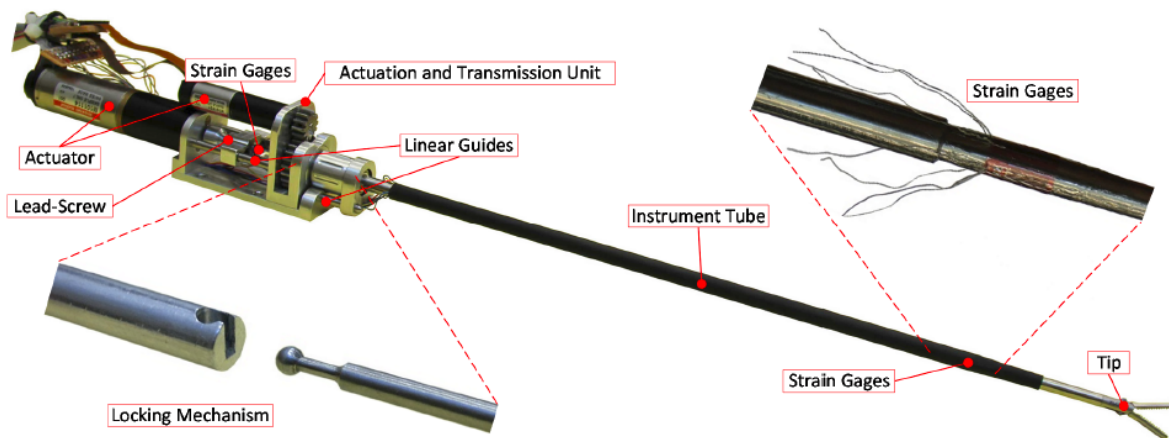


Figure 2.11: Force-feedback-enabled minimally-invasive surgery instrument © 2013 IEEE [51].

2.5 Summary and Conclusions

Several MIS instruments have been developed to assist with tumour localization. Most recent work involves the use of capacitive based sensors placed on a hand operated instrument composed of a long slender rod that, in some cases, is equipped with small jaws that can rotate in one direction. These instruments are able to measure the applied pressure distribution on tissue, thereby identifying any irregularities in the tissue. However, the limitations of these instruments lie in the difficulty of applying consistent pressure and measuring it, both of which are required to properly identify areas with tumours. Current MIS instruments are significantly inferior to direct manual palpation and can result in tissue damage. As a result, in some cases, the conversion to open surgery is required to allow for physical tumour palpation.

The research presented in this section will assist the transition to smaller and less complex robotic surgery systems that can, hopefully, improve surgical environments. A small, lightweight instrument can be positioned directly above patients or hand held to allow more floor space in the operating room and better access to a patient. Smaller instruments are more likely to fit inside a typical hospital autoclave and permit their storage in a cabinet. Their lower weight also allows the manipulators to be easily and quickly added or removed during surgical procedures, or to convert to an open procedure [12].

Smaller sized instruments can provide further benefits as mechanisms of lighter weight require smaller motors to drive them. The smaller motors can be integrated directly into the mechanism and simplify the drivetrain composition. With a simpler drivetrain, the reliability of the system is improved due to a reduction in potential failure modes and wear of actuation cables. Most importantly, with reduced mass of the mechanism, the safety of the entire MIS system can be greatly improved. Accidental collisions between manipulators or impacts with a patient will be less likely to cause significant damage [12]. Therefore, a compact, minimally-invasive tool for tumour treatment that can mimic manual palpation and present intra-operative imaging is required to improve current treatments and enhance delivery of therapy.

Chapter 3

Tool Design and Analysis

This chapter explains the design methodology for the tumour localizing device. The design requirements and constraints, and the concepts generated, will be presented. Finite element analysis conducted on the final design will be used to demonstrate the suitability of the design for tissue palpation. This chapter will also outline some of the machining techniques used to manufacture a prototype of the design.

3.1 Design Requirements and Constraints

Hand-held tools for minimally invasive surgery require very small components and materials that are both biocompatible and sterilizable. The focus of this design is on a minimally-invasive tool for manipulation and palpation of lung tissue. To be suitable for MIS, the tool must be able to fit through a 12-mm diameter trocar and needs to have the ability to be cleaned and easily disassembled for maintenance. In addition, the tool must be able to manipulate and palpate tissue of various shapes and sizes. While conducting MIS, surgeons lose their sense of touch. Therefore, it is important to also integrate kinaesthetic, tactile, and ultrasound feedback to accurately construct haptic feedback and measure tool–tissue interaction forces.

The presented design requirements and constraints were generated based on consultation with thoracic surgeons and experience gained with previously designed palpation and tumour localization tools [10], [13]. The tools developed to date are able to palpate tissue and localize tumours,

but their usage for MIS is very limited as they are mechanically complex, hard to implement, and difficult to sterilize and clean. The new design will attempt to address the drawbacks and limitations experienced with the current minimally-invasive surgical tools.

One of the major limitations in previously designed graspers, coupled jaw motion, will be addressed in the new design. From experience gained with a previous generation of the tool [10], it was discovered that incorporating independent jaw motion could improve jaw alignment with tissue, thereby achieving better data readings from sensors on the jaws. Independent jaw motion also improves tool dexterity and provides more freedom to manipulate and palpate tissue. For example, one jaw can act as a backbone for palpation while the other initiates the palpation motion. It should also be possible to automate jaw motion to allow for future integration with robotic systems.

In addition to having independent jaw motion, the design is required to reuse sensorized jaws that were designed and made for the previous generation palpation instrument. The jaws include ultrasound and tactile sensors. The ultrasound jaw was designed by Kurowski [10], while the tactile jaw and sensor were designed by Naidu [52]. This constraint greatly limited the mechanical design of the instrument. The jaws were designed based on commercially available tools used for tissue manipulation. More specifically, the way that the jaws were designed to attach to the rest of the instrument, and the length of the jaws, create a large force amplification that weakens the overall design. Such a design constraint made it difficult to meet tool strength requirements while still fulfilling the minimally-invasive size constraint.

3.2 Design Specifications

Design specifications were generated to establish theoretical performance standards to help guide the design process. By comparing the specifications of state-of-the-art hand-held devices (Table 3.1), it was determined that a total of 3 DOF for the instrument would be desirable, two of which account for jaw motion. In order to effectively manipulate lung tissue, the tool needs to be able to support the mass of a lung, about 800 g [53], and be able to palpate tissue of up to 40 mm in thickness [41]. A higher target load capacity of 10 N was selected to account

for variability in the mass of a lung across a population. In addition, to acquire reliable and meaningful data from sensors on the jaws, the tool needs to be able to apply a palpation force of 5 N [50]. To ensure accurate jaw motion, an angular speed of 1 to 2 degrees per second needs to be achieved with a resolution of at least 0.01 degrees. These motion characteristics were derived from a minimally-invasive grasper design by Rosen *et al.* [17]. To optimize the ergonomics of the instrument, anthropometric data [54] was used to determine an optimal size range for the tool handle, 80 to 90 mm in length and 55 mm to 65 mm in diameter. A list of design specifications and design targets are provided in Table 3.2.

Table 3.1: Summary of DOF available in state-of-the-art hand-held palpation and grasper devices.

DOF	Trocar Diameter (mm)	Reference
2	10	[55]
3	10	[56]
3	10	[31]
3	12	[10]

Table 3.2: Design specifications and targets derived from design requirements.

Design Specifications	Design Target
Nominal load capacity	10 N
Nominal palpation force	5 N
Nominal speed	1–2 °/s
Movement resolution	$\leq 0.01^\circ$
Diameter of handle	≤ 65 mm
Length of handle	80–90 mm
Widest jaw opening	≥ 40 mm
DOF for each jaw	3
Trocar size	12 mm
Tool length	300–400 mm
Tool weight	600–800 g

3.3 Concept Selection and Evaluation

Based on the design requirements and specifications, various concepts were generated. A summary of the concepts and their evaluation is presented in this section. The concepts generated are broken down into the main components of the tool: articulated wrist design, multiple link design, and handle and support shaft design.

3.3.1 Articulated Wrist Design

One of the first concepts considered for the MIS tool was an articulated wrist design offering five DOF. If a hypothetical wrist joint were to be implemented on a regular grasper (Figure 3.1), three rotational DOF can be implemented about the X, Y and Z axes. Two additional DOF can be achieved through the opening and closing of the jaws, and by changing their pitch. Several challenges accompany the inclusion of wrist joints. Positional accuracy can worsen with each added DOF due to the accumulation of error in joint position. In addition, the length of the end effector may increase substantially and make the tool unsuitable for the chest cavities of certain patients, unless shorter jaws are used. Finally, the added complexity of the system may no longer allow for intuitive human control of the device.

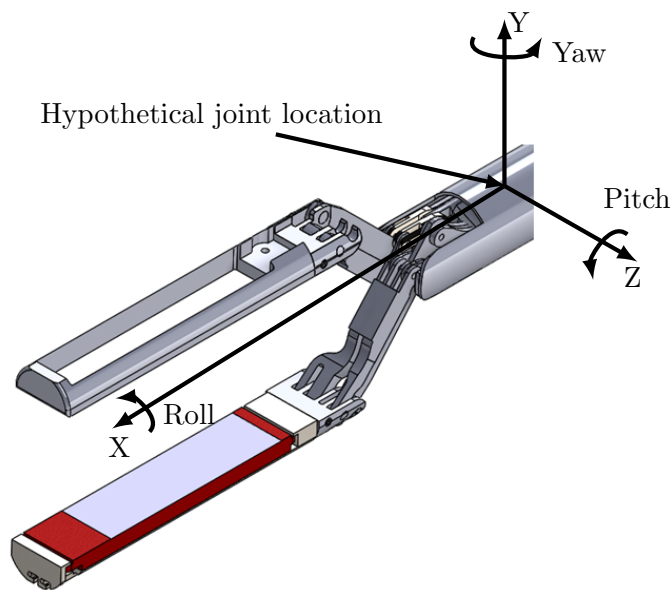


Figure 3.1: Coordinate system for wrist motion.

Despite the complexity of wrist joints, partial wrist motion can be implemented in a simpler manner than full wrist motion. In such a configuration, either the roll, pitch or yaw DOF are implemented. As a starting point, a Hooke joint was first considered (Figure 3.2). A Hooke joint can provide two DOF, pitch and yaw. The implementation of such a joint would require the use of cables or flexible rods to facilitate bending.

Cables require a tensioning mechanism that increases tool weight and complexity. Cables also stretch, wear out quickly, and have variable tension and friction that can negatively affect the accuracy of jaw movement. Conversely, flexible push rods experience less stretch and wear, but there is a high degree of uncertainty that they work reliably and are strong enough to support palpation forces.

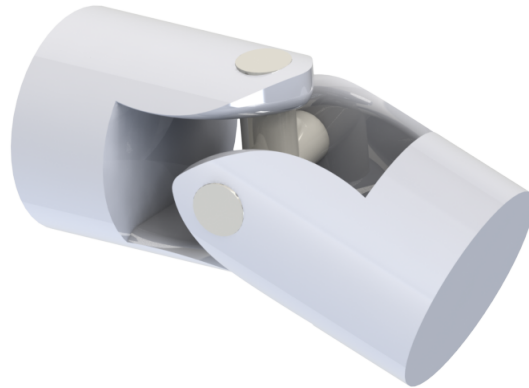


Figure 3.2: Hooke joint structure.

Since neither cables nor flexible push rods seemed to be optimal, a gear system, such as a bevel and spur gear system (Figure 3.3), was considered instead. Such a system would add a roll DOF. This system can also be combined with a Hooke joint to provide all three DOF. However, the implementation of such a gear system, or any other gear system in general, would significantly complicate the design. In addition, another actuator would be required for each added DOF, further increasing the weight, size and complexity of the device. This design would increase manufacturing costs, and make it significantly harder to complete maintenance or repair duties on the tool. In order to keep the design simple, a wrist motion without physical actuators was considered instead.

The easiest DOF to implement without any actuators, would be roll. Two configurations are possible for this DOF, one where the jaws move relative to a stationary handle and one where the handle can be repositioned relative to the jaws. The stationary handle configuration has been implemented in a previous generation of the instrument [41]. The mechanism involved a push and pull plastic shaft collar that allowed the entire distal end of the instrument to be rotated 180 degrees (Figure 3.4).

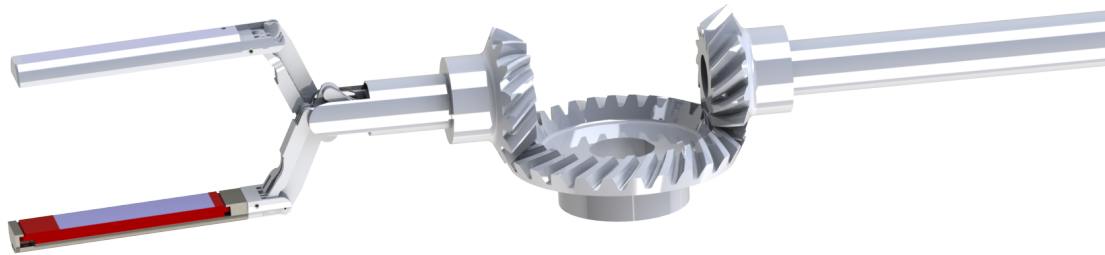


Figure 3.3: Bevel and spur gear system design.

A simpler alternative to this approach involves the integration of floating controls such that they can be repositioned or rotated about the center axis of the instrument. Such a system allows the entire tool to be rotated relative to the controls (Figure 3.5). Assuming that the wiring of the controls allow for rotation, this concept would work well for a hand-held instrument where roll can be easily implemented by the user changing the grip position on the handle. Floating controls would also require minimal added complexity and no additional actuators.

Having no articulated joints provides further advantages as the use of cables can be avoided and push rods can be used instead. Push rods are larger in diameter than cables and deform less than cables of similar material under the same loading conditions. The decreased deformation will reduce backlash in jaw motion and improve the accuracy of the control system. The main disadvantage of using push rods is their larger size, which limits the amount of space available for electrical wires to pass through the shaft of the instrument. In addition, push rod mechanisms, if improperly manufactured, are prone to backlash. However, the benefits of using push rods outweigh the disadvantages, especially when it comes to servicing and the simplicity of the design.

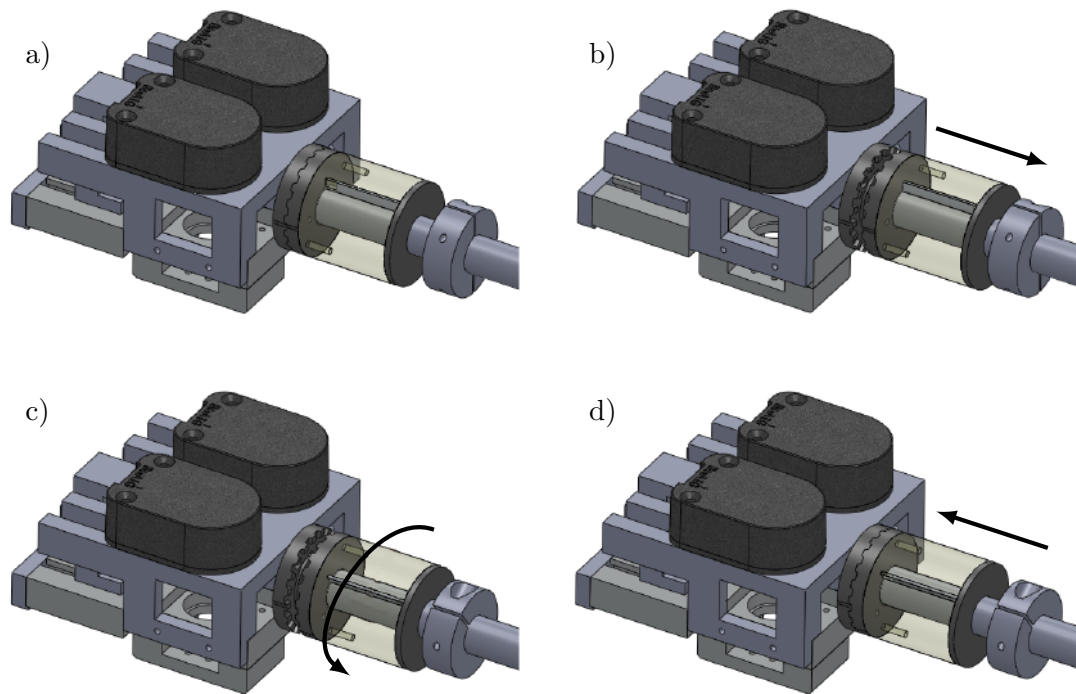


Figure 3.4: Twisting mechanism of the end effector implemented in a previous generation tool. The plastic collar is shown translucent. a) Collar in closed position. b) Collar is pulled forwards to allow rotation of distal end. c) Entire distal end is rotated. d) Collar is pushed back into its closed position [41].

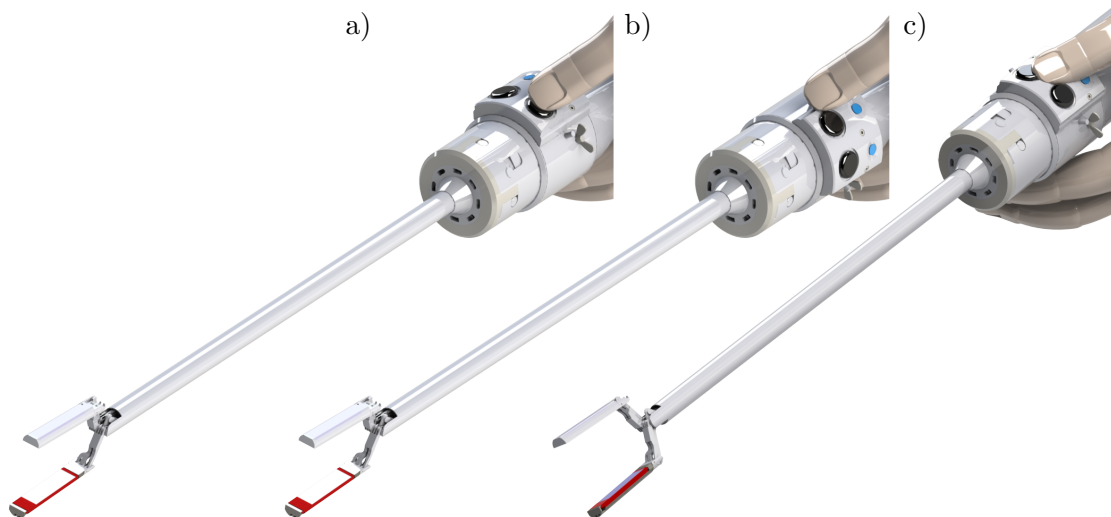


Figure 3.5: a) Tool is held upright with controls aligned with the hand. b) The user rotates the controls counterclockwise while the rest of the tool stays stationary. c) The entire tool is rotated clockwise so that the controls are aligned with the hand again.

Push rods can be easily replaced, experience less wear, are cheaper than equivalently stiff cables, and have the flexibility of being manufactured into complex geometries, allowing for more variety in design. More importantly, one of the design goals for this tool is to have a compact handle assembly in order to improve the ergonomics of the tool. Push rods can easily facilitate the use of actuators that are aligned with the instrument's central axis, which helps to minimize handle size. In contrast, using a cable driven mechanism would require large amounts of rotary motion, making a compact handle harder to implement.

3.3.2 Multiple Link Design

Palpating against soft tissue can produce varied results due to the variable stiffness of the supporting tissue. The use of a grasper design was justified because it ensures that the jaw sensors are always supported by a rigid backing that increases the accuracy and repeatability of measurements. For optimal tactile and ultrasound sensor operation, the sensors need to be in contact with the tissue over as much of the sensing surface as possible. Data acquired by the sensors can then be relayed back to the surgeon in the form of haptic and visual feedback. While proper tissue contact directly impacts data quality, data processing and feedback are beyond the scope of this thesis.

Before a multi-link design was generated, a simpler, scissor-like, jaw design was considered. However, since scissors only have one DOF of motion, they would not be optimal for tissue palpation as the end effector would not always align well with the tissue. Therefore, a multi-link configuration was considered instead, in which better jaw to tissue alignment is provided by an additional DOF. The added DOF allows the grasping of various angled surfaces such as a ramp, a wedge, and a square (Figure 3.6). Since lungs vary in shape and size, the added DOF will allow the palpation of many different tissue shapes and thicknesses.

Various link configurations were generated to implement two DOF for each jaw. Since the jaw geometry was predefined, link configurations were limited and had to attach to the proximal end of the jaw. A cable driven mechanism that uses sliders to control jaw motion was first considered. However, in order to implement uncoupled jaw motion, a very large diameter shaft was required to fit all of the sliders. As a result, the design did not meet the size requirements for MIS. Instead,

a hybrid cable–push-rod system, which has fewer parts and can provide a more compact actuation mechanism (Figure 3.7), was considered as an alternative. As can be seen in Figure 3.8, a cable can run from the jaw at location ‘A’ to the roller at ‘B’ and continue back to the handle of the tool where it can be actuated. However, this design is very weak when supporting side loads due to very minimal support of the jaw at location ‘A’.

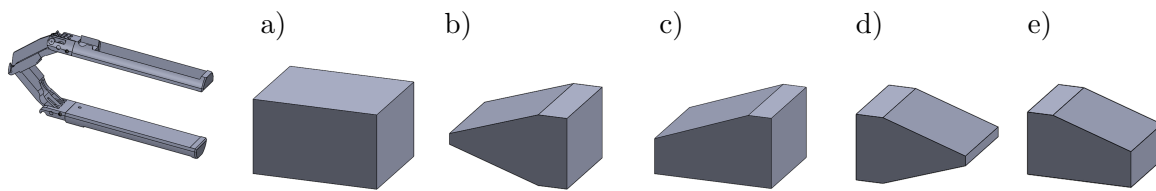


Figure 3.6: Ideal grasping orientations: a) square, b) inclined wedge, c) inclined ramp, d) declined wedge e) declined ramp. Grasping orientation is indicated by the jaw on the left side of the figure.

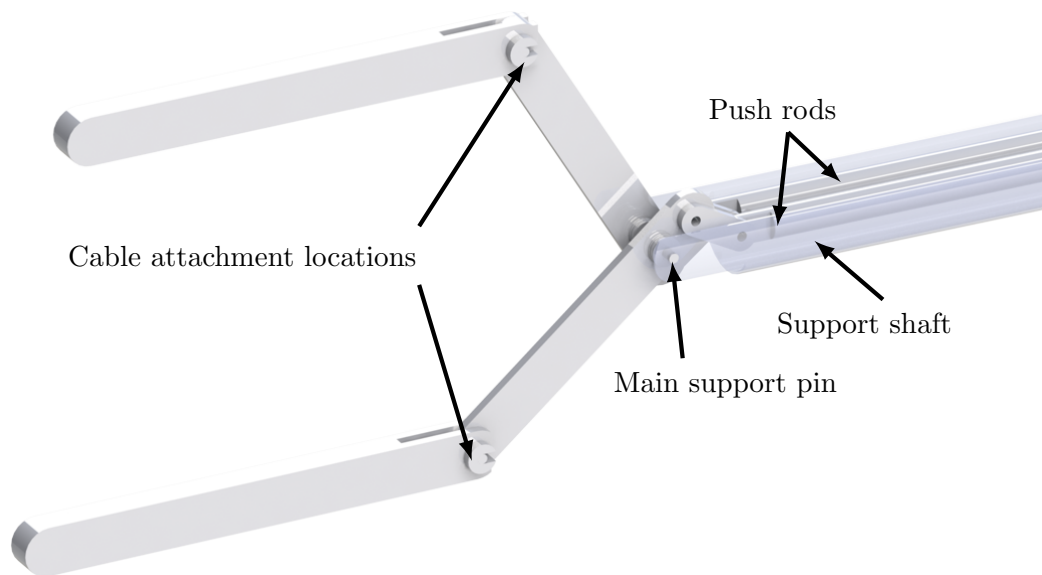


Figure 3.7: Hybrid cable–push-rod link mechanism. Cables not shown.

In order to strengthen the design, cables were completely avoided and a system consisting of only push rods was implemented (Figure 3.9). The improved design incorporated several side-by-side links to provide better support for the jaw. The elimination of cables also simplified the design as a tensioning mechanism was not required. To further strengthen the end effector, an extended support shaft was also considered (Figure 3.10). The extension can allow for better side load support throughout jaw motion. As shown in Figure 3.11, a slider moves along a slot in the

extension to provide continuous side support. The main drawback of this design is that it only supports one side of each jaw. The design is also complicated to implement as any outward loads may cause the slider to fall out or may cause permanent deformation to the shaft causing it to lose functionality.

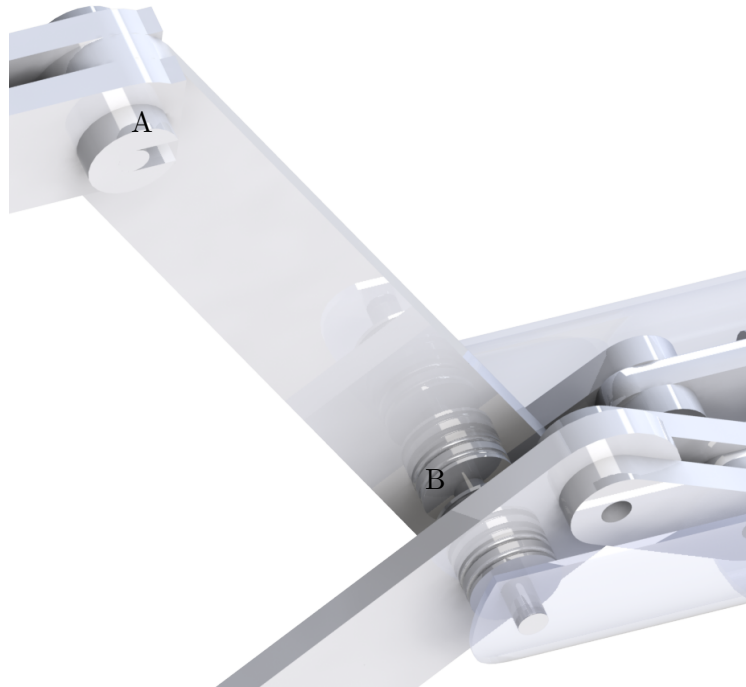


Figure 3.8: Close up view of rollers and jaws. Cables, not shown, would connect to the jaw at location 'A' and run through rollers at 'B'.

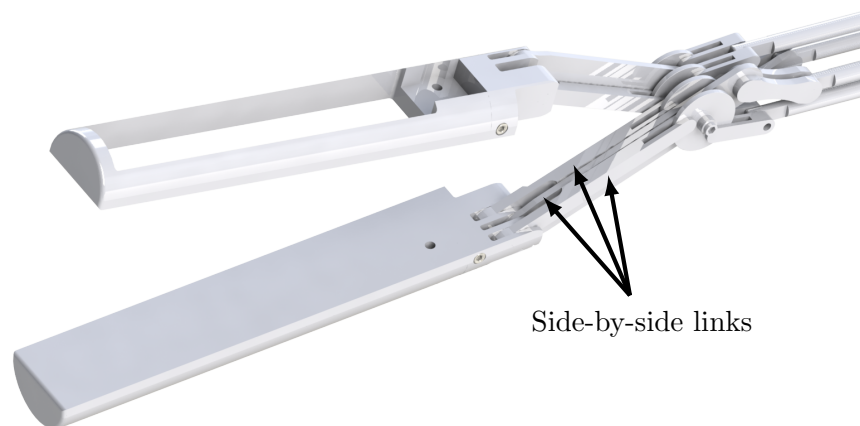


Figure 3.9: Improved linkage mechanism with multiple side-by-side support links. The support shaft is hidden for better visibility of the mechanism.



Figure 3.10: Linkage mechanism with an extended support shaft.

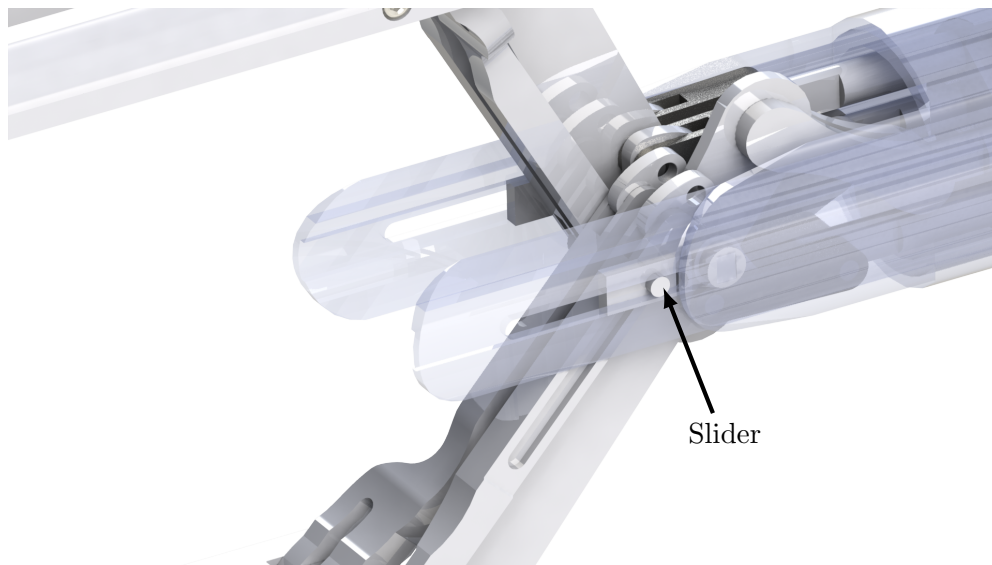


Figure 3.11: View of linkage mechanism with shaft transparent.

Due to the drawbacks of the extended support shaft, a modified link design was considered instead (Figure 3.12). In this design, the outer links supporting the jaw are connected with an intermediate support. The rollers at the main support pin also have a support between them (Figure 3.13). The extra supports doubled the side load carrying capacity, as calculated in FEA simulations. Although the supports improved the strength of the instrument, more refinement of the design was still required to optimize it.

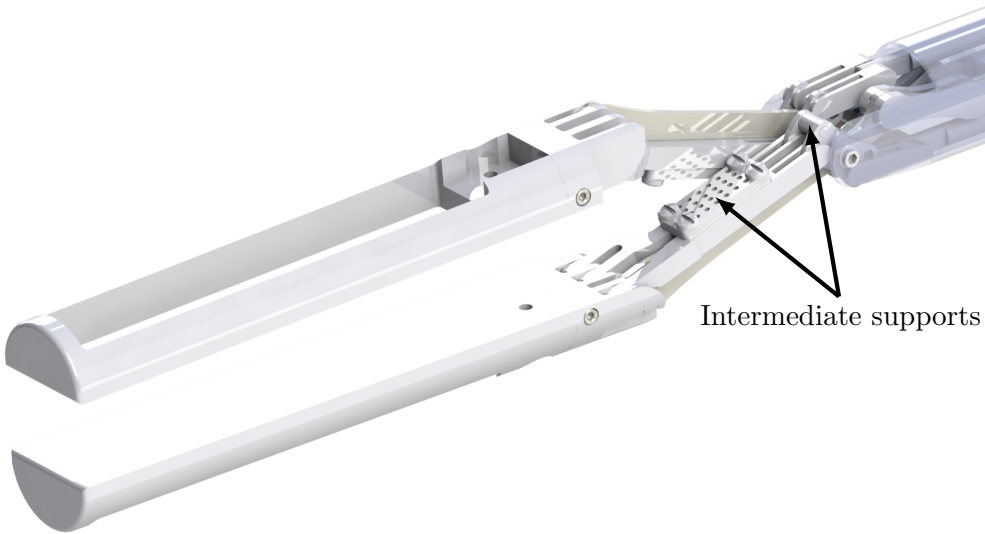


Figure 3.12: Linkage mechanism with intermediate link supports.

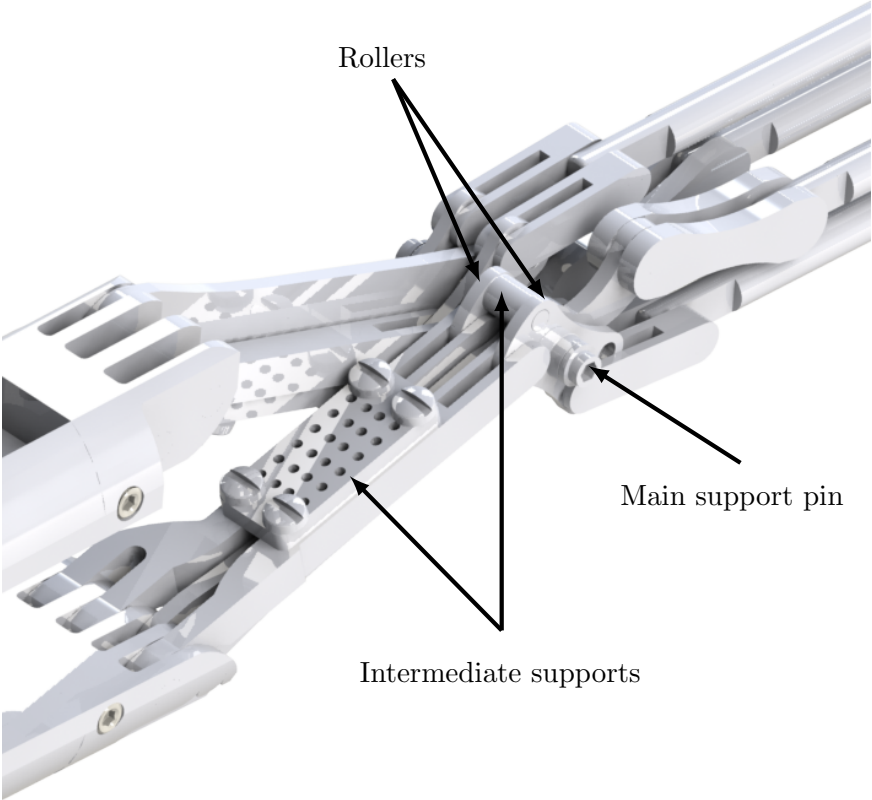


Figure 3.13: Detailed view of linkage mechanism with supports. Supporting shaft is hidden for better visibility.

The intermediate link support design was refined and improved using results from FEA, and by reducing the number of components in the assembly. The final iteration of the linkage mechanism consists of two jaws that support the ultrasound and tactile sensors (Figure 3.14). Each jaw is connected to the rest of the instrument via an adapter that holds the jaws in place using set screws, and is supported by two independent series of links. Each series is shown in Figure 3.15. One link from each series connects directly to the jaw, and provides one DOF of jaw motion. The link system is held together using pins (Figure 3.16) and is actuated by push rods.

The final design can open up to 35 mm with a parallel jaw configuration (Figure 3.17), and close all of the way so that the jaws are touching. Jaws can also open up to palpate tissue of 128 mm in thickness (Figure 3.18). At a fully opened position, the jaws are at 95 degrees to each other and can tilt 66 degrees inwards (Figure 3.19). The jaws can also make a 60 degree sweeping motion (Figure 3.20). Single jaw motion is shown in Figure 3.21.

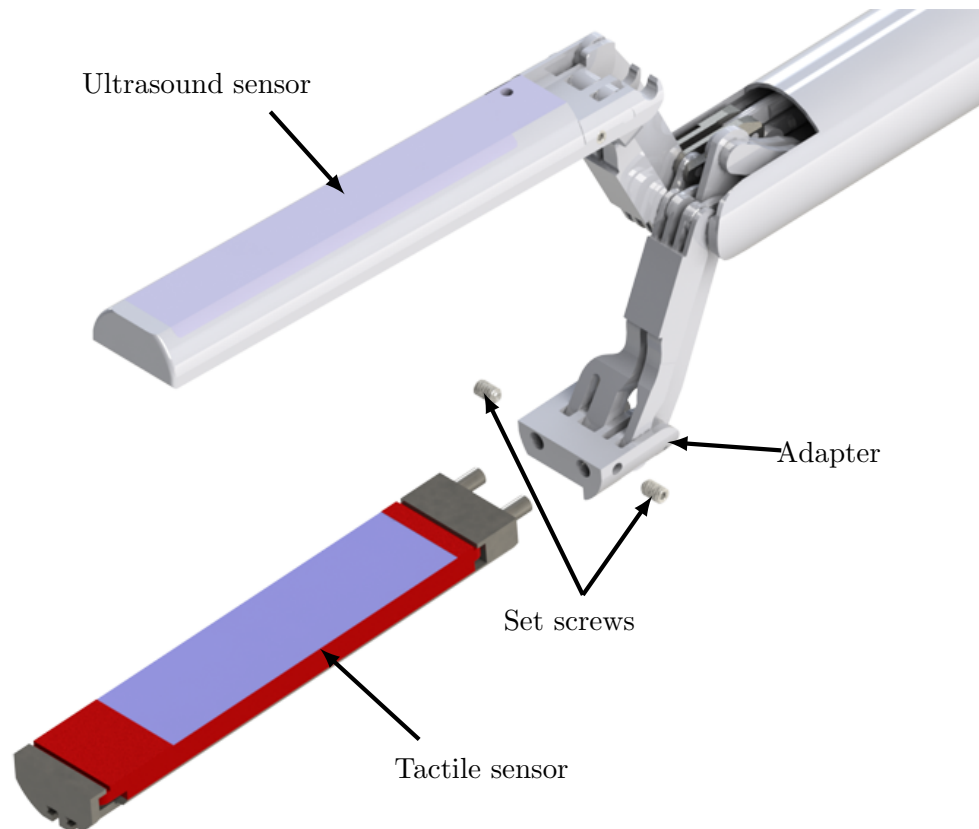


Figure 3.14: Final jaw linkage design.



Figure 3.15: Linkage actuation mechanism with push rods. Links of each series are numbered in separate colours.

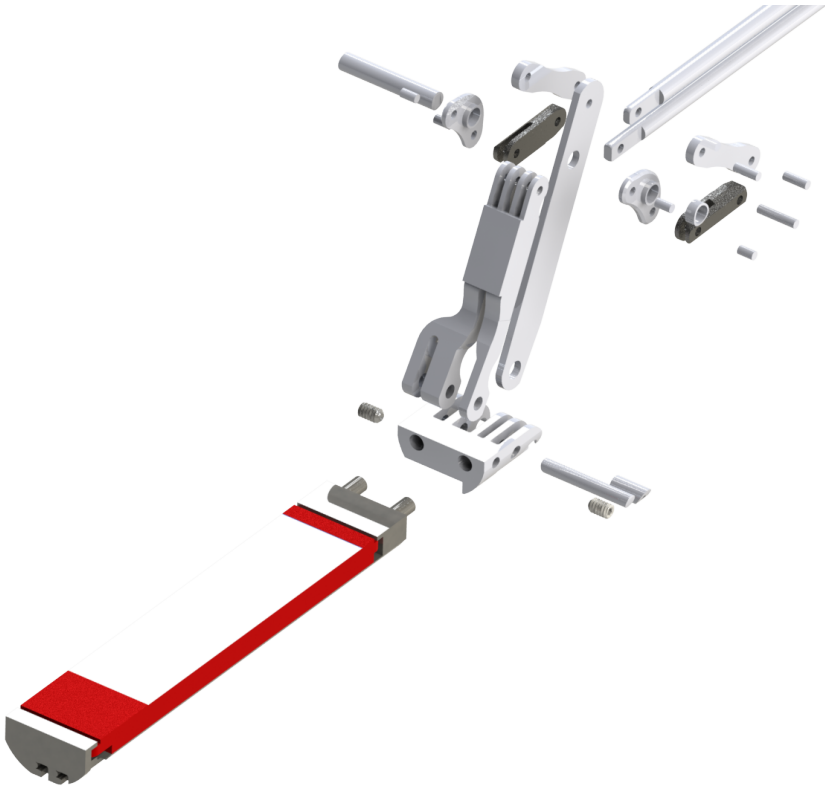


Figure 3.16: Exploded view of jaw linkage components.



Figure 3.17: Maximum parallel jaw opening.

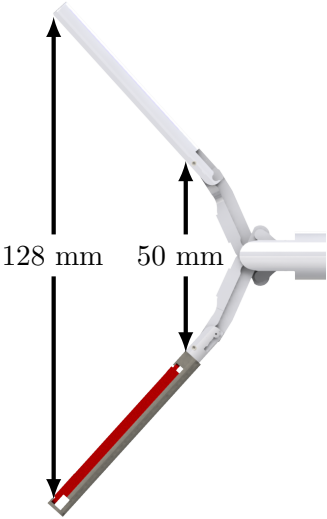


Figure 3.18: Maximum jaw opening.

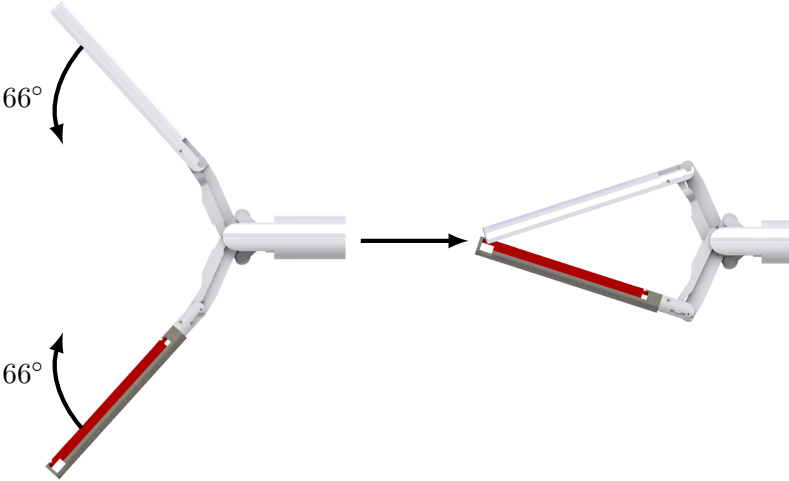


Figure 3.19: Jaw tilt at a fully opened position.

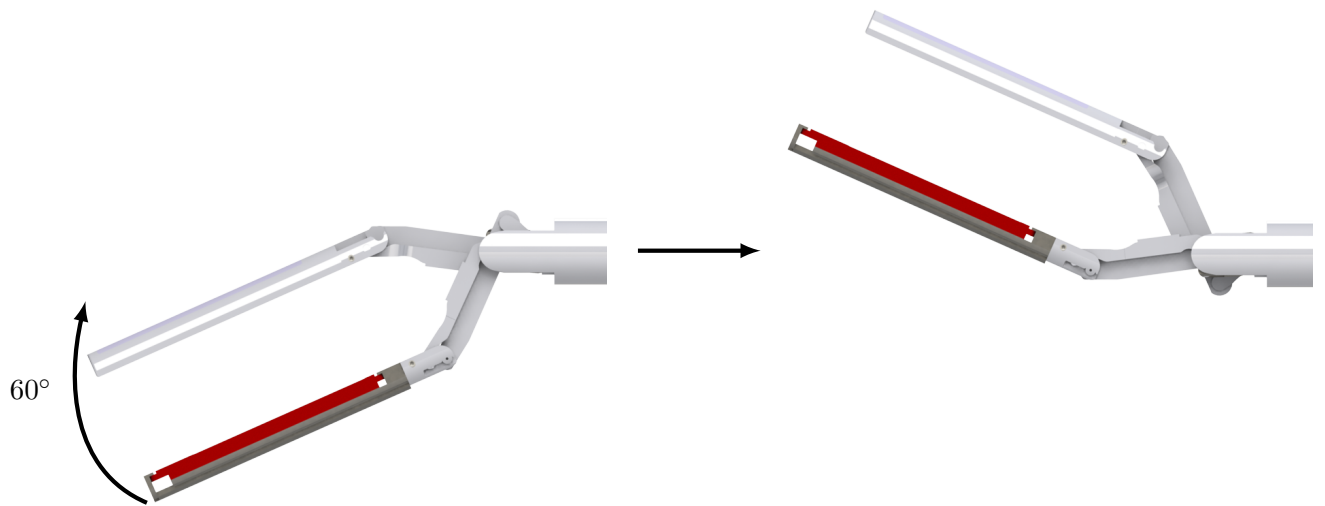


Figure 3.20: 60 degree jaw sweep.

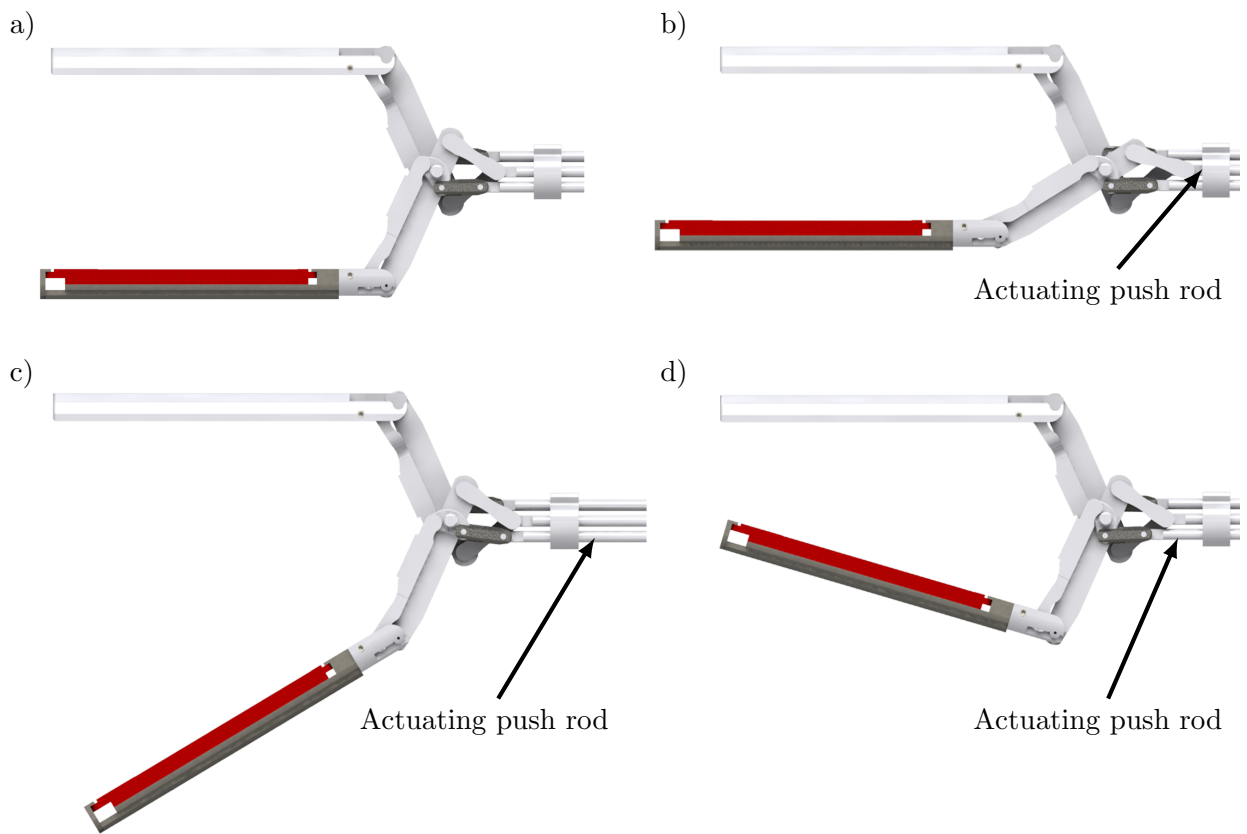


Figure 3.21: Single jaw motion: a) Fully open position. b) Bottom jaw is closed by pulling the push rod. c) Bottom jaw is rotated outwards by pulling the push rod. d) Bottom jaw is rotated inwards by pushing the push rod.

3.3.3 Support Shaft and Handle Design

The main goal of the shaft and handle design process was to create a system that can be easily assembled and disassembled and can provide ample room for electrical wires to connect to sensors on the jaws. The support shaft and handle were considered as two separate systems that are connected together through a quick-release mechanism. The support shaft is composed of three components: top cover, base, and a sleeve with an outer diameter of 12 mm that holds the other two pieces together (Figure 3.22). The shaft and sleeve support the entire push-rod-linkage system. The top cover and base are able to slide into the handle (Figure 3.23) while the sleeve is attached through an 18 degree turn-lock mechanism (Figure 3.24 and 3.25). Keyways in the handle and on the base help align the components.

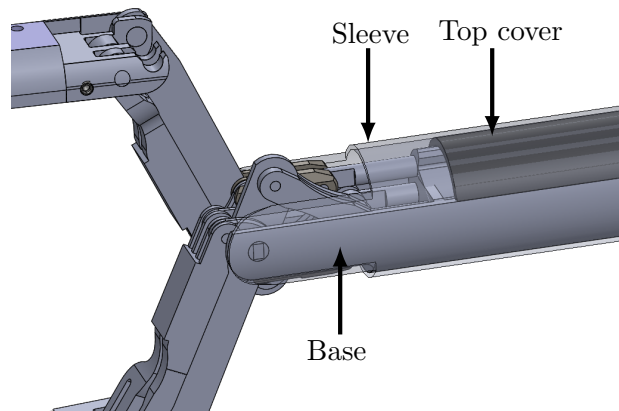


Figure 3.22: Support shaft components: base, sleeve and top cover.

Furthermore, the support shaft, with a 10.2-mm inner diameter, is lined with guides that support the push rods (Figure 3.26 and 3.27). The push rods extend from the jaws to the handle where ball lead screws control their movement (Figure 3.28). Lead screw linear motion is transferred to the push rods via a ball nut adapter that connects the two components together. Each lead screw is controlled by one motor. Since push rods are mechanically fastened to the adapter, a quick-release mechanism was implemented to allow the push rods to be efficiently detached without detaching them directly from the adapter.

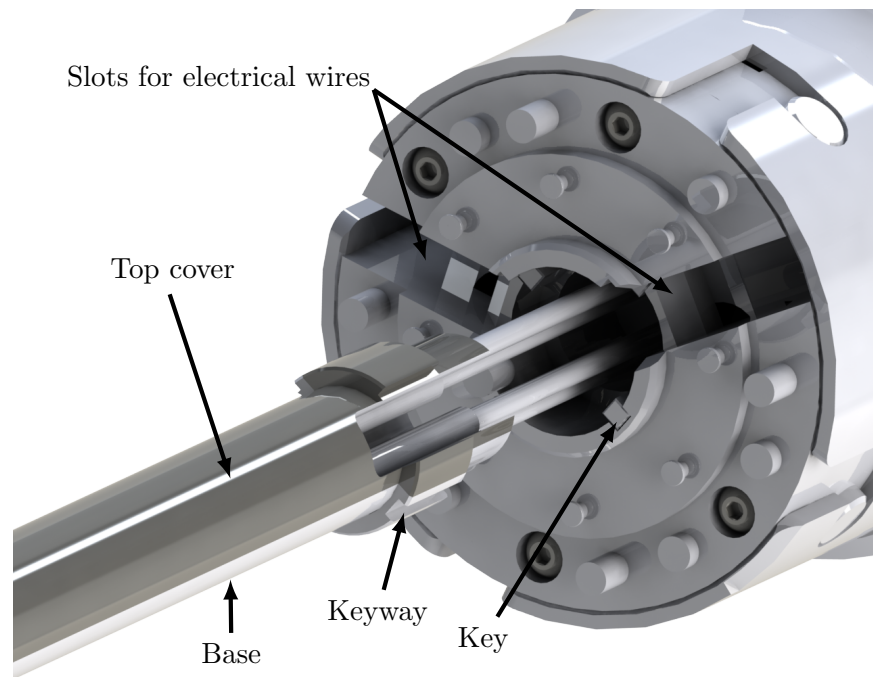


Figure 3.23: Connection of the top cover and base to the instrument's handle.

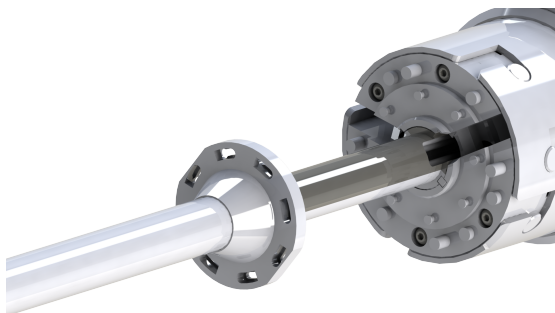


Figure 3.24: Quarter turn sleeve design.

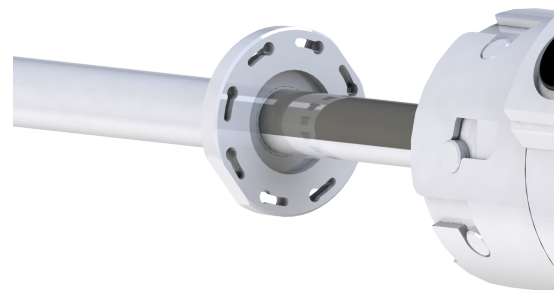


Figure 3.25: Rear view of quarter turn design.

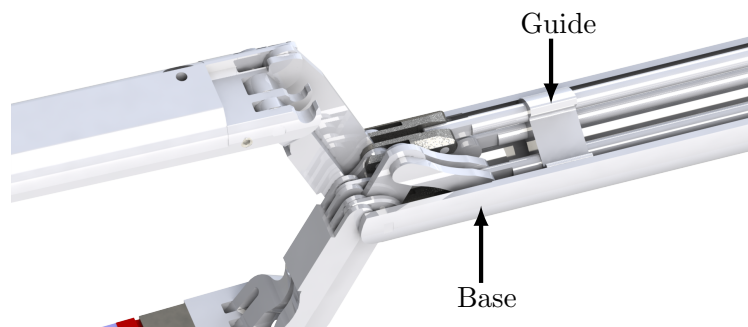


Figure 3.26: Push rod guide set up.

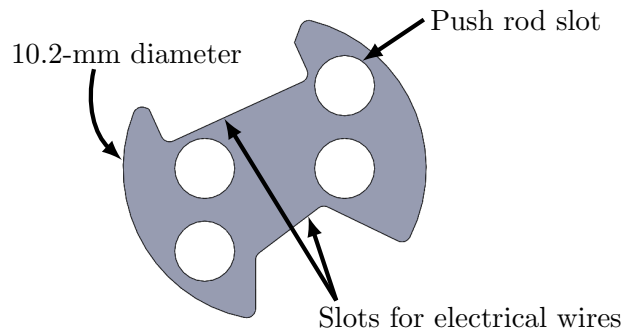


Figure 3.27: Guide cross-section.

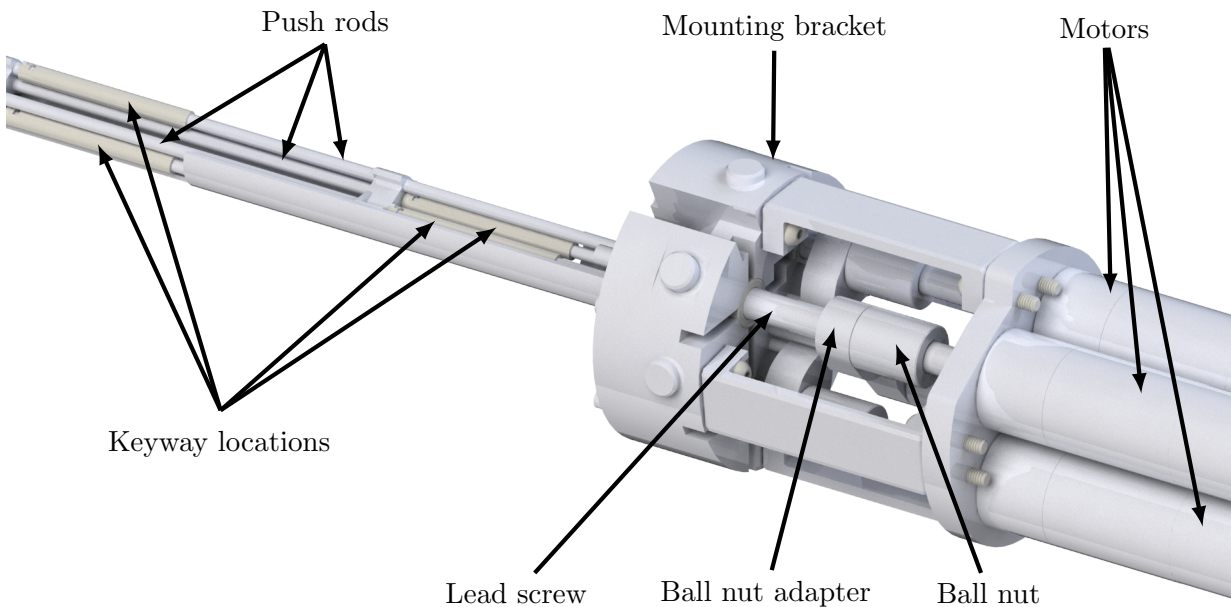


Figure 3.28: Motor and lead screw assembly at the proximal end of the tool.

Each push rod has a keyway at the proximal end, just before it attaches to a lead screw. These keyways allow the distal end of the instrument to be easily disconnected without detaching any motors or taking apart the handle (Figures 3.29 and 3.30). The keys are held in place by a cover that clips into pins pressed into the push rod and can be easily removed. These pins also act as mechanical stops for push rod movement. The base has slots that allow access to the keyways (Figure 3.31). The ability to easily separate the proximal and distal ends of the instrument allows for easy tool assembly, cleaning and sterilization. Detailed disassembly instructions can be found in Appendix A.

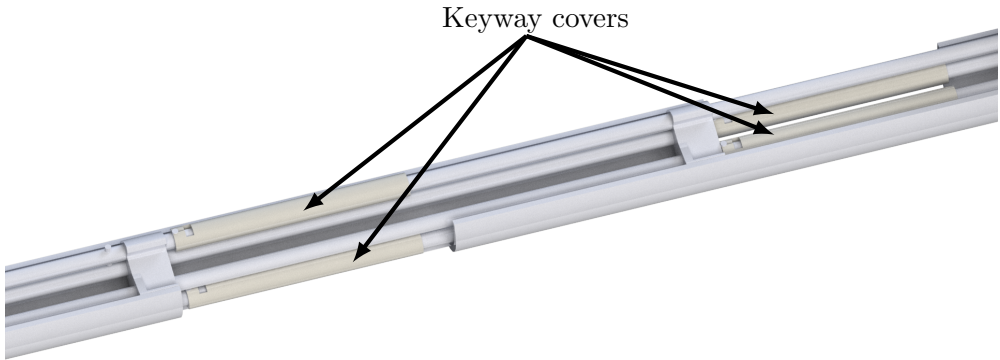


Figure 3.29: Push rod keyway covers.

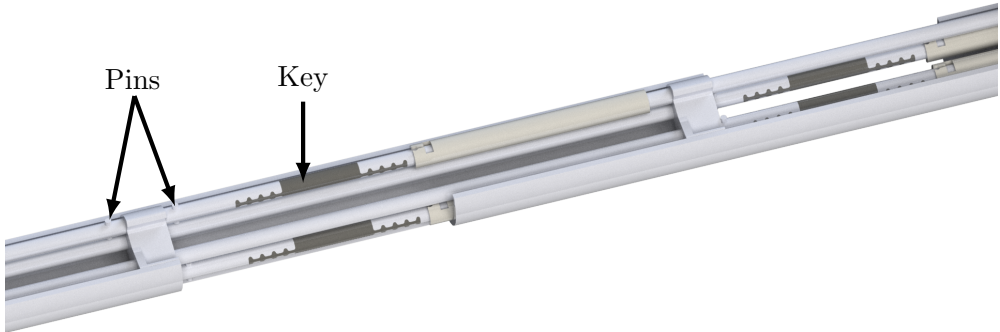


Figure 3.30: Push rod keyways with covers removed.

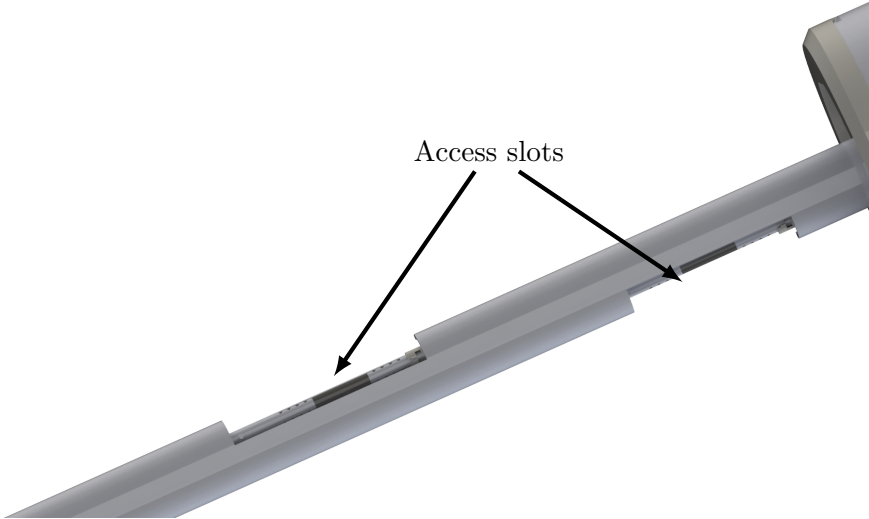


Figure 3.31: Keyway access slots in the base of the support shaft.

The quick-release system is unique in its use of very few mechanical fasteners. The only mechanical fasteners used in the design are for mounting four motors at the handle (motor selection is covered in Chapter 4.1.1). The motors are fastened to a plate that is attached to the rest of the instrument via four mounting brackets. This attachment configuration further facilitates easy assembly of the device as it allows the motors to be mounted prior to attaching them to the rest of the instrument (Figure 3.32).

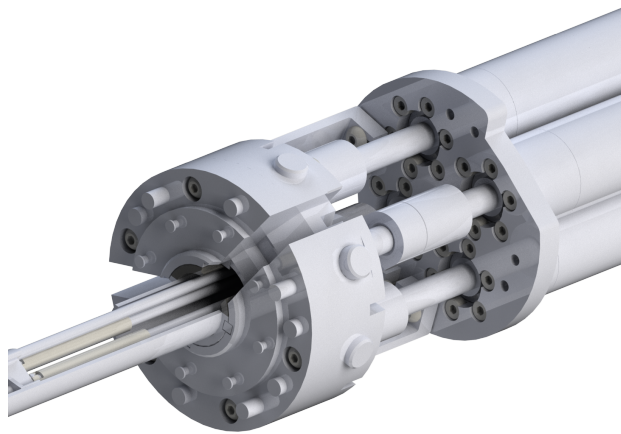


Figure 3.32: Mounting of motors with mounting brackets hidden.

The motors are encased in a cylindrical sleeve that forms the handle of the instrument (Figure 3.33). The handle can be removed via a turn-release mechanism consisting of five pins that hold the cylinder in place (Figure 3.34). One pin acts as a release pin that prevents the rotation of the handle. The pin is spring loaded and can be pressed inwards to allow the handle to be removed. On the handle, two joysticks and two push buttons are mounted. The joysticks and buttons serve as user controls for the motors. The controls can be rotated 270 degrees around the handle to allow the device to be used in any orientation. Rotation is inhibited by a thumb screw located near the controls.

Although several quick-release mechanisms were implemented in the design, the mechanisms will only work if wiring that passes through the shaft can also be easily disconnected at the same location as the support shaft. The wiring of the sensors is beyond the scope of this project, however, sufficient room for ultrasound cabling and tactile sensors was provided in the design as well as extra space for other cables and connectors.

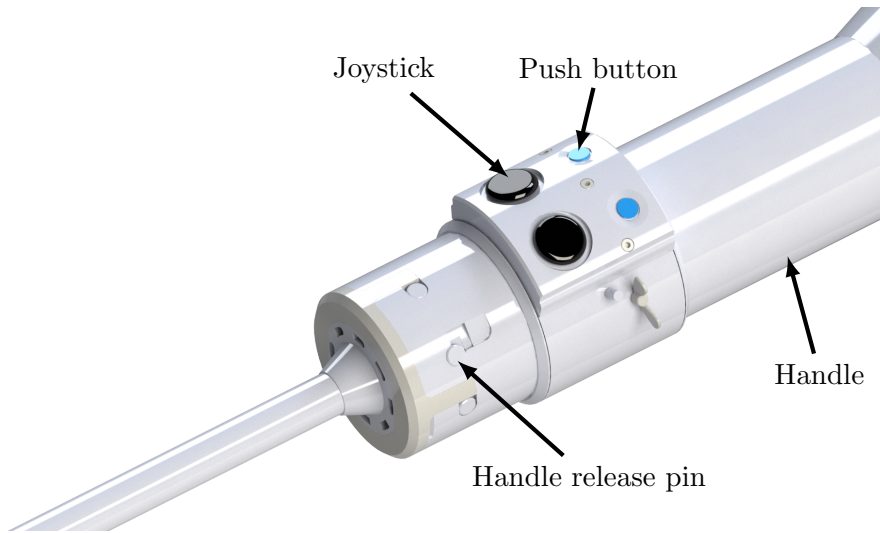


Figure 3.33: Instrument handle with controls.

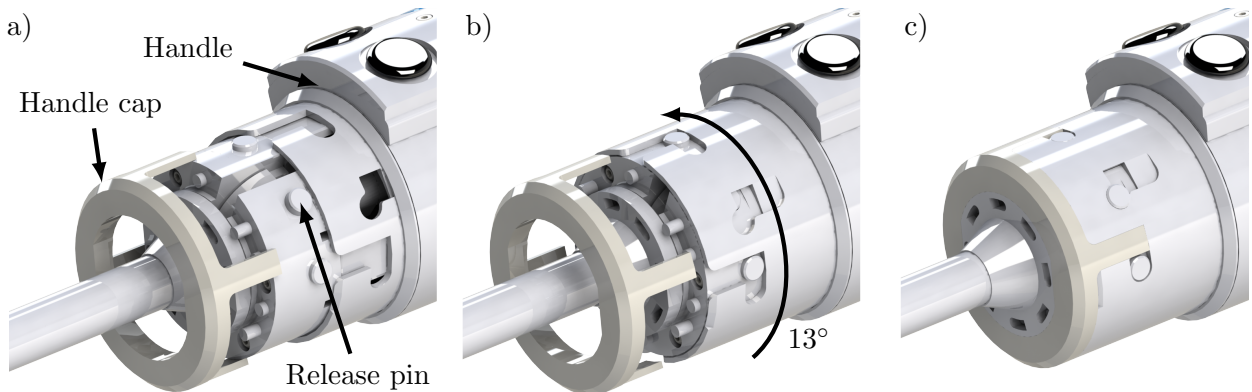


Figure 3.34: Instrument handle attachment mechanism: a) The handle is aligned with the pins. b) The release pin is pressed inwards and the handle is moved forwards so that it is sitting flush with the pins. The handle is then rotated 13 degrees clockwise. c) The cap is pushed into place.

3.3.4 Final Design

To create the final design, the multi-link, articulated wrist, handle and shaft concepts were combined to create a complete tool. Over 100 iterations were made to create the final instrument, named the Palpatron (Figure 3.35). The designs were refined by reducing the number of assembly parts, especially fasteners, and using FEA. Parts of the final design were realized as a physical prototype. Figure 3.36 shows a scaled up model of the link mechanism. The purpose of prototyping the mechanism was to verify the functionality of the designed multi-link mechanism, identify any structural weaknesses, and to determine ease of assembly.



Figure 3.35: CAD render of final tool design.

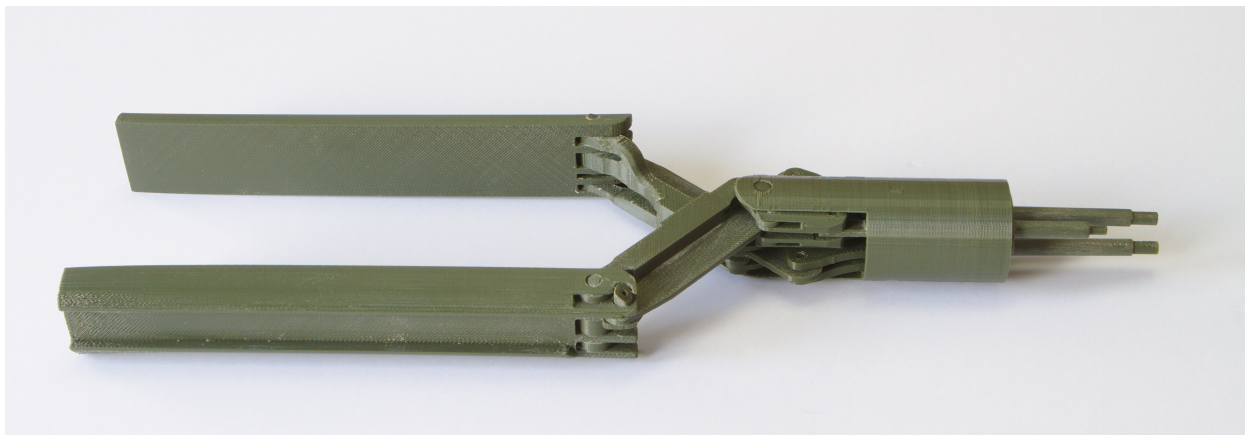


Figure 3.36: Linkage mechanism prototype, scaled in size by a factor of four.

Although the integration of different sensing modalities is beyond the scope of this project, strain gauges were incorporated into the final design of the tool and were placed on one link for measurement of tool–tissue forces. The mounting and implementation of the strain gauges will be further discussed in Chapter 4. Overall, the final design can accommodate three sensing modalities that can be combined together to display palpation information in an intuitive manner.

3.4 Finite Element Analysis and Material Selection

FEA was conducted on the main components of the tool in order to determine a suitable material for the design. As a preliminary test (Figure 3.37), a 10 N load was applied perpendicularly to one jaw, positioned at 140 degrees relative to Link 3. Details of the FEA model setup are described in Appendix B.1. In order to eliminate any dependencies of the model on mesh size, the mesh of the model was gradually refined until a difference of less than 5% was observed between two consecutive results. The results from the FEA are presented in Figure 3.38. From the results, it was determined that the critical stress points are at the pins. This was expected considering the surface area and wall thickness near the pins are very small compared to the rest of the instrument (Figure 3.39). A similar analysis was also conducted at various other jaw positions including maximum and minimum jaw opening. It was discovered that a maximum stress of 700 MPa is experienced by the links when the jaw is in the fully closed position (Figure 3.40). However, by modifying the scale on the stress results, a closer inspection of the model reveals that the maximum stress is closer to 420 MPa (areas shaded red in Figure 3.40). This suggests that the calculated maximum stress is a stress singularity and does not reflect the real stress on the link.

In addition to normal loading conditions, the tool may also experience side loads (Figure 3.41). The highest calculated stress for this loading condition is 1,514 MPa (Figure 3.42). However, after modifying the scale of the results (Figure 3.43), this stress appears to be another stress singularity as it occurs at the edge of the main support pin. The stress that the pin actually experiences is closer to 550 MPa, as shown by the updated scale of results.

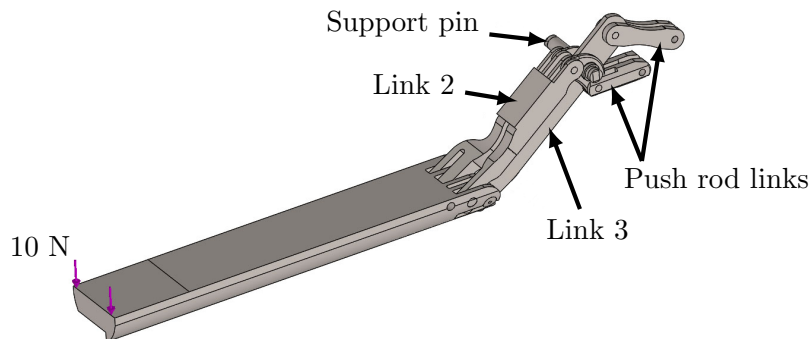


Figure 3.37: FEA model of jaw with a 10 N load.

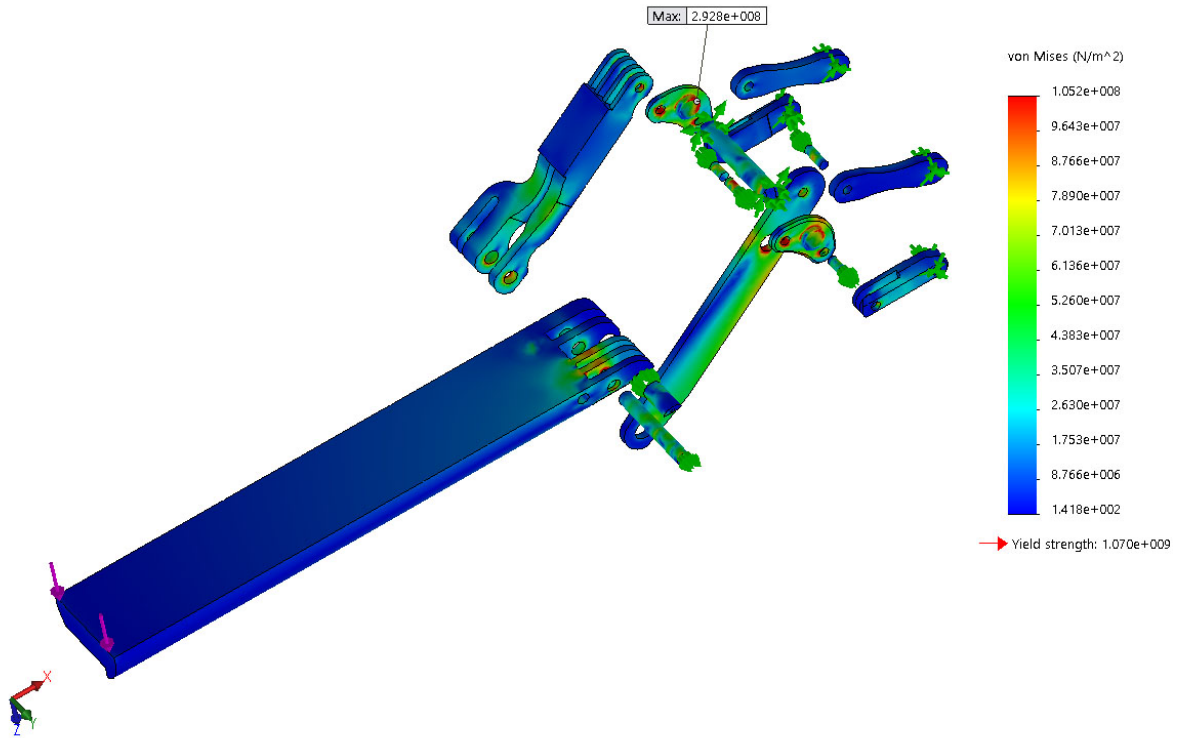


Figure 3.38: FEA stress results at a 40 degree jaw opening.

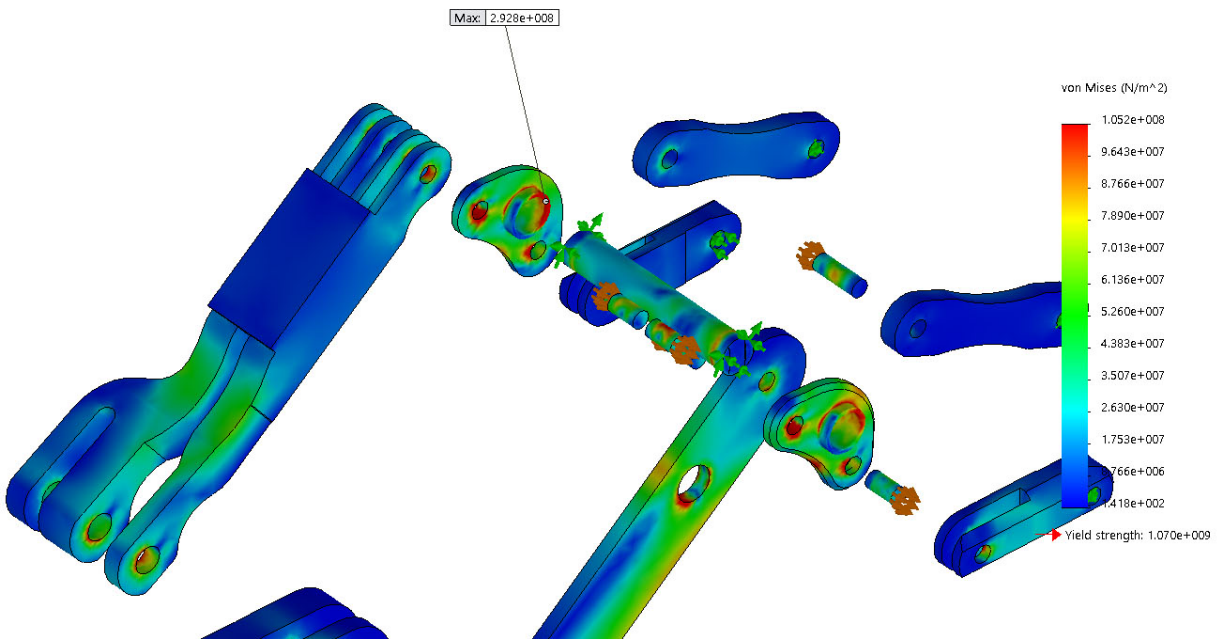


Figure 3.39: Close up of FEA at a 40 degree jaw opening.

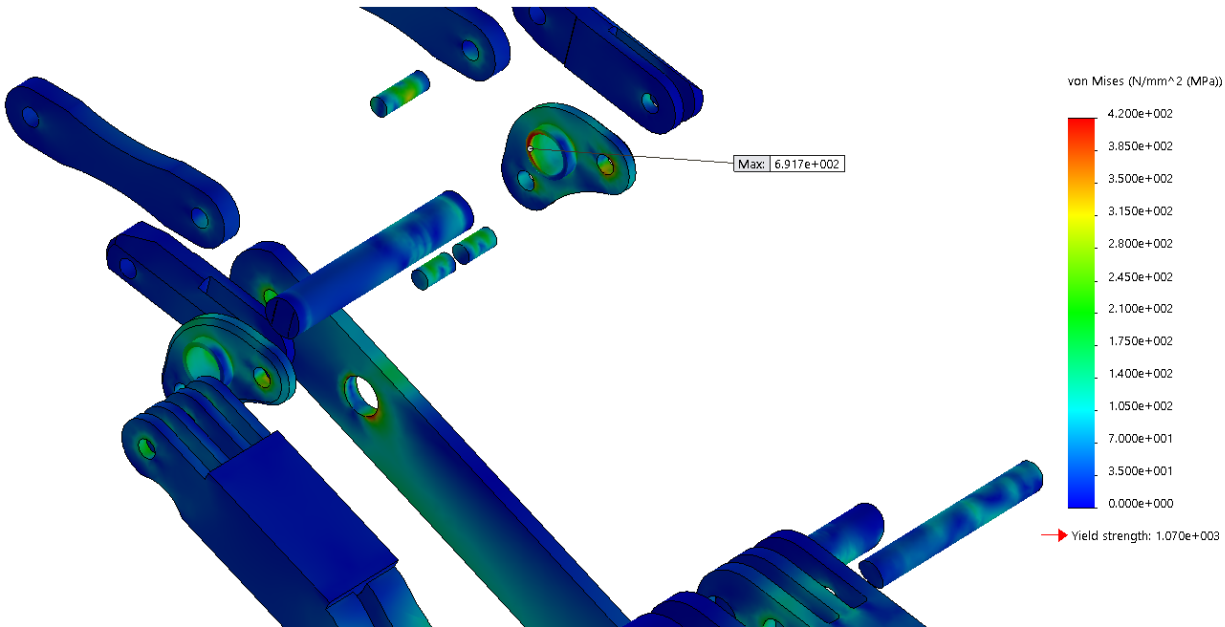


Figure 3.40: Close up of FEA at a minimum jaw opening.

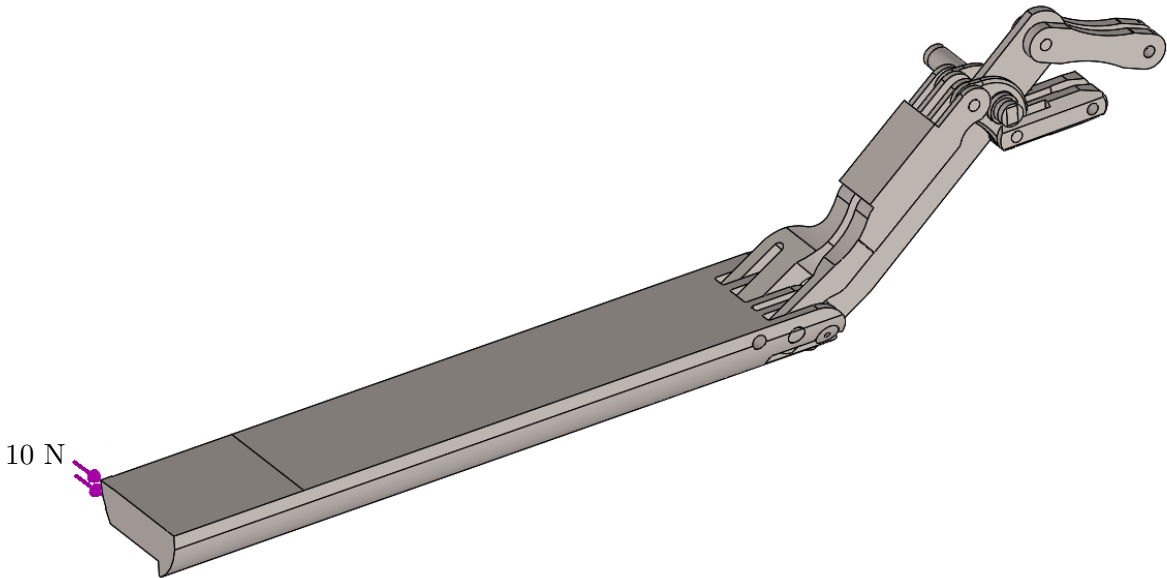


Figure 3.41: FEA model of jaw with a 10 N side load.

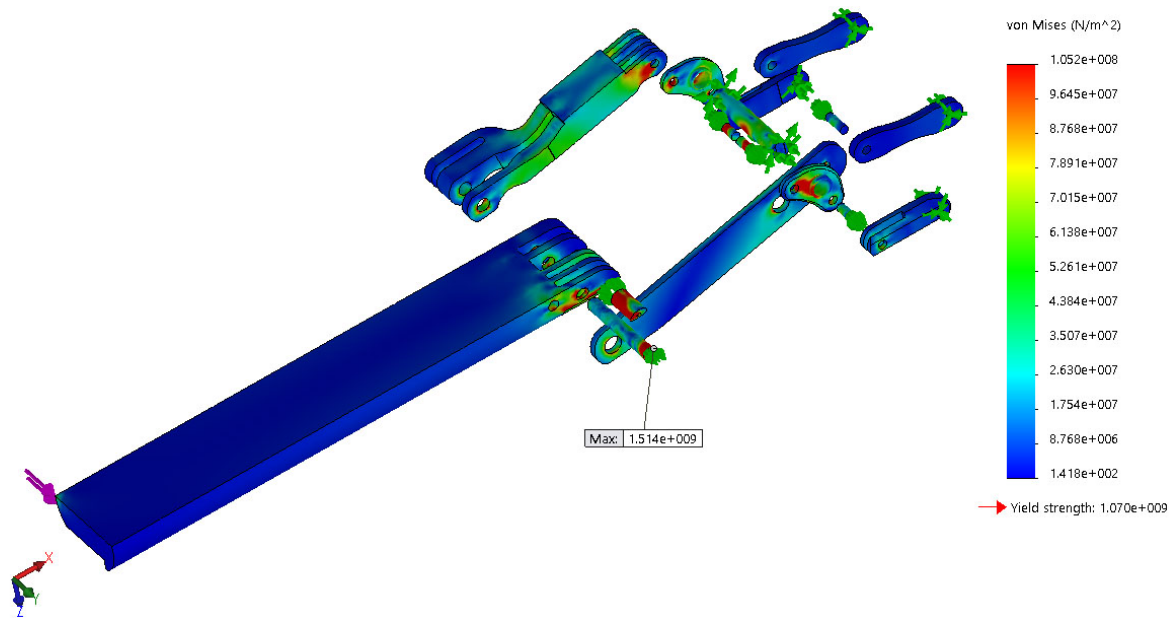


Figure 3.42: Side load FEA results.

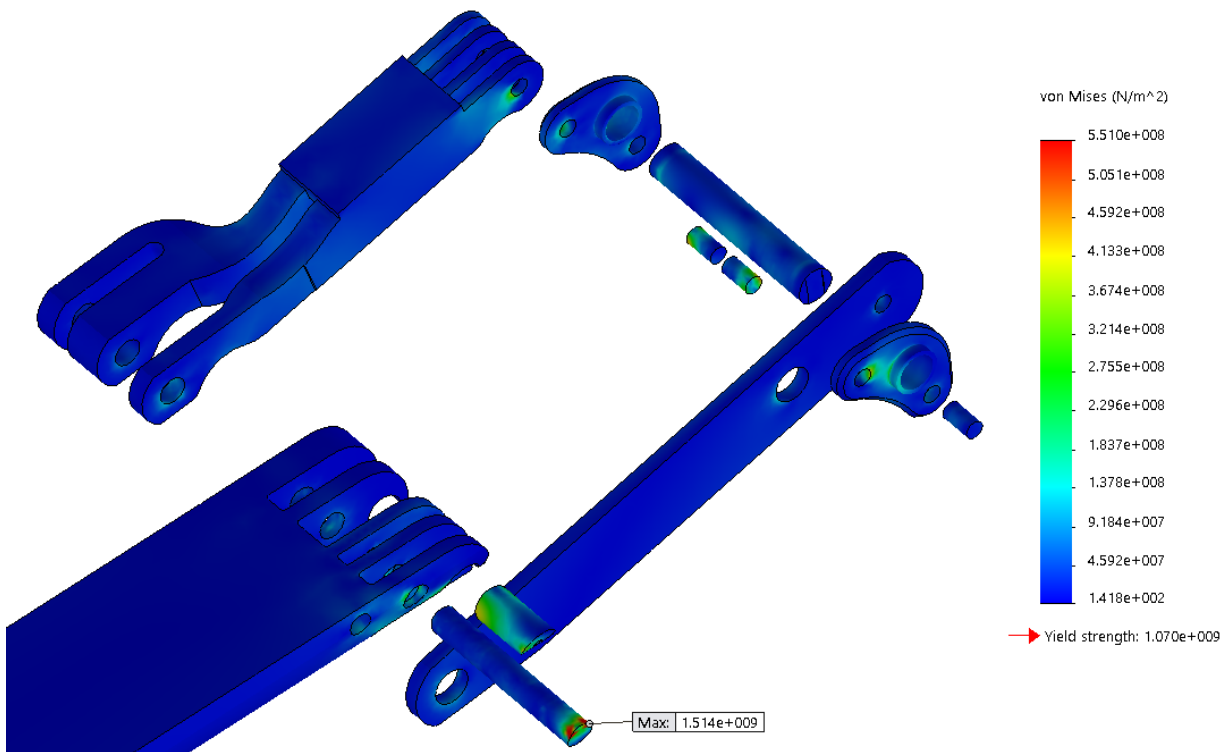


Figure 3.43: Side load FEA results with a modified stress map scale.

Although the results from the FEA can only serve as a guideline and require validation through testing of the instrument, it can still be concluded that a material with a yield strength of at least 1,400 MPa is required to provide the links with a factor safety of 2. However, the strongest material that is readily available in the market is Grade 5 titanium (Ti-6Al-4V), with a yield strength of 827 MPa. Stronger titanium alloys, ceramics and heat treated metals do exist with a yield strength exceeding 1,000 MPa, such as Ti-3Al-8V-6Cr-4Mo-4Zr. However, such materials are much harder to machine and require post-manufacturing processes that can distort the geometry of parts. For the purpose of validating the design, Grade 5 titanium was chosen as it is relatively cheaper, biocompatible [57], and easier to machine as compared to stronger materials. Although not ideal, a FOS of 1.2 is the highest rating that could be achieved for the links based on calculations from FEA stress results.

Once FEA was conducted on the links, reaction forces at the push rods and supporting shaft were determined. The largest forces occurred when the jaws were in a fully closed position (Figure 3.44). The maximum resultant force on the main support pin was 117 N, where 122 N acted along the X-axis and 19 N along the Z-axis. On the other hand, the maximum resultant force on the push rods was 160 N, acting primarily along the negative X-axis (a compressive load). A load of 2 N or less was observed along the Y-axis, while a maximum load of 22 N was observed along the Z-axis. The loads along the Y- and Z-axes are considered insignificant as compared to the main axial load and suggest minimal bending of the push rods.

Using the calculated loads, FEA was conducted on the push rods and support shaft of the instrument (Figures 3.45 and 3.46). The setup of the FEA models is described in Appendix B.2 and B.3. Results from the FEA on the support shaft showed that a maximum stress of 85 MPa occurred near the distal and proximal ends of the support shaft while supporting a 10 N load at the tip of one jaw. Lower stresses were observed during palpation due to the cancellation of forces when both jaws are engaged. This analysis justified the use of 321 grade SS which is one of the strongest grades of SS available in the market that is also biocompatible [57]. Such a material would provide a buckling factor of safety of 14 and a yielding FOS of 2.4. Furthermore, results from FEA on the push rods revealed a maximum stress of 315 MPa. This justified the use of corrosion-resistant, and biocompatible [58], 17-4 PH SS for the push rods. This material has a

yield strength of 814 MPa, providing a buckling FOS of 9 and a FOS of 2.7 against yielding.

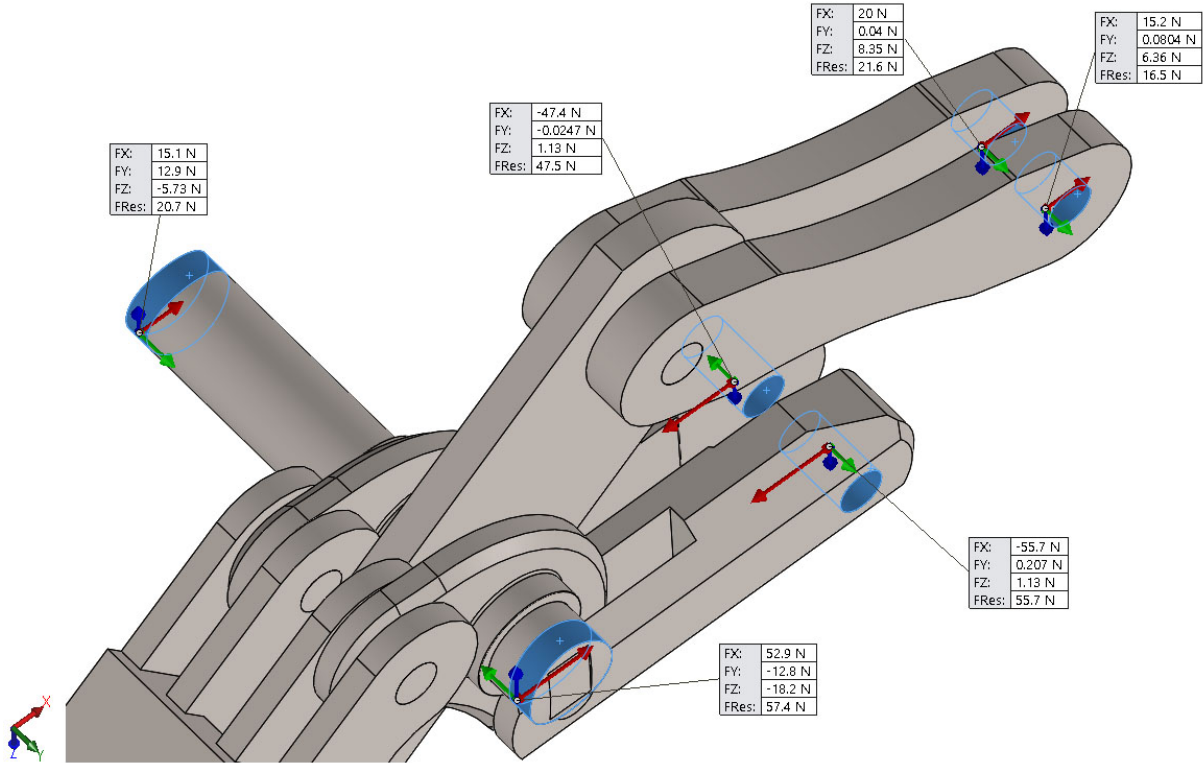


Figure 3.44: Reaction forces from SolidWorks.

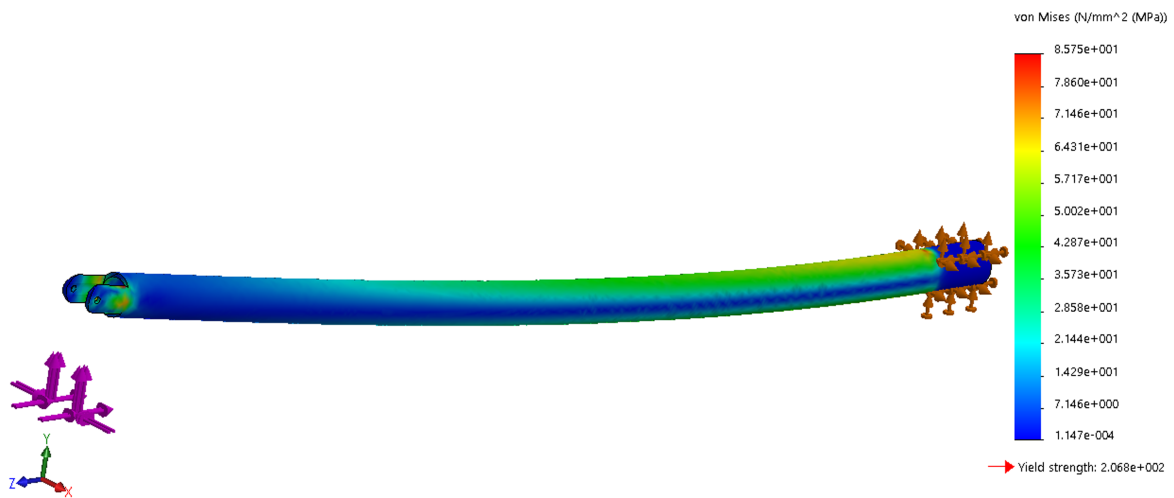


Figure 3.45: Results from FEA on support shaft. The top cover, base and sleeve are combined into one part.

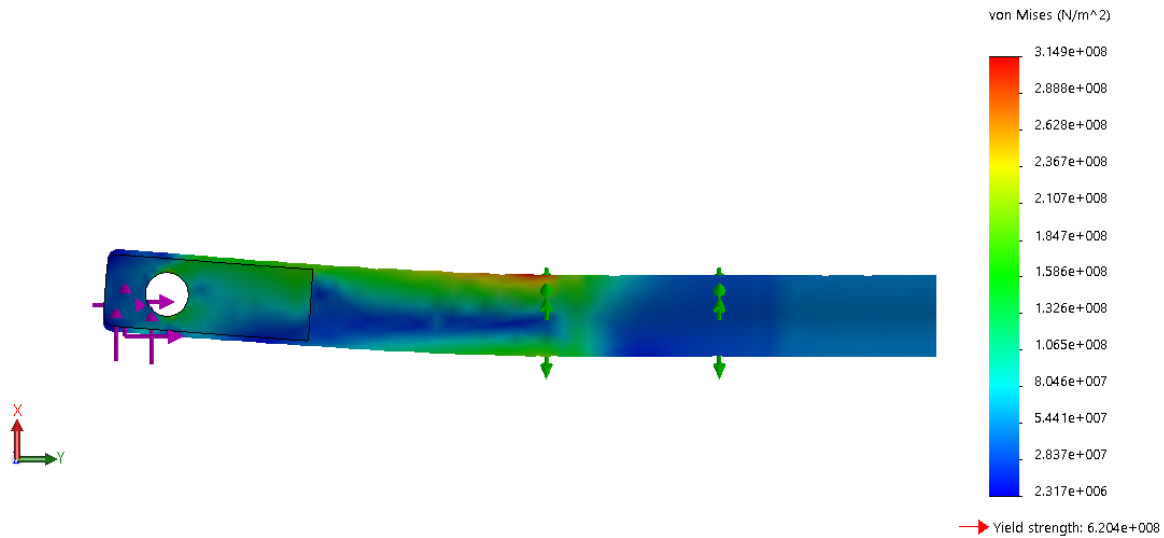


Figure 3.46: Sectioned view of push rod showing deformation at the distal end.

After analyzing the main components of the mechanism, FEA was also conducted on the pins holding the links together (Figure 3.47). The FEA determined that the highest stress experienced by the pins is around 550 MPa, as described earlier for the side-loading conditions, while a maximum stress of 312 MPa is experienced in normal loading. These high stresses made it difficult to choose a material for the pins. Currently, the strongest pins available in the required size are made of 316 SS which has a yield strength of 290 MPa. Although, based on FEA, this material would fail, for prototyping purposes, 316 SS would work well if loading conditions do not exceed 5 N of side load or 9 N of normal load. Testing can be conducted on the prototype to verify the FEA results and determine the load capacity of the instrument. If 316 SS proves to be strong enough to support the required loads, it would be a good choice of material as it is biocompatible and is one of the most widely used materials for biomedical applications.

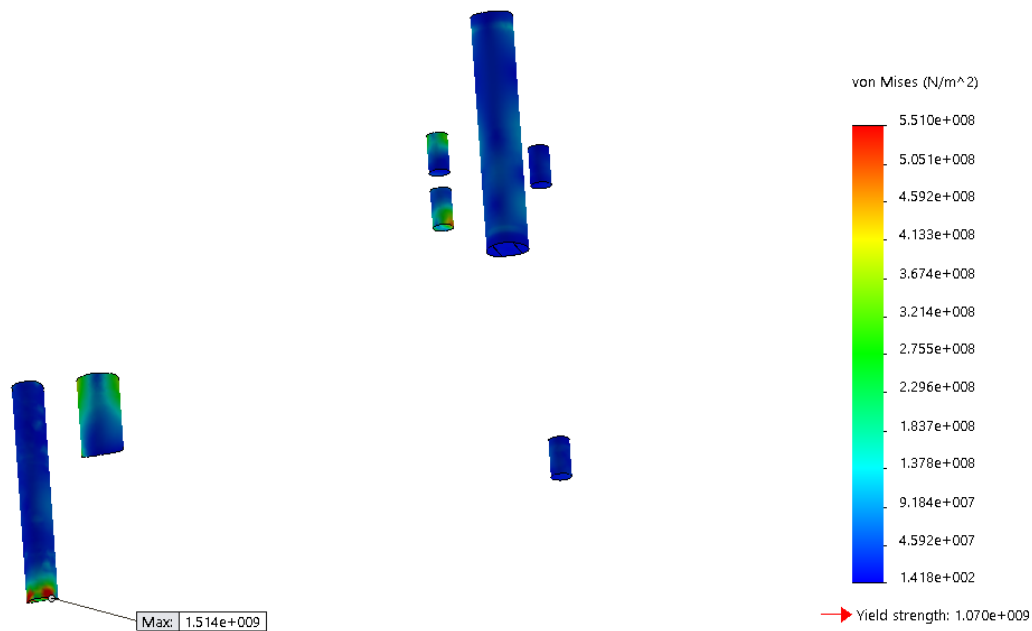


Figure 3.47: Results from FEA on pins highlighting high stress locations.

3.5 Machining Process

One of the design objectives was to create a tool that can be easily manufactured. All the designed parts are simple enough to be machined on standard machines such as a lathe and mill (Figures 3.48 and 3.49). Smaller parts, such as the links and keyways (Figures 3.50, 3.51, and 3.52), were easily made through electrical discharge machining (EDM) (Figures 3.53). For simplicity and to save manufacturing time, some parts were also 3D printed out of ABS plastic. These parts included the push rod guides as well as the joystick housing on the handle. Since these parts do not support any large loads, their strength is not vital for the functionality of the device. However, bronze push rod guides would have potentially been much more effective due to the ability of bronze to reduce friction and wear. It would be much more difficult to machine push rod guides from bronze due to the complex geometry of the guides. Therefore, 3D printing was chosen for validation purposes and the plastic guides proved to work well during the testing phase of the project. Given the success of the machining and assembly phase of the project, the simplicity and feasibility of the design was verified.



Figure 3.48: CNC mill machining a link.

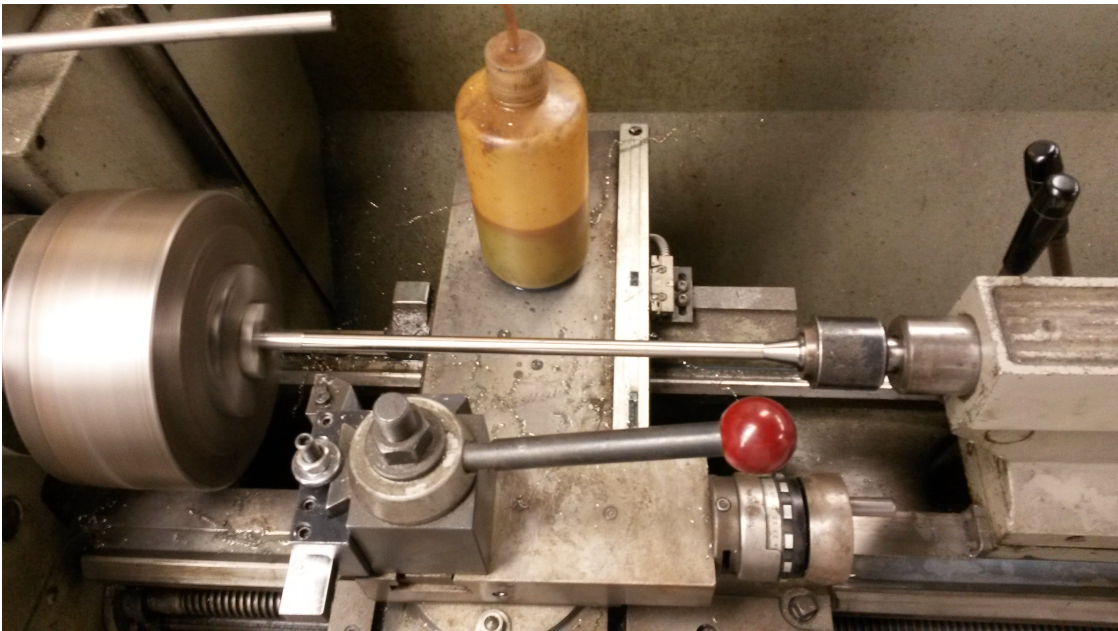


Figure 3.49: Lathe setup for machining tool support shaft.



Figure 3.50: Small links machined with wire EDM.

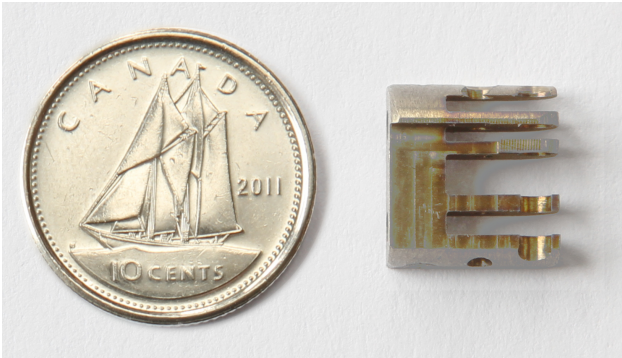


Figure 3.51: Jaw holder machined with wire EDM and CNC mill.

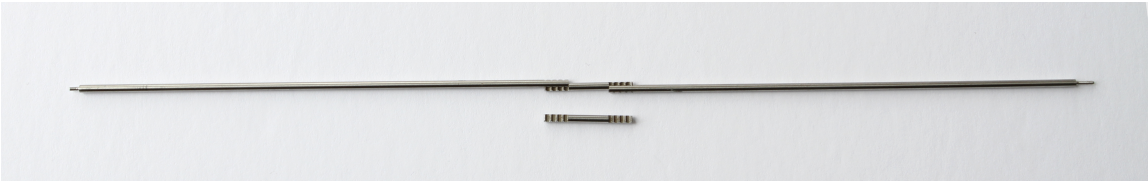


Figure 3.52: Machined keyway and key.

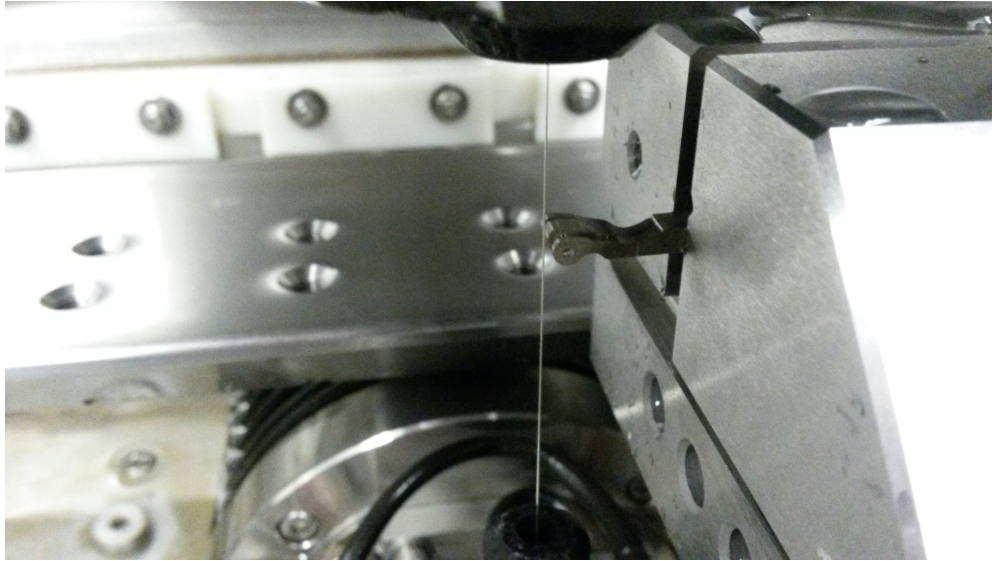


Figure 3.53: Wire EDM setup.

3.6 Conclusions

An iterative design process resulted in a novel three DOF minimally-invasive palpation device, named Palpatron. The end effector of the device consists of two jaws that support an ultrasound and a tactile sensor. Two series of links that are held together using pins support each jaw. The links are actuated with push rods that are contained within a 12-mm cylindrical shaft. Ball lead screws at the handle of the instrument control push rod movement, and each lead screw is controlled by one motor. The support shaft, along with the push rods and links, can be easily removed from the rest of the instrument via a keyway mechanism. In addition, very few fasteners were used in the design and most components are fastened to one another via a quick-release mechanism. The ability to easily separate the proximal and distal ends of the instrument allows for sterilization of the end effector.

The device was designed to hold a 10 N load in a multitude of configurations. In order to determine which materials would be suitable for the design, FEA was conducted on the major components of the tool: the end effector, support shaft, push rods, and pins. It was concluded that Grade 5 titanium was best suited for the linkage mechanism, although it could only provide a FOS of 1.2. Similarly, 321 grade SS was selected for the support shaft and can provide a buckling

FOS of 14 and a yielding FOS of 2.4. 17-4 PH SS was selected for the push rods and can provide a buckling FOS of 9 and a FOS of 2.7 against yielding. Lastly, 316 SS was selected for the pins; however, FEA results suggested that this material would fail under the required loads, thus testing is required to verify whether 316 SS is sufficiently strong. All of the materials selected for the design are biocompatible and are readily available.

Once materials were selected, the tool was manufactured using standard machines such as a lathe and mill. Smaller parts were manufactured by wire EDM. With the successful implementation of the Palpatron, the performance of the design can be determined. The ability of the design to meet the design specifications will be explored in the next chapters.

Chapter 4

Electronics and Control System Design

This chapter discusses the implementation of a manual control system for the designed tool. The forward and inverse kinematic equations are presented and validated in this chapter, establishing the first steps towards a fully automated device.

4.1 Semi-Automated Control

This section describes the manual control system that was implemented for the device using a PIC and two analog joysticks. The actuator selection process, and backlash and hysteresis characteristics are also presented.

4.1.1 Actuator Selection

Three methods for actuating the linkage system were considered: electrical motors, pneumatics and hydraulics. Pneumatic actuators operate using an external source of pressurized air, while hydraulic actuators use pressurized, non-compressible fluid to transfer forces between two points within a closed system. Both systems are purely mechanical and require special fittings and passage lines to ensure proper function. Such components are relatively large and would greatly complicate the design. Both systems pose a great risk to patients as they are prone to leaks that

can contaminate a surgery. However, these actuation methods have a high ratio of load capacity to size of fluid or air line. Fluid lines of 6 mm in diameter can support an axial load of over 4,000 N, while electrical motors of similar size, without a gear head, can support less than a newton at most.

Similarly to pneumatic and hydraulic systems, electrical motors are available in many forms and sizes, but rely on electrical power to function. The main advantage of electrical actuation is ease of integration with other electronic systems and implementation of autonomous control. Hybrid systems, consisting of a hydraulic–electric or pneumatic–electric actuators, are available, but would add unnecessary complexity if a solely electrical actuation is feasible. Therefore, for simplicity, a purely electrical actuation system was used. Such a system would allow for autonomous control of jaws either based on data input from jaw–sensors or from user input. Enabling autonomous control would also make it possible to integrate the tool with other robotic systems.

Based on SolidWorks FEA simulations, it was determined that a maximum axial load of 200 N is supported by push rods when a 10 N load is applied to the tip of a jaw. Therefore, a motor that can provide a continuous actuating force of at least 250 N is required. A higher rating is preferred in order to compensate for friction within the tool. Two forms of electrical motors were considered: linear and rotary. A linear motor has a flat actuating mechanism that produces a linear force along its length. In contrast, a rotary motor has an actuating mechanism that is arranged into a continuous loop and can produce a continuous torque. Unlike linear motors, rotary motors can be equipped with a spindle drive and a gearhead that can amplify the torque output from the motor and convert it into a linear actuating force. Consistent with the compact handle design requirement, linear actuation would be optimal to actuate the push rods.

Two possible motor options were considered that meet the required design specification. The first option is an EC, 16-mm diameter, brushless motor with hall sensors, from the company Maxon Motors® (Part #: 395588). The motor is equipped with a preloaded-ball-screw spindle drive, capable of supporting a maximum 370 N in dynamic loading (Part #: 424752). The motor also has a 512 counts per turn encoder with three channels (Part #: 201940) and is controlled by a 2 A, 9 to 24 V-DC digital motor positioning controller (EPOS2 24/2, Part #: 380264). This selected setup has an 850:1 gearhead with a spindle that can provide an axial accuracy of 0.046

mm and a maximum feed velocity of 0.5 mm/s. Such specifications would exceed the minimum requirements for the intended control system.

The second possible option was a rotary motor from Micromo[®] (Part #: 1628T012BK313IE2-1024+15/10 750:1+MG10). This motor has very similar specifications to the Maxon[®] EC motor however, lead screws and gearhead combinations available from Micromo[®] cannot support the required design loads. Therefore, a lead screw was selected from Haydon Kerk[®] that can support up to 340 N in dynamic loading. Due to uncertainties in compatibility between the motor and lead screw, as well as bulky design, this option was discarded. Instead, four Maxon[®] motor assemblies were used and placed at the proximal end of the instrument, as described in Chapter 3.3.3.

4.1.2 Control Implementation

This section describes the hardware and software used to create the manual automatic control system for the Palpatron. All the physical components of the system (hardware) and their function, and the code required to implement the manual control system (software) are described.

4.1.2.1 Hardware

The implemented control system relies on input from two joysticks and a push button to control jaw motion. The joysticks can be used to move the jaws, while the button initiates a homing sequence. Due to the lack of heavy data processing in the proposed control system, strong computing powers were not required for the manual control of the instrument. In order to increase the portability and ease of use of the instrument, the use of a PC was avoided and only a PIC microcontroller was used to implement manual control. Arduino and Raspberry Pi programmable boards were also considered, but the stock boards lack sufficient analog and digital inputs and outputs, and are much bigger in size as compared to a PIC.

A dsPIC33FJ64MC802, from Microchip[®], was used to read inputs from the two analog joysticks and the push button. The microcontroller was programmed to resolve the analog inputs from the joysticks as a 12-bit value. Under this configuration, the microcontroller assigns a value to a variable in the range of 0 to 3.1 that is proportional to an input voltage from the joysticks that ranges from 0 V to 3.1 V. It was observed that signal outputs from different joysticks are

consistent and similar enough to allow the same code to be implemented for any joystick. A similar approach could have been implemented for the push button, but a simpler digital signal was used instead, where 3.3 V is considered a high logic level.

In order to communicate with the motor controllers, a custom command library was created to facilitate serial communication between the PIC and EPOS2 motor controllers, in a master-slave configuration. In this configuration, the master (PIC) can send direct commands to the slave (one EPOS2 controller), or other controllers through the slave via a CAN-open interface that connects all the EPOS2 controllers together. Although a communication library is available from Maxon Motors[®], it is written in C++ language which was not compatible with the PIC at the time the control system was constructed. The PIC is programmed by low level machine language using a C-language-based program, MPLAB X IDE. The program now also supports C++.

The serial communication with the EPOS2 controllers was configured using a baud rate of 115200, 8 data bits, no parity, and 1 stop bit. One motor controller acted as the main communication interface while the other motor controllers were connected in a daisy-chain configuration to the first controller, each having an assigned node. Motors on nodes 1 and 2 control the tactile sensor jaw while the motors on nodes 3 and 4 control the ultrasound jaw.

4.1.2.2 Software

A source file was created, and it contained the main program for the control system, as well as various functions that implemented serial communication between the PIC and the motor controllers. The logic of the coded program is briefly described in Figure 4.1. The program starts with the initialization of several variables and functions after which the EPOS2 controllers are enabled in the “main” function. The controllers are set to “Profile Velocity Mode” and are placed under a quickstop. A quickstop is an EPOS2 command that prevents motor movement, even if a “go” signal is received by the motor controller. A controller needs to be changed to an active state before it can initiate motor movement.

Once the controllers are enabled and in the quickstop state, the program enters an infinite loop in which it is constantly checking for input from two joysticks and one push button. The program exits the loop if an error message is received from the motor controllers or communication times

out. The timeout was set to 150 ms. Within the loop, there is a homing sequence that is triggered by the press of the push button. If initiated, the home position of the device is determined based on mechanical stops within the instrument and using a current threshold trigger. For the homing sequence to work properly, the jaws need to be able to fully close, one at a time, without colliding into one another. This means that the jaws need to be opened up prior to initiating the homing sequence.

During the homing sequence, four homing positions are determined that correspond to the two DOF of each jaw. First, the bottom jaw closes, until a mechanical limit is reached at which point there is a spike in motor current and the position is defined as 'home'. Once the first home position is determined for the bottom jaw, it is opened so that the first home position can be determined for the top jaw. Next, the pitch of the bottom jaw is changed so that the jaw opens outwards in order to find the home position for the second DOF. The second DOF for the top jaw is determined in a similar manner. Once homing is completed, limits to jaw motion are enabled.

Although the homing sequence proved to work properly, it is not very consistent due to friction within the tool. Variable friction between the links of the jaws can cause the home position to be underestimated and may lead to tool and motor damage as the motors can overpower the mechanical stops. Therefore, caution needs to be taken by the user to ensure proper instrument control.

In addition to monitoring input from the push button, the while loop within the main function continuously monitors for input from the joysticks. Four cases are implemented for each joystick DOF. Moving the joystick up and down or left to right generates the 0 to 3.1 V range. If the observed input is greater than 2.9 V and a quickstop is not enabled, the corresponding motor starts moving at 4000 rpm, closing the jaw or rotating it in an inwards direction. Similarly, when input is less than 0.9 V motors move at -4000 rpm, opening the jaw or rotating it in an outwards direction. Joystick controls are summarized in Table 4.1. From the table it is possible to see that when the jaws open and close, there is also a slight change in jaw pitch. If homing is completed, motor movement is limited to -4000000 quadrature counts (qc) which is equivalent to about 4 mm of linear motion. A limit of 1750000 qc (1.75 mm) was not yet implemented for the motors controlling jaw pitch due to inconsistencies with the homing sequence.

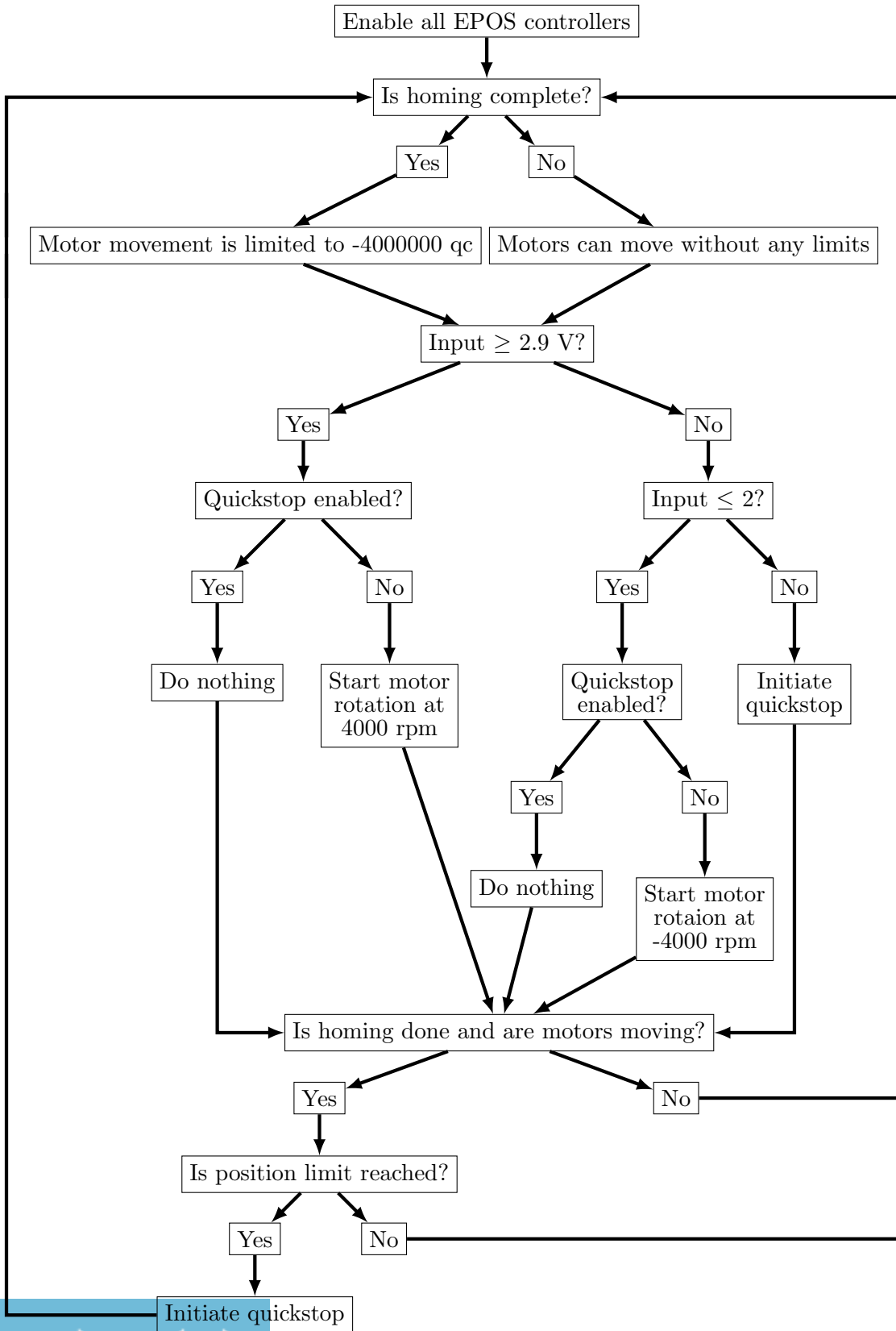
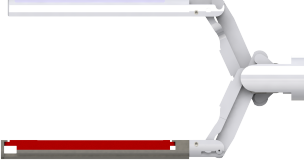


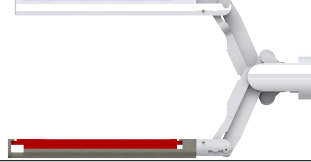
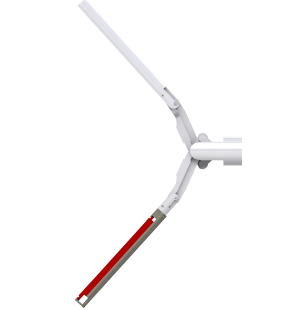

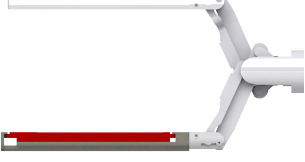
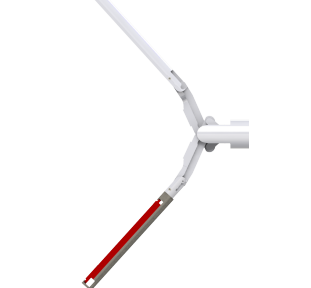


Figure 4.1: Jaw control sequence.

Table 4.1: Joystick control summary.

Joystick movement	Effect on jaw	Starting position	Ending position
Up	Close		
Down	Open		
Left	Angle inwards		
Right	Angle outwards		

The implemented control system exhibited unnoticeable delay between joystick movement and motor movement. A custom printed circuit board (PCB) was created to house all of the electronic components of the system. Toggle switches were used to provide power to motors and PIC separately, thereby providing means to restart the system without affecting any predetermined homing positions (Figure 4.2). The PCB is 74 mm wide, 74 mm long, and 44 mm tall. It is of a comparable size to other commercially available programmable boards but has many more capabilities, a lower price, and more features.

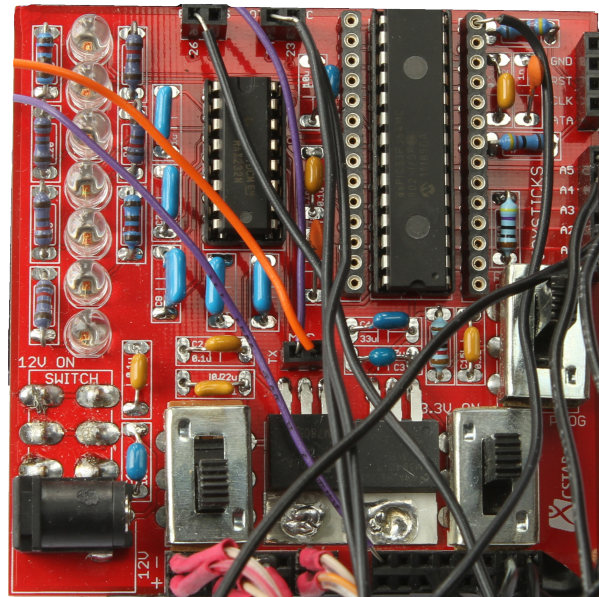


Figure 4.2: Custom PCB with all the electronic components required to actuate the Palpatron.

4.1.3 Quantifying Jaw Backlash and Hysteresis

Due to small inaccuracies in the manufacturing of links, and inherent material deformation, some backlash exists in the prototype of the instrument. To estimate jaw backlash, the instrument was clamped to a solid base with the clamp holding down the handle of the instrument. Two dial indicators were used to measure shaft and jaw deflections (Figures 4.3 and 4.4). In the first setup, one dial indicator was configured to measure shaft deflection while the other measured jaw deflection. In the second setup, both dial gauges were placed on the jaw in order to determine the angular backlash specifically at the jaw.

Testing was conducted by incrementally adding 100 g weights to the tip of the jaw, up to a load of 700 g. Dial displacements were recorded at each weight increment. Weights were then incrementally removed to determine any hysteresis in the system. It was determined that when a 700 g load is placed at the tip of the jaw, the shaft deflects 0.32 degrees, about 2 mm of vertical displacement of the tip of the jaw. The backlash observed at the shaft is mainly due to poor material selection. The main part supporting the shaft was 3D printed out of plastic in order to save on manufacturing costs and time (Figure 4.5). Once loads were placed on the jaws, the

3D printed part permanently deformed where the captive pins are located and was not able to hold the pins tightly. The deformation accounted for an additional 1.4 degrees, 5 mm vertical tip displacement, of no-load-play. The deflection observed in the shaft can be minimized by machining the part out of a stiffer material, such as metal.



Figure 4.3: Shaft and jaw deflection measurement setup.



Figure 4.4: Jaw deflection measurement setup.

While under a 700 g load, the jaw, by itself, only deflects about 2 degrees, 1.5 mm of vertical displacement of the jaw tip. Therefore, there is a total of 3.5 mm vertical deflection of the tip of the jaw when a 700 g load is applied. Considering that the optimal palpation force is 4 N (about 400 g), the testing results show that under normal operating conditions, there will be at least a 25% reduction in jaw deflection (Figure 4.6). Deflection will be further reduced during palpation as the force will be distributed over a larger surface area rather than being a point load at the tip of the jaw.

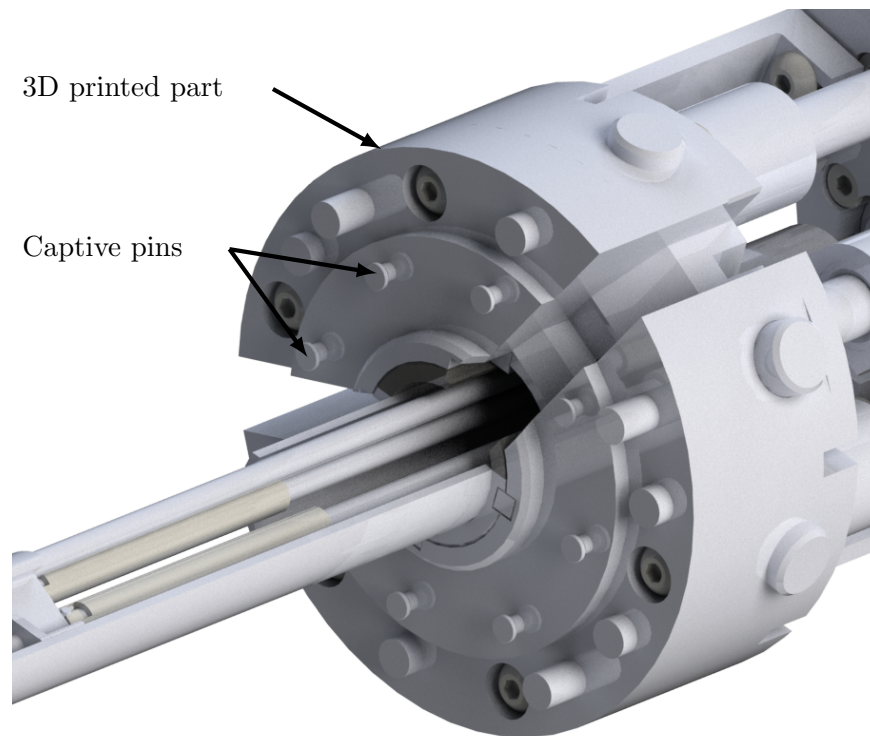


Figure 4.5: Captive pins that hold the sleeve of the instrument.

Although backlash and hysteresis are present in the system, results have shown that such parameters are consistent between trials and can be related to applied load using simple quadratic functions as shown by the dotted lines in Figure 4.6. A maximum standard deviation of 0.24° for jaw orientation or 0.50 mm of vertical displacement was observed between five trials conducted for each incremental weight stage. The biggest spread occurred for jaw orientation between the addition and removal of weights, accounting for 0.72° , 0.90 mm of vertical displacement, at 300 g.

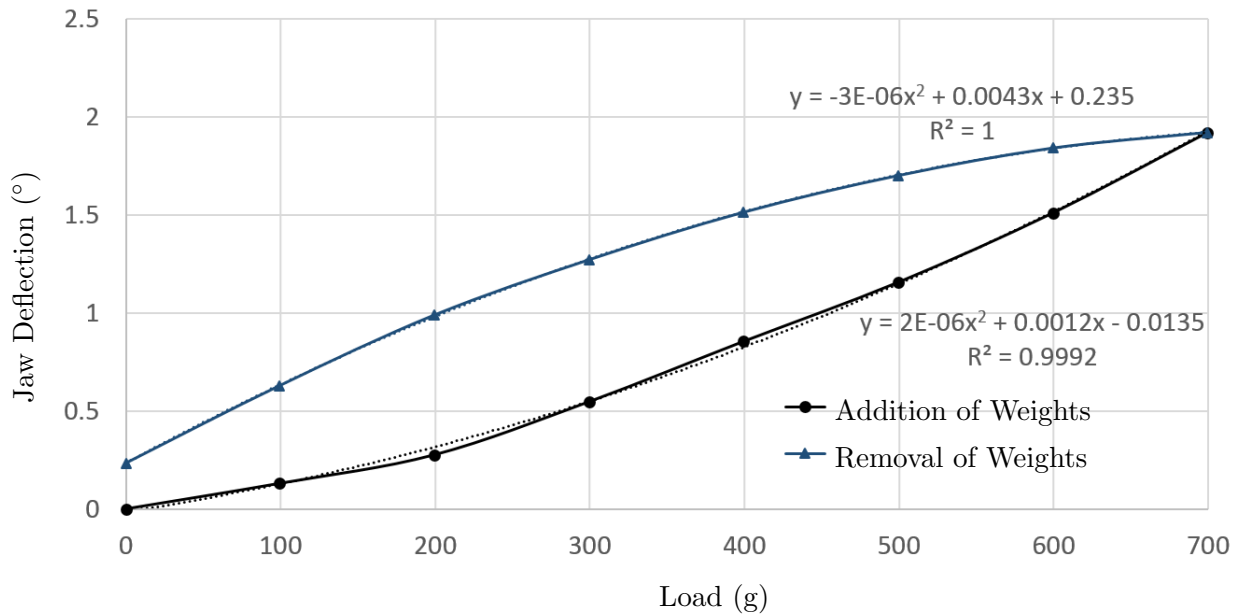


Figure 4.6: Effects of jaw load on angular position of the jaw.

The non-zero intercept for the unloading of weights from the jaws is caused by play in the shaft of the instrument, not from plastic deformation of the support shaft. The shaft was physically moved to a zero position at the beginning of each trial to ensure consistent starting positions for deflection measurements. Values from three consecutive trials were identical.

Furthermore, sideways-play in the jaws was also investigated (Figure 4.7). Although sideways-play does not directly relate to the control system, it may result in unwanted jaw motion. It was determined that when an inwards load of 500 g is applied, the jaw deflects sideways by 3 mm. When the same load is applied outwards, there is over twice the amount of deflection, about 7 mm. This effect is due to the interaction between Link 8 of each jaw. The links support each other while supporting inward loads. Less than 0.1 mm of jaw motion was measured perpendicular to the load direction, suggesting minimal effects of side load on jaw motion.

Even though significant backlash and jaw deflection under loading were present, such factors did not adversely affect the manual control of the jaws. Using the implemented control system, a phantom tissue was grasped with a force of 4 N, and object maneuvering tasks were successfully completed as described in Chapter 5.3.



Figure 4.7: Sideways jaw loading setup with an inwards applied load.

4.2 Forward Kinematics

Although not implemented as part of this thesis, one of the future goals for this design is to implement an automated control system. In order to do so, the forward kinematics for jaw motion need to be determined. To derive the forward kinematics, a coordinate frame was constructed (Figure 4.8), centered at the main support pin. Using lines to represent the links, a kinematic model for jaw position was created to facilitate equation derivations (Figures 4.9 and 4.10). For simplicity, only one jaw was modeled due to independent jaw movement. In-depth derivations of the kinematic equations is presented in Appendix C. The derivations yield three main equations that can be used to model jaw motion:

$$\sqrt{l_8^2 - (M \sin \theta_h + N \cos \theta_4 + I)^2} - K \sin \theta_h + I \cos \theta_h + J = 0 \quad (4.1)$$

$$h_{1,y} = |l_3| \sin \theta_G + A \sin \theta_h - B \cos \theta_h \quad (4.2)$$

$$h_{1,x} = O \sin \theta_h + P \cos \theta_h + Q \quad (4.3)$$

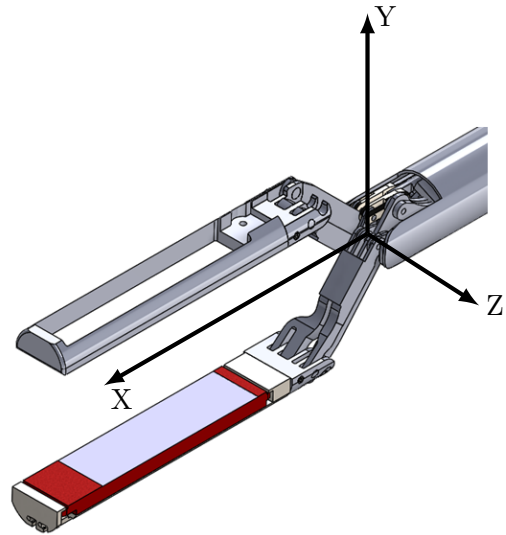


Figure 4.8: Coordinate system for jaw mechanism.

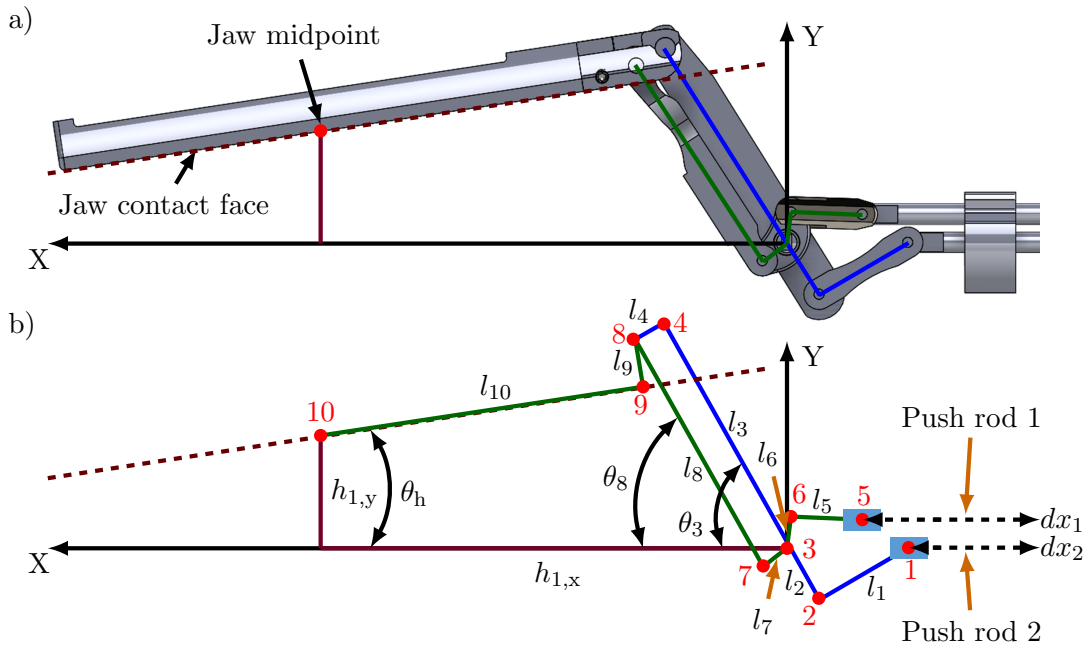


Figure 4.9: Kinematic model of jaw mechanism: a) Conversion of the 3D link model to a 2D representation. b) Complete 2D kinematic model.

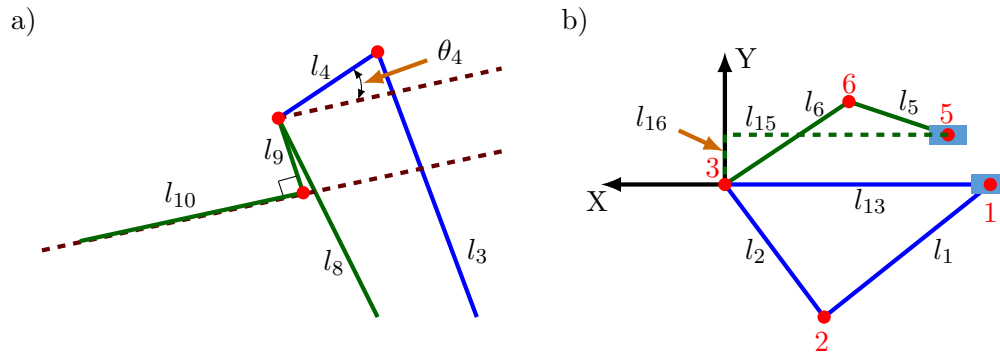


Figure 4.10: a) Detailed view of Link 4 and 9 angles. b) Detailed view of push-rod links.

The derived equations can be used to calculate three variables, θ_h , $h_{1,y}$, and $h_{1,x}$, that describe the orientation of the jaw. As shown in Figure 4.9, θ_h is the angular pitch of the jaw, $h_{1,y}$ is the vertical distance from the centerline of the instrument shaft to the midpoint of the jaw, and $h_{1,x}$ is the horizontal distance to the midpoint from the main support pin. The jaw midpoint was arbitrarily selected for the purposes of kinematic equation derivation. Any point along the bottom surface of the jaw can be selected. θ_h , $h_{1,y}$, and $h_{1,x}$ depend on the position of the push rods, dx_1 and dx_2 . Due to the complexity of jaw motion, a closed form expression for θ_h could not be derived. θ_h needs to be numerically approximated and is used to determine $h_{1,y}$, and $h_{1,x}$. The terms A , B , K , O , and P are constants while θ_G , I , J , and Q are variables that depend on push rod position. Table 4.2 provides a summary of all the constants and variables used in the kinematic equations.

4.3 Inverse Kinematics

Using Equations (C.11), (C.12) and (C.13), derived in Appendix C.2, and the angular position and height of the jaw, push rod positions can be determined. Based on these equations, we have the following constants: A , B , K , L , M , N . We can then solve for θ_G using Equation (C.11):

$$\theta_G = \sin^{-1} \left(\frac{h_{1,y} + B \cos \theta_h - A \sin \theta_h}{|l_3|} \right) \quad (4.4)$$

Table 4.2: Summary of variables and constants that can be used to solve the kinematic equations.

Constants		Variables	
Symbol	Value	Symbol	Expression
l_1	10.09 mm	l_{13}	9.6 mm $- dx_1$
l_2	6.00 mm	l_{15}	16 mm $- dx_2$
l_3	22.50 mm	C	$\frac{l_{13}^2 + l_1^2 - l_2^2}{2l_1 l_{13}}$
l_4	3.36 mm	D	$\frac{\sqrt{4l_1^2 l_{13}^2 - (l_{13}^2 + l_1^2 - l_2^2)^2}}{2l_1 l_2}$
l_5	7.00 mm	E	$\frac{l_6^2 + l_{15}^2 + l_{16}^2 - l_5^2}{2l_6 \sqrt{l_{15}^2 + l_{16}^2}}$
l_6	3.00 mm	θ_F	$405^\circ - \tan^{-1}\left(\frac{l_{16}}{l_{15}}\right) - \cos^{-1}(E)$
l_7	3.00 mm	G	$\sin^{-1}(D) - \cos^{-1}(C)$
l_8	22.80 mm	H	$ l_7 \sin \theta_F$
l_9	1.73 mm	I	$ l_3 \cos \theta_G - l_7 \cos \theta_F$
l_{10}	31.47 mm	J	$H - l_3 \sin \theta_G$
l_{16}	2.75 mm	Q	$ l_3 \cos \theta_G$
θ_4	22.75°		
A	34.57 mm		
B	3.03 mm		
K	-3.10 mm		
L	1.30 mm		
M	1.30 mm		
N	3.10 mm		
O	3.03 mm		
P	34.57 mm		

With a value for θ_G , we are able to create a numerical solution for variable θ_F and use it to solve for l_{15} :

$$\sqrt{(l_8^2 - (M \sin \theta_h + N \cos \theta_h + |l_3| \cos \theta_G - |l_7| \cos \theta_F)^2)} + K \sin \theta_h + L \cos \theta_h + |l_7| \sin \theta_F - |l_3| \sin \theta_G = 0 \quad (4.5)$$

With a value for θ_F , we can numerically solve for l_{15} :

$$\left(\left(\frac{l_{16}}{l_{15}} \right)^2 + 1 \right) (l_6^2 + l_{15}^2 + l_{16}^2 - l_5^2)^2 - 4l_6^2(l_{15}^2 + l_{16}^2) \left(\left(\frac{l_{16}}{l_{15}} \right) \sin(405^\circ - \theta_F) + \cos(405^\circ - \theta_F) \right)^2 = 0 \quad (4.6)$$

Similarly to l_{15} , l_{13} depends on θ_h and $h_{1,y}$. l_{13} can be numerically approximated using the following expression:

$$\frac{h_{1,y} + B \cos \theta_h - A \sin \theta_h}{|l_3|} = \frac{\sqrt{4l_1^2 l_{13}^2 - (l_{13}^2 + l_1^2 - l_2^2)^2} (l_{13}^2 + l_1^2 - l_2^2 - \sqrt{4l_1^2 l_2^2 - 4l_1^2 l_{13}^2 + (l_{13}^2 + l_1^2 - l_2^2)^2})}{4l_1^2 l_2 l_{13}} \quad (4.7)$$

Once a value for l_{15} and l_{13} is determined, dx_1 and dx_2 can be calculated and will correspond to the incremental change in horizontal position of each push rod that is required to achieve the desired jaw orientation.

4.4 Conclusions

An intuitive, manual control system was designed that incorporates two joysticks, a push button and four motors. The motors are controlled by relaying joystick input to motor controllers via a PIC using serial communication. The implemented control system allows the user to open and close the jaws as well as change their pitch. Homing and safety features are implemented to prevent damage to the tool.

Preliminary tests conducted on the tool demonstrated that the jaws have a total vertical backlash of 3.5 ± 2.5 mm, measured from the tip of the jaw. The backlash is consistent and can be approximated based on the applied load. Hysteresis within the system further reduces jaw motion accuracy and adds a positional error of as much as 0.9 mm. Due to the nature of the control system, errors in jaw position due to backlash can be compensated by visual inspection. Tool-tissue forces and data from tactile sensors can also be used to correct for jaw backlash.

In order to provide the ability to implement autonomous control, a kinematic model for the tool was created. Based on the model, the forward and inverse kinematic equations for jaw motion were derived. Three governing equations were derived and validated for forward kinematics which then allowed the inverse kinematic equations to be derived. It was determined that although there is no explicit solution to the governing equations, they can be numerically approximated using a known jaw orientation or push rod position.

Chapter 5

Prototype Testing and Validation

This chapter describes the experimental setup used to test the manufactured prototype and validate the design. The load carrying capacity of the Palpatron is validated, and the ability to measure tool–tissue forces is explored. The grasping capabilities and object manipulation abilities of the instrument are also presented.

5.1 Experimental Setup

To test the structural rigidity of the design, the instrument was clamped to a wooden base. A point load was placed at the tip of one jaw, along its centerline, using a hooked weight rack. Small and light retainers were placed on the jaw to prevent the weight rack from sliding off, and to ensure consistent loading conditions. In order to investigate the ability of the tool to measure tool–tissue forces, strain gauges were placed on Link 8. Link 8 is the closest link to the jaws, and the ability to sample strain near the jaws helps minimize non-linearities in tool–tissue force measurement. Strain was measured at two locations on Link 8, as shown in Figure 5.1. Gauge 1 was placed near the centre of the jaw, where stresses were predicted, using FEA, to be lower. It was expected that Gauge 1 would be less sensitive to side loads on the jaws and would be able to better approximate tool–tissue forces. Gauge 2 was placed closer to one of the pins on Link 8 in case reliable measurements could not be attained from Gauge 1. Based on FEA, the stresses near the pin would be higher than stresses at the location of Gauge 1. The strain gauges were

connected, using two separate quarter bridge configurations, to a Micro Measurements[®] P3 Strain Indicator and Recorder (Figure 5.2).

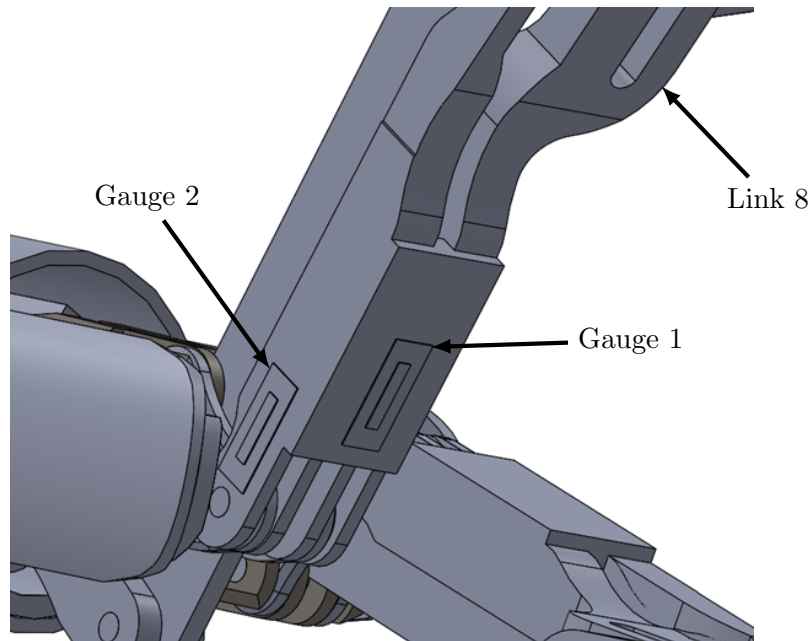


Figure 5.1: Strain gauge locations.

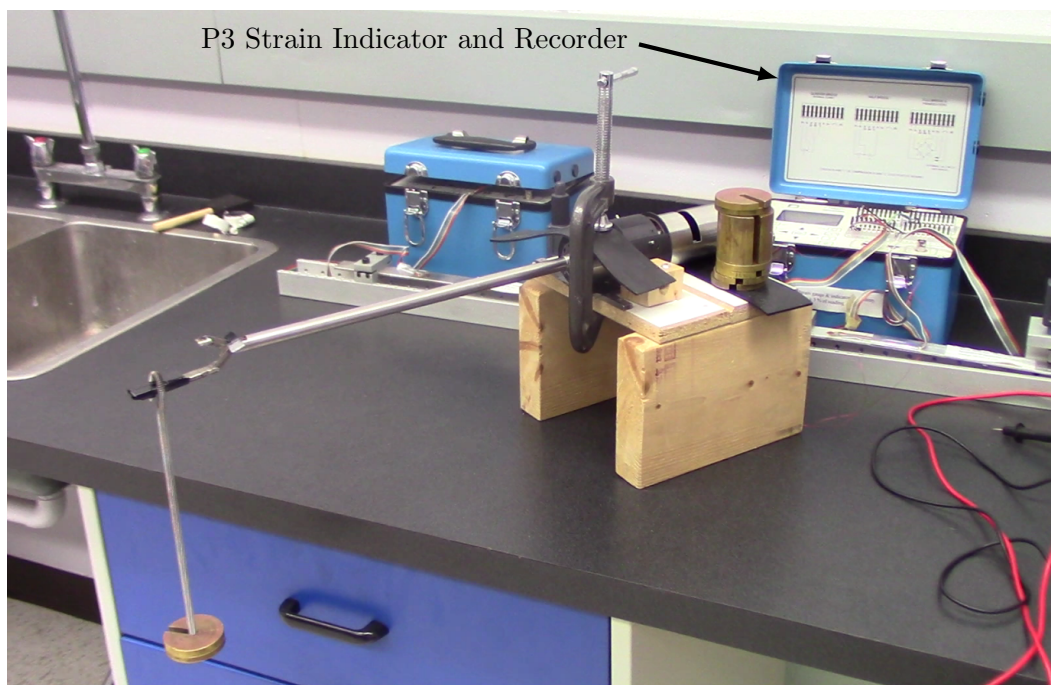


Figure 5.2: Experimental setup for strain measurements.

5.2 Load Carrying Capacity and Strain Measurement

The load carrying capacity of the instrument was tested by placing 100 g weights at the tip of one jaw, up to a load of 700 g (7 N). Although the tool was designed for a 10 N load, a lower, conservative load was chosen for testing purposes to avoid accidental tool damage. Due to the cost of building the prototype and its uniqueness, the validation experiments were not conducted to failure. Before weights were added to the jaw, each strain gauge quarter bridge was balanced through the P3 device so that a strain of zero was measured. As weights were placed on the hooked rack, strain was measured for each weight increment. Figures 5.3 and 5.4 represent the data from six trials in which 100 g weights were loaded and unloaded from one jaw.

The data shows a non-linear relationship between strain and load, similar to previous published work in which tool–tissue forces are measured indirectly (Chapter 2.1.1). However, it can be seen that at loads above 200 g, the average stress is close to linear, suggesting that as loads increase, friction effects decrease. A nearly linear relationship also suggests elastic deformation of the link, which is the expected response from the loading conditions. The strain data also shows that while Gauge 1 has better repeatability, Gauge 2 has less hysteresis. Repeatability was measured as the standard deviation observed between all the trials for each weight increment. Hysteresis was measured as the maximum difference between the average strain for addition and removal of weights. Although crucial to the ability to measure palpation forces, a strain–load relationship for distributed loads was not explored. However, the data collected for a point load can still be used to calibrate the instrument in order to estimate tool–tissue forces. Based on measurements from Gauge 1, it would be expected that a 4 to 6 N palpation force, would correspond to a measured strain of 30 to 40 $\mu\epsilon$.

In a follow-up experiment, the dependency of measured strain on load orientation was investigated by moving a point load of 600 g medially and laterally across the jaw. Due to an asymmetric link design (Figure 5.5), loads are distributed differently between the links depending on the orientation of the applied load and its location relative to the center axis of the jaw. As a point load is moved towards the lateral or medial edge of the jaw, it induces a torque that can either increase or decrease the apparent load experienced by the strain gauges. It was discovered that

strain measured by Gauge 1 only deviated by $3.25 \mu\epsilon$ medially–laterally, while Gauge 2 deviated by $42.25 \mu\epsilon$. Therefore, Gauge 2 is very sensitive to load location across the jaw and any additional applied torques. Considering that the surface of the jaw is expected to be in full contact with tissue during palpation, the effects of jaw loading dependency will be minimized.

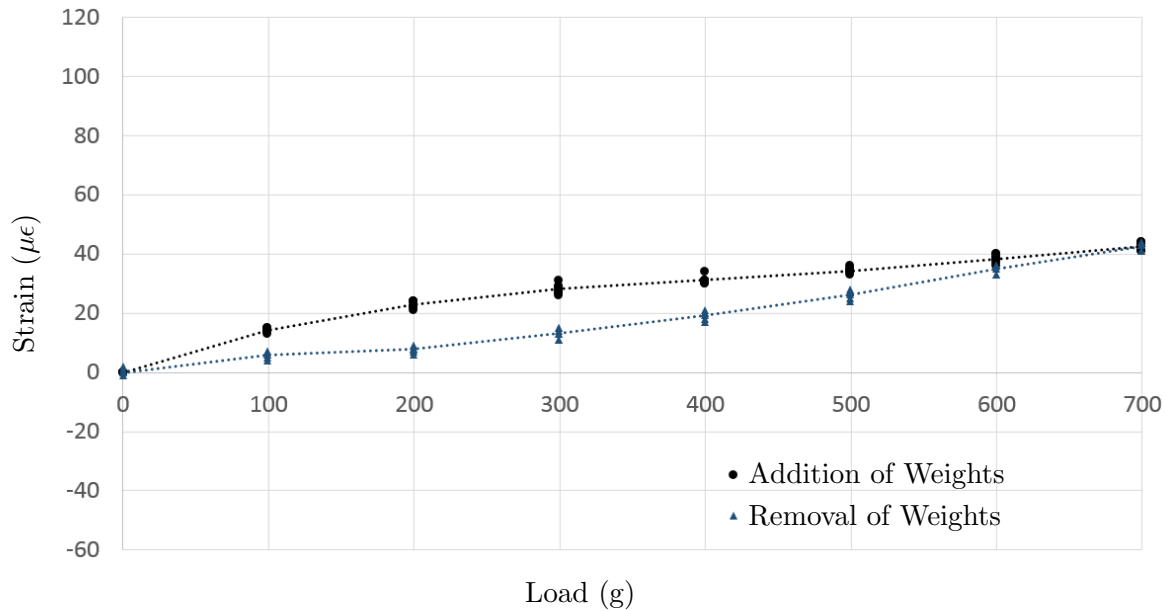


Figure 5.3: Scatter plot of strain at incremental loading conditions for Gauge 1. Average strain is represented by dotted lines.

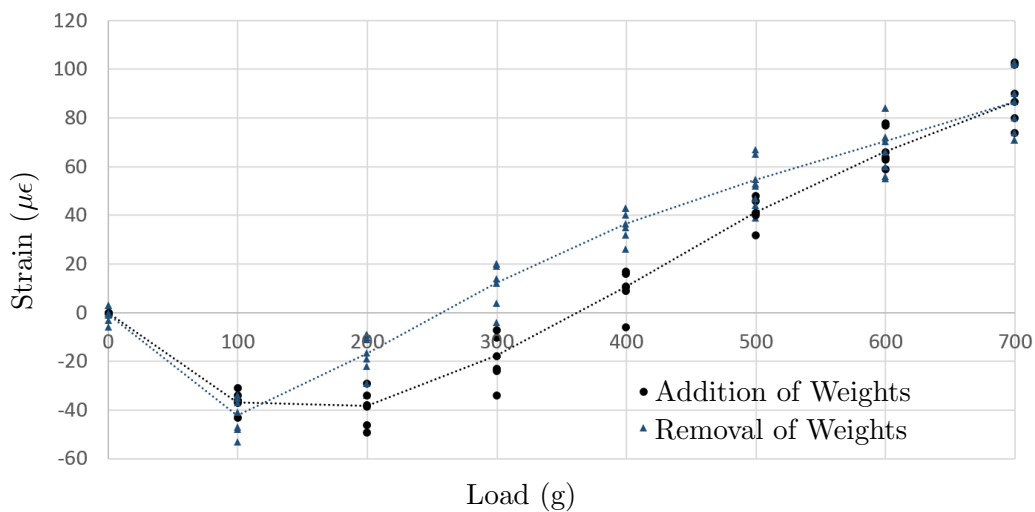


Figure 5.4: Strain reading from P3 at incremental loading conditions for Gauge 2. Average strain is represented by dotted lines.

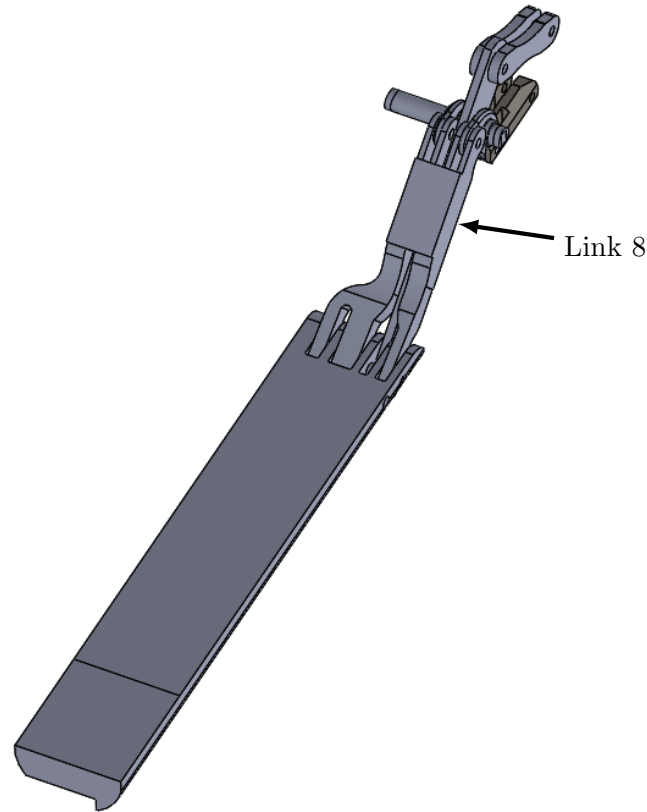


Figure 5.5: Link configuration and asymmetric jaw design.

During tissue palpation, the jaw may also experience side loads while tissue is being manipulated. The ability of the tool to support side loads, and its sensitivity to such loads was investigated by rotating the tool 90 degrees and placing weights on the side of one jaw. Data from this test (Figures 5.6 and 5.7) showed that Gauge 1 was much less sensitive to side loads than Gauge 2, reaching a maximum strain of about $9.00 \mu\epsilon$ with a side load of 400 g. Gauge 2, on the other hand, reached $380 \mu\epsilon$ when the same load was placed on the jaw. Due to high observed strain, the device was not loaded past 400 g. Considering that normal lung tissue weighs about 600 g, side loads may cause a significant error in tool–tissue force estimation of as much as $10 \mu\epsilon$ at Gauge 1 and over $300 \mu\epsilon$ at Gauge 2. Since the actual direction of the load during palpation cannot be easily determined in real time, tool–tissue forces will be measured more accurately by Gauge 1.

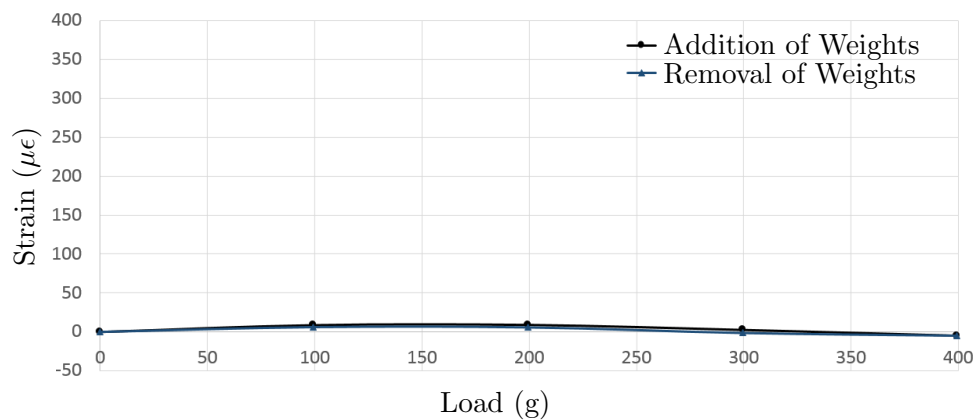


Figure 5.6: Strain readings from Gauge 1 with incremental side loads on the jaw.

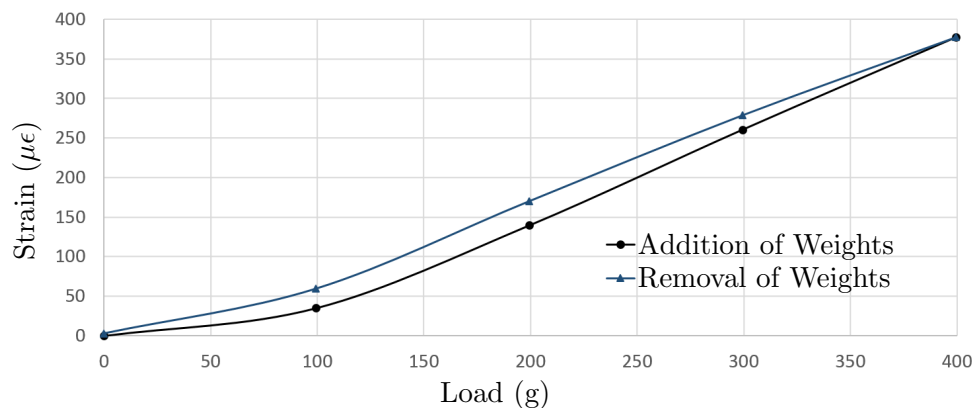


Figure 5.7: Strain readings from Gauge 2 with incremental side loads on the jaw.

5.2.1 FEA Model Validation

Using the experimental data, the FEA conducted in Chapter 3 was validated in order to determine its accuracy. At a maximum load of 700 g, an average strain of $43 \mu\epsilon$ was measured at Gauge 1, while an average strain of $87 \mu\epsilon$ was measured at Gauge 2. In comparison, the strain calculated using FEA at Gauges 1 and 2 were $39 \mu\epsilon$ and $90 \mu\epsilon$ respectively (Figure 5.8). The average measured strain was 10% lower at Gauge 1 and 3% lower at Gauge 2 as compared to the FEA calculations. Unlike the results for the normal loading condition, the side load FEA model overestimated the strain at Gauge 1 by a factor of seven, but under estimated the strain at Gauge 2 by a factor of two (Figure 5.9).

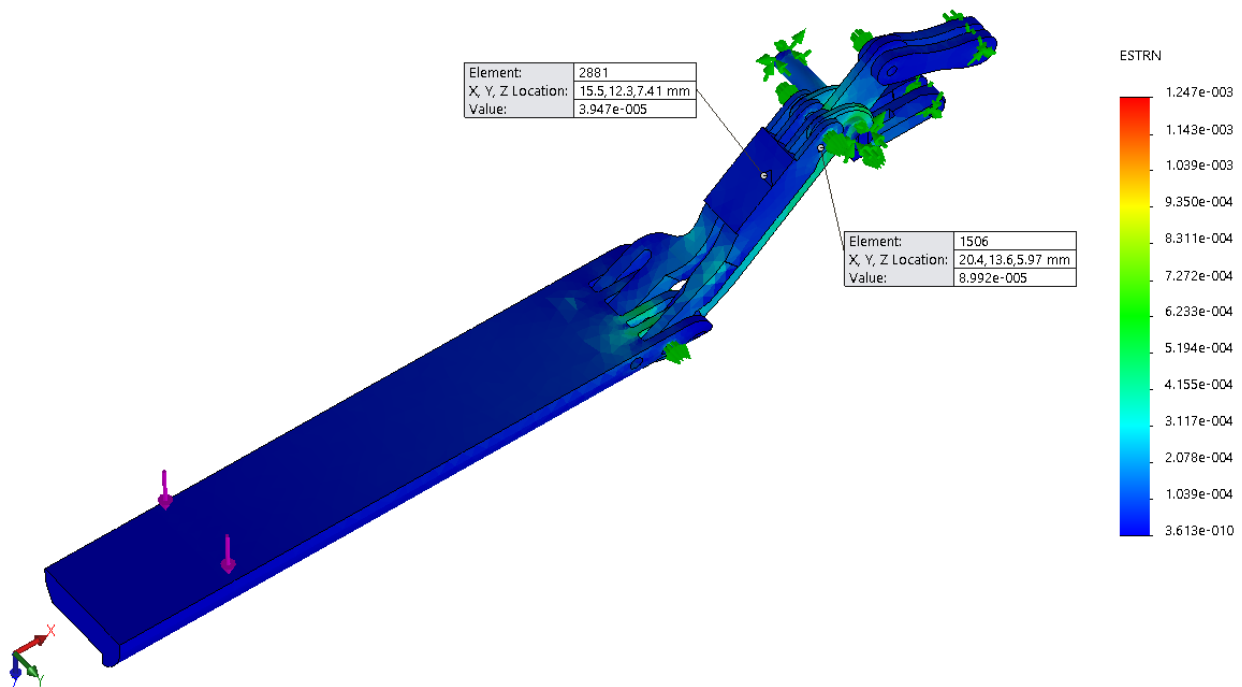


Figure 5.8: FEA strain results from applying a normal load of 7 N.

One possibility for the discrepancy between measured and theoretical strain is improper strain gauge bonding to the link. The small size of the gauges and the links made it challenging to glue the gauge and align it with the central axis of the link. Any misalignment would greatly affect the ability of the gauge to measure strain. Similarly, slight inaccuracies in manufacturing and replication of the simulation setup in real life would also affect the results and may explain the discrepancy between the theoretical and measured strain values.

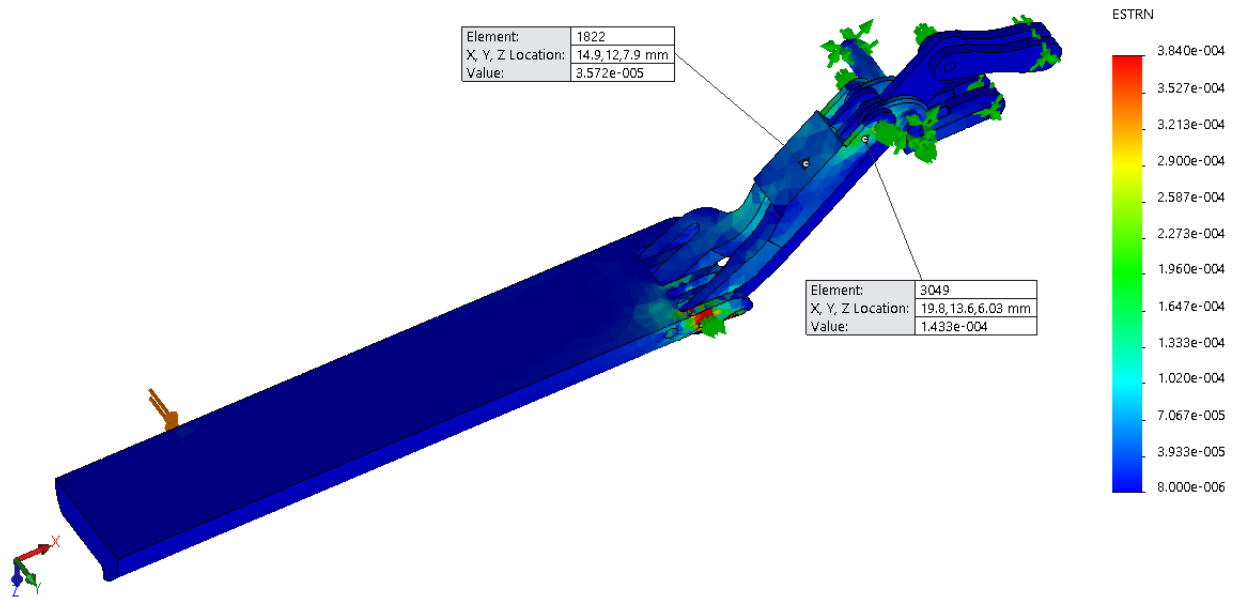


Figure 5.9: FEA strain results from applying a side load of 4 N.

Discretization errors and stress singularities within the FEA model could have also played a role in the observed stress discrepancies. Discretization errors result from representing a continuous variable as a finite number of evaluations on a computer. Although there is always some amount of discretization error in FEA models, it was minimized in the FEA models presented in this thesis by refining mesh size and increasing element order. Mesh refinement was conducted until the percent difference between two consecutively measured stresses was less than 5%. The refinement of mesh size also helped mitigate the effects of stress singularities. A stress singularity prevents a point on the mesh from converging towards a specific value. The stress at the singularity will also influence the stress results near the singularity and will increase their values.

Stress singularities tend to occur on sharp re-entrant corners, corners of two or more bodies in contact and at point restraints, all of which were present in the FEA model of the tool. For these reasons, strain was attempted to be measured away from the edges of Link 8. Saint-Venant's principle allows the dismissal of stress singularities when the stress near the singularity is not of interest [59]. Figure 5.10 shows how the effects of stress singularities can be minimized through mesh refinement by increasing the number of elements that span the surface of the link. With an increased mesh distance between the stress singularity and the point at which strain is sampled, the stress at the point of interest is less influenced by the singularity. In addition, friction between

the links of the real device was not modeled in SolidWorks, and could have also played a role in the strain discrepancy (FEA model setup can be found in Appendix B).

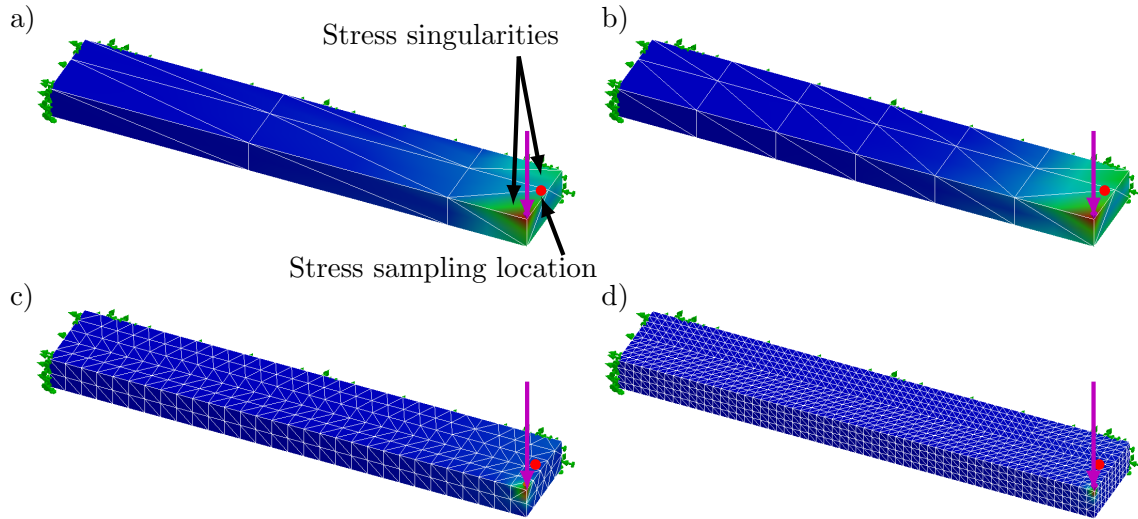


Figure 5.10: A load is applied to a rectangular block at the location and direction of the purple arrow. Mesh size, represented by white lines, is decreased from a) to d). The effects of stress singularities are negligible in mesh d) as compared to the mesh a).

Although some errors exist in the FEA models, the FEA model for a load oriented normal to the jaw is, on average, within 10% of the measured strain from Gauge 1 and Gauge 2. Therefore, the FEA results could be used to show that the jaws can support a normal load of 10 N, with a 10% uncertainty. Destructive testing would need to be completed in order to verify this load capacity. Since a consistent trend between the FEA model and measured strain was not found for side loads, the side load carrying capacity of the Palpatron would need to be determined by loading the jaw until failure. Although there was visible deformation of the tool under a 400 g load, no permanent deformation was observed on any component. It is expected that the tool will be able to support a side load of at least 600 g without material failure.

5.3 Palpation Abilities

The main purpose of the designed tool is for tissue palpation. Therefore, the ability of the tool to palpate to a force of 8 N was tested. A palpation force of 8 N is twice the required force required to properly palpate tissue [50]. The test was conducted by lifting and lowering an 800

g mass (Figure 5.11). The instrument was able to successfully complete the task over ten times. The palpation abilities were further investigated by ensuring that the instrument was able to consistently apply a sufficient grasping force. An 80 mm rubber ball was grasped with a 4 N grasping force (Figure 5.12). Although the rubber ball is much thicker than normal lung tissue, it tested the full capabilities of the Palpatron at applying a 4 N grasping force. Over 20 trials were conducted in which the instrument successfully grasped the ball to the required grasping force.



Figure 5.11: Jaw lifting a 700 g mass.

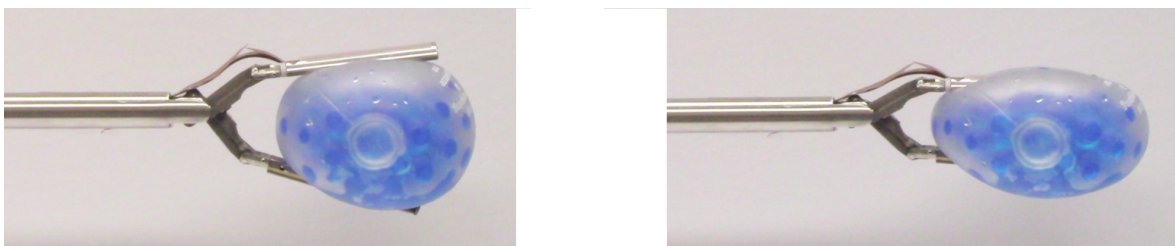


Figure 5.12: Squeezing of a rubber ball to 4 N.

To test the object manipulation capabilities of the tool, a wooden block, angled at 30 degrees, was grasped using the manual control system and placed into a container with a hole matching the contour of the wooden block (Figures 5.13 and 5.14). Strain readings were monitored to ensure that a 4 to 5 N grasping force was applied to the block. The same task was completed with the block in the reverse orientation (Figure 5.15). Five trials were conducted for each block orientation, with the jaws starting at a fully closed position at the beginning of each trial. It was determined that the placement task took 67 seconds on average to complete. The large completion time was mainly due to the slow movement of the jaws. However, the control system proved to be intuitive enough that no extensive training, other than remembering how the joysticks influence jaw movement, was required to accurately place the block into the box.



Figure 5.13: Grasping a wood wedge with a declining slope.



Figure 5.14: Slot and wooden block.



Figure 5.15: Grasping a wood wedge with an inclining slope.

5.4 Conclusions

This chapter presents the experimental setup used to validate the design of the Palpatron. The validation setup involved clamping the instrument to a wooden base and applying a load onto one jaw using a hooked weight rack. It was determined that the designed tool can support a load of 8 N, which matches the average weight of an adult lung of 800 g [53]. While weights were placed on the jaw, a P3 Strain Indicator and Recorder was used to obtain strain readings from two locations on one link. A linear relationship between load and strain was observed, facilitating the estimation of tool–tissue forces. It was determined that of the two strain gauges placed on one of the links, the gauge that was more in line with the centre-axis of the jaw was more accurate.

Strain readings were used to validate the FEA model developed in Chapter 3. Through validation of the simulation results, it was determined that the tool would be able to support a normal load of 10 N. However, the ability of the tool to support a side load of 10 N was not confirmed. A side load of 4 N is the highest that was tested. The simulation results for side loads did not reflect the measured values well enough to provide any meaningful correlation between the measured and calculated values.

Furthermore, the ability of the tool to maneuver objects with a grasping force of 4 N was tested. The manual control system proved to be intuitive and sufficiently accurate to perform simple object maneuvering tasks. With improved control algorithms, grasping speeds can be greatly increased, making tool use more comparable to the direct manipulation of objects with a hand. Having completed some preliminary tests, the ability of the designed tool to meet the design targets can be evaluated. Table 5.1 shows a comparison between tool performance and the design targets generated in Chapter 3. The Palpatron has met or exceeded the majority of the design targets. The only outstanding design targets are: load carrying capacity, movement resolution and weight. With further testing, the load carrying capacity can be verified through destructive testing. On the other hand, movement resolution can only be improved by redesigning the linkage mechanism or by using an encoder with a finer resolution. Although the current movement resolution is much higher than the desired value, it did not pose a problem for manual control of the jaws.

Table 5.1: A comparison of tool performance to design targets.

Design Specifications	Design Target	Actual Value
Nominal load capacity	10 N	8 N
Nominal palpation force	5 N	8 N
Nominal speed	1–2 °/s	1 °/s
Movement resolution	$\leq 0.01^\circ$	0.84 °
Diameter of handle	≤ 65 mm	50.8 mm
Length of handle	80–90 mm	83 mm
Widest jaw opening	≥ 40 mm	128 mm fully extended, 35 mm parallel jaws
DOF for each jaw	3	3
Trocar size	12 mm	12 mm
Tool length	300–400 mm	380 mm
Tool weight	600–800 g	1200 g

Chapter 6

Conclusions and Recommendations

6.1 Summary

The work presented in this thesis describes the design and manufacturing of the Palpatron, a novel hand-held minimally-invasive tumour localization device. The Palpatron surpasses the performance of current minimally-invasive devices, and brings palpation technology a step further towards a palpation device that is as effective and efficient as a bare hand at localizing tumours. The proposed device incorporates one ultrasound jaw and one tactile jaw that are independently actuated, allowing for optimal jaw–sensor alignment. The instrument also allows the jaws to be easily sterilized and tool–tissue forces to be measured.

In order to validate the design, a prototype was fabricated to test the mechanical capabilities and manual control system of the Palpatron. It was determined that the proposed device could be used under the designed 10 N load, while achieving a factor of safety of 1.2. The device was also able to manipulate and move loads of 8 N using a manual control system involving two joysticks and four motors. Due to the cost and uniqueness of the design, validation experiments were not conducted to failure. Based on the observed capabilities of the Palpatron, the device provides a substantial advancement to current minimally-invasive instruments. With continued development, the proposed system will be able to provide a compact and minimally-invasive means for tumour localization that can mimic manual palpation and present intra-operative images. Such system will greatly enhance delivery of therapy.

6.2 Concluding remarks

The Palpatron has a great potential to improve minimally-invasive lung tumour localization. Though the motivation for the presented work was lung cancer treatment, the Palpatron can also be used on other organs, such as the liver. The device incorporates one imaging sensor, one tactile sensor and two strain gauges. The ultrasound sensor can be used to examine the subsurface of tissue while the tactile sensor can be used to create a topographical map of tissue texture. The strain gauges can be used to provide kinaesthetic feedback. By combining these data sets, a 3D model of the subsurface tissue can be created while ensuring that correct palpation forces are being applied to the tissue. The 3D model of tissue in combination with kinaesthetic feedback will allow for optimal imaging data collection and reduction in tissue damage.

In traditional grasper-based, minimally-invasive palpating designs, jaw motion is coupled. This severely limited palpation capabilities as the jaws could only undergo mirrored motion. The added flexibility of uncoupled jaw motion in the presented design allows for better tool dexterity, ensuring that different thicknesses of tissue with many different inclines can be palpated. Uncoupled jaw motion also allows for fast jaw alignment with tissue as it is possible for one jaw to remain stationary while the other moves to align with the surface of the tissue. Improved jaw-tissue alignment provides better imaging results. Since the Palpatron is electronically controlled, it can also be incorporated into robotic surgical systems by implementing an automated control system with the existing motor controllers. An automated system will allow for repeatable palpation actions, which are expected to increase tumour localization performance.

The Palpatron is unique from other lung tumour localization tools in the following ways:

1. Improved tissue manipulation abilities and sensor alignment with tissue.
2. Lower risk of tissue damage due to the incorporation of kinaesthetic feedback.
3. Easy tool assembly and disassembly allowing for sterilization of jaws.

6.3 Recommendations

Due to mainly focusing on design, the time spent analyzing the performance of the Palpatron and determining its capabilities was very limited. Although some experimental validation was completed, extensive testing, iterations and improvements are still required in order for the device to reach its full potential. The next sections present some potential future improvements and tests that can be conducted on the instrument.

6.3.1 Mechanical Design

One of the biggest problems in the current mechanical design is stress amplification. Loads applied to the jaws are amplified ten fold at the push rods. A lower amplification will allow for a higher tool factor of safety without the need of acquiring very strong materials. The jaws were previously designed based on commercial products used for tissue manipulation. The problem with the jaws is their length and attachment location to the rest of the instrument that created a large force amplification that weakened the overall tool design. Reducing the force amplification by reassessing the geometry of the current links and the jaws would help improve the factor of safety and side load carrying capacity of the Palpatron.

Aside from improving the links and jaws, the use of cables for link actuation can be considered instead of push rods. Using cables as an alternative may help to achieve a stronger and more compact design. In addition, it could allow for the the implementation of wrist joints that could potentially improve tumour localization by increasing the number of spatial configurations available for the jaws. However, the challenges that accompany the inclusion of wrist joints need to be kept in mind, as discussed in Chapter 3.3.1.

Furthermore, the current design uses a sleeve that slides over the jaws to support the main shaft. The sleeve has a very tight clearance with some of the wires that connect to sensors on the jaws. A better method should be implemented to prevent accidental wire damage. Similarly, the strain relief mechanism for wires coming out of the back of the handle did not work properly. Not enough clearance was provided for all the wires to pass through the back of the instrument. A mechanism with a larger space for wires is required to prevent the wires from detaching from

motors and other electrical components of the tool.

Lastly, backlash in the system can be greatly minimized by replacing plastic components with metal ones, as described in Chapter 4.1.3. Optical encoders or other sensors can also be implemented to estimate backlash in real time.

6.3.2 Control System

The current control system provides the user with manual control capabilities. The next step would be to implement automatic controls which can allow for automatic tissue palpation and integration with robotic systems. However, in the current tool design, correct jaw alignment cannot be easily determined solely by relying on jaw sensors. Therefore, a method for determining proper jaw contact with tissue needs to be implemented. This can be achieved by placing additional sensors at the tip and base of the jaw which are able to sense whether the entire jaw is in contact with tissue.

In order to further improve tool control and efficiency, haptic and visual feedback need to be implemented. Haptic feedback requires a control system that can interact with the surgeon. In this case, the existence of a tumour or changes in tissue stiffness are relayed to the hand of the user. Implementation could include a redesigned handle that is able to provide motion resistance to the hand of the operator. Similarly, tool-tissue forces can be displayed on a screen, but this would require more strain gauges can be placed on the instrument to better estimate tool-tissue forces. For example, gauges can be placed on push rods and the handle in addition to the links. The present locations for gauges on one link have shown to be sensitive to load orientation, affecting their reliability. Therefore, in order to make the force estimation more accurate, additional room on the links needs to be made to allow for the placement of additional sensors. Strain gauges need to first be calibrated by placing weights on the jaw, and then validated using a load cell or similar apparatus to ensure accurate measurement of applied loads.

6.3.3 Testing and Validation

In order to test the performance of the Palpatron in real-time tumour localization, the tool needs to be tested on phantom tissue that is embedded with fake tumours. It is also recommended to

verify the load carrying capacity of the tool. The tool needs to be loaded to the designed 10 N to verify its functionality. A test setup needs to be designed in which varying loads along a single jaw and both jaws can be applied, in varying directions, for varying end-effector configurations. Once tool reliability and efficiency are determined, the instrument should be tested on *ex vivo* lung tissue in order to compare its performance to currently available tumour localization devices.

Once the performance of the design is tested, the ease of use and effectiveness of the current design can be determined. This can be accomplished by conducting palpation experiments on tissue with embedded phantom tumours, involving multiple instrument operators with varying levels of expertise. Ease of use and effectiveness can be judged by the sensitivity and specificity of the device at localizing a tumour, and the ability of the operator to use the device.

References

- [1] Government of Canada, “Predictions of the future burden of cancer in Canada,” May 2015. [Online]. Available: <http://www.cancer.ca/~media/cancer.ca/CW/cancer%20information/cancer%20101/Canadian%20cancer%20statistics/Canadian-Cancer-Statistics-2015-EN.pdf?la=en>
- [2] R. Martinez-Monge, I. Vivas, C. Garran, and J. M. Lopez-Picazo, “Percutaneous CT-guided 103pd implantation for the medically inoperable patient with T1N0M0 non-small cell lung cancer: A case report.” *Brachytherapy*, vol. 3, no. 3, pp. 179–181, Aug 2004.
- [3] R. Harris, B. Croce, and T. D. Yan, “Minimally invasive pulmonary resection,” *Annals of Cardiothoracic Surgery*, vol. 1, no. 1, 2012. [Online]. Available: <http://www.annalscts.com/article/view/488>
- [4] H. van Overhagen, K. Brakel, M. W. Heijenbrok, J. H. L. M. van Kasteren, C. N. F. van de Moosdijk, A. C. Roldaan, A. P. van Gils, and B. E. Hansen, “Metastases in supraclavicular lymph nodes in lung cancer: assessment with palpation, US, and CT,” *Radiology*, vol. 232, no. 1, pp. 75–80, 2004.
- [5] C. J. Simon, D. E. Dupuy, T. A. DiPetrillo, H. P. Safran, C. A. Grieco, T. Ng, and W. W. Mayo-Smith, “Pulmonary radiofrequency ablation: long-term safety and efficacy in 153 patients,” *Radiology*, vol. 243, no. 1, pp. 268–275, 2007.
- [6] USC Cardiothoracic Surgery, “A patient’s guide to lung surgery: The thoracotomy procedure,” 2015. [Online]. Available: <http://www.cts.usc.edu/lpg-thoracotomy-thethoracotomyprocedure.html>
- [7] Continuing Professional Development, “Minimally invasive gynaecologic surgery,” Sept 2015. [Online]. Available: <http://www.cpd.utoronto.ca/migs/>
- [8] S. Schostek, M. O. Schurr, and G. F. Buess, “Review on aspects of artificial tactile feedback in laparoscopic surgery,” *Medical Engineering and Physics*, vol. 31, no. 8, pp. 887–898, 2009.
- [9] C. R. Wagner, N. Stylopoulos, and R. D. Howe, “The role of force feedback in surgery: Analysis of blunt dissection,” in *International Symposium on Haptic Interfaces for Virtual Environment and Teleoperator Systems*, Orlando, FL, 2002, p. 73.
- [10] T. P. Kurowski, A. L. Trejos, M. D. Naish, R. Patel, and R. A. Malthaner, “Design of a minimally invasive lung tumor localization device,” in *ASME 5th Annual Dynamic Systems and Control Conference*, vol. 3, Fort Lauderdale, FL, 2012, pp. 411–418.

- [11] A. Bicchi, G. Canepa, P. I. De Rossi, and E. Scillingo, "A sensor-based minimally invasive surgery tool for detecting tissue elastic properties," in *IEEE International Conference on Robotics and Automation*, vol. 1, Minneapolis, MN, 1996, pp. 884–888.
- [12] P. Berkelman, "A compact, simple, and robust teleoperated robotic surgery system," in *Surgical Robotics: Systems Applications and Visions*. Boston, MA: Springer US, 2011, ch. 7, pp. 139–158.
- [13] G. L. McCreery, A. L. Trejos, R. V. Patel, M. D. Naish, and R. A. Malthaner, "Evaluation of force feedback requirements for minimally invasive lung tumour localization," in *IEEE/RSJ International Conference on Intelligent Robots and Systems*, San Diego, CA, 2007, pp. 883–888.
- [14] A. M. Okamura, "Force feedback and sensory substitution for robot-assisted surgery," in *Surgical Robotics: Systems Applications and Visions*. Boston, MA: Springer US, 2011, ch. 18, pp. 419–448.
- [15] J. Rosen, B. Hannaford, M. P. MacFarlane, and M. N. Sinanan, "Force controlled and teleoperated endoscopic grasper for minimally invasive surgery-experimental performance evaluation," *IEEE Transactions on Biomedical Engineering*, vol. 46, no. 10, pp. 1212–1221, 1999.
- [16] M. MacFarlane, J. Rosen, B. Hannaford, C. Pellegrini, and M. Sinanan, "Force-feedback grasper helps restore sense of touch in minimally invasive surgery," *Journal of Gastrointestinal Surgery*, vol. 3, no. 3, pp. 278–285, 1999.
- [17] J. Rosen, J. Brown, S. De, and B. Hannaford, "Macro and micro soft-tissue biomechanics and tissue damage: Application in surgical robotics," in *Surgical Robotics: Systems Applications and Visions*. Boston, MA: Springer US, 2011, ch. 24, pp. 583–618.
- [18] J. Dargahi and S. Najarian, "An integrated force-position tactile sensor for improving diagnostic and therapeutic endoscopic surgery," *Bio-medical Materials and Engineering*, vol. 14, no. 2, pp. 151–166, 2004.
- [19] G. Tholey, A. Pillarisetti, W. Green, and J. P. Desai, "Design, development, and testing of an automated laparoscopic grasper with 3-D force measurement capability," *Medical Simulation*, vol. 3078, no. 2, pp. 38–48, 2004.
- [20] P. L. Yen, "Palpation sensitivity analysis of exploring hard objects under soft tissue," in *IEEE/ASME International Conference on Advanced Intelligent Mechatronics*, vol. 2, Kobe, Japan, 2003, pp. 1102–1106.
- [21] M. D. Naish, R. V. Patel, A. L. Trejos, M. T. Perri, and R. A. Malthaner, "Robotic techniques for minimally invasive tumor localization," in *Surgical Robotics: Systems Applications and Visions*. Boston, MA: Springer US, 2011, ch. 20, pp. 469–496.
- [22] D. T. V. Pawluk, J. S. Son, P. S. Wellman, W. J. Peine, and R. D. Howe, "A distributed pressure sensor for biomechanical measurements," *Journal of Biomechanical Engineering*, vol. 120, no. 2, pp. 302–305, 1998.
- [23] M. E. H. Eltaib and J. R. Hewit, "Tactile sensing technology for minimal access surgery—a review," *Mechatronics*, vol. 13, no. 10, pp. 1163–1177, 2003.

- [24] N. Kattavenos, B. Lawrenson, T. G. Frank, M. S. Pridham, R. P. Keatch, and A. Cuschieri, "Force-sensitive tactile sensor for minimal access surgery," *Minimally Invasive Therapy and Allied Technologies*, vol. 13, no. 1, pp. 42–46, 2004.
- [25] J. Dargahi, S. Najarian, and K. Najarian, "Development and three-dimensional modelling of a biological-tissue grasper tool equipped with a tactile sensor," *Canadian Journal of Electrical and Computer Engineering*, vol. 30, no. 4, pp. 225–230, 2005.
- [26] R. Sedaghati, J. Dargahi, and H. Singh, "Design and modeling of an endoscopic piezoelectric tactile sensor," *International Journal of Solids and Structures*, vol. 42, no. 21, pp. 5872–5886, 2005.
- [27] S. Schostek, C.-N. Ho, D. Kalanovic, and M. O. Schurr, "Artificial tactile sensing in minimally invasive surgery: a new technical approach," *Minimally Invasive Therapy and Allied Technologies*, vol. 15, no. 5, pp. 296–304, 2006.
- [28] H. Roham, S. Najarian, S. Mohsen Hosseini, and J. Dargahi, "Design and fabrication of a new tactile probe for measuring the modulus of elasticity of soft tissues," *Sensor Review*, vol. 27, no. 4, pp. 317–323, 2007.
- [29] A. Mirbagheri and F. Farahmand, "Design and analysis of an actuated endoscopic grasper for manipulation of large body organs," in *Annual International Conference of the IEEE Engineering in Medicine and Biology Society*, Buenos Aires, Argentina, Sept 4 2010, pp. 1230–1233.
- [30] IMS, "Laparoscopic babcock grasper 330 mm 10 mm," December 2013. [Online]. Available: <http://www.spectrumsurgical.com/product/70-2010G/Laparoscopic-Babcock-Grasper-330mm-10mm.php>
- [31] H. Seibold, B. Kuebler, H. Weiss, T. Otmaier, and G. Hirzinger, "Sensorized and actuated instrument for minimally invasive robotic surgery," in *EuroHaptics*, Munich, Germany, 2004, pp. 482–485.
- [32] F. Meer, A. Giraud, D. Esteve, and X. Dollat, "A disposable plastic compact wrist for smart minimally invasive surgical tools," in *IEEE/RSJ International Conference on Intelligent Robots and Systems*, Edmonton, Alberta, 2004, pp. 919–924.
- [33] S. M. Hosseini, S. Najarian, S. Motaghinas, A. T. Golpaygani, and S. Torabi, "Prediction of tumor existence in the virtual soft tissue by using tactile tumor detector," *American Journal of Applied Sciences*, vol. 5, no. 5, pp. 483–489, 2008.
- [34] K. Takashima, K. Yoshinaka, T. Okazaki, and K. Ikeuchi, "An endoscopic tactile sensor for low invasive surgery," *Sensors and Actuators: A. Physical*, vol. 119, no. 2, pp. 372–383, 2005.
- [35] M. T. Perri, A. L. Trejos, M. D. Naish, R. V. Patel, and R. A. Malthaner, "New tactile sensing system for minimally invasive surgical tumour localization," *The International Journal of Medical Robotics and Computer Assisted Surgery*, vol. 6, no. 2, pp. 211–220, 2010.
- [36] A. P. Miller, W. J. Peine, J. S. Son, and Z. T. Hammoud, "Tactile imaging system for localizing lung nodules during video assisted thoracoscopic surgery," in *IEEE International Conference on Robotics and Automation*, Rome, Italy, 2007, pp. 2996–3001.

- [37] K. Baba, "Endoscope having an ultrasonic diagnosis function," US Patent 4 401 123, Aug 30, 1983.
- [38] M. A. Cundari, A. I. West, T. W. Roberts, and D. R. Widder, "Diagnosis and treatment of tissue with instruments," US Patent 6 063 031, May 16, 2000.
- [39] A. West, J. Weinstein, N. Dewagan, and D. Krag, "Obtaining images of structures in bodily tissue using ultrasound and pressure-sensing," WO Patent 2001/039 668 A1, June 07, 2001.
- [40] W. J. Hyung, J. S. Lim, J. H. Cheong, Y. C. Lee, and S. H. Noh, "Tumor localization using laparoscopic ultrasound for a small submucosal tumor," *Journal of Surgical Oncology*, vol. 86, no. 3, pp. 164–165, 2004.
- [41] T. P. Kurowski, "Design of a hand held minimally invasive lung tumour localization device," Master's thesis, Department of Mechanical and Materials Engineering, Western University, London, ON, 2011.
- [42] A. Escoto, S. Bhattad, A. Shamsil, A. Sanches, A. L. Trejos, M. D. Naish, R. A. Malthaner, and R. V. Patel, "A multi-sensory mechatronic device for localizing tumors in minimally invasive interventions," in *IEEE International Conference on Robotics and Automation*, Seattle, WA, 2015, pp. 4742–4747.
- [43] M. N. Leroy, "Design of a minimally invasive single port HDR brachytherapy applicator for the treatment of lung cancer," Master's thesis, Department of Mechanical and Materials Engineering, Western University, London, ON, 2013.
- [44] M. O. Culjat, J. W. Bisley, C.-H. King, C. Wottawa, R. E. Fan, E. P. Dutson, and W. S. Grundfest, "Tactile feedback in surgical robotics," in *Surgical Robotics: Systems Applications and Visions*. Boston, MA: Springer US, 2011, ch. 19, pp. 449–468.
- [45] C. R. Doarn and G. R. Moses, "Overcoming barriers to wider adoption of mobile telerobotic surgery: Engineering, clinical and business challenges," in *Surgical Robotics: Systems Applications and Visions*. Boston, MA: Springer US, 2011, ch. 4, pp. 69–102.
- [46] T. Hu, A. E. Castellanos, G. Tholey, and J. P. Desai, "Real-time haptic feedback in laparoscopic tools for use in gastro-intestinal surgery," in *Medical Image Computing and Computer Assisted Intervention*, London, UK, 1996, pp. 66–74.
- [47] R. L. Feller, C. K. L. Lau, C. R. Wagner, D. P. Perrin, and R. D. Howe, "The effect of force feedback on remote palpation," in *IEEE International Conference on Robotics and Automation*, vol. 1, New Orleans, LA, 2004, pp. 782–788.
- [48] M. V. Ottermo, O. Stavadahl, and T. A. Johansen, "Palpation instrument for augmented minimally invasive surgery," in *IEEE/RSJ International Conference on Intelligent Robots and Systems*, vol. 4, Sendai, Japan, 2004, pp. 3960–3964.
- [49] H. Liu, D. P. Noonan, K. Althoefer, and L. D. Seneviratne, "Rolling mechanical imaging: A novel approach for soft tissue modelling and identification during minimally invasive surgery," in *IEEE International Conference on Robotics and Automation*, Pasadena, CA, 2008, pp. 845–850.

- [50] A. L. Trejos, J. Jayender, M. T. Perri, M. D. Naish, R. V. Patel, and R. A. Malthaner, "Robot-assisted tactile sensing for minimally invasive tumor localization," *The International Journal of Robotics Research*, vol. 28, no. 9, pp. 1118–1133, 2009.
- [51] M. M. Dalvand, B. Shirinzadeh, S. Nahavandi, F. Karimirad, and J. Smith, "Force measurement capability for robotic assisted minimally invasive surgery systems," *Lecture Notes in Engineering and Computer Science*, vol. 2207, no. 1, pp. 419–424, 2013.
- [52] A. Naidu, "Design of novel sensors and instruments for minimally invasive lung tumour localization via palpation," Master's thesis, Department of Electrical and Computer Engineering, Western University, London, ON, 2015.
- [53] D. K. Molina and V. J. M. DiMaio, "Normal organ weights in men: part II—the brain, lungs, liver, spleen, and kidneys," *The American journal of forensic medicine and pathology*, vol. 33, no. 4, p. 368, 2012.
- [54] U.S. Department of Health and Human Services, "Anthropometric reference data for children and adults: United states, 2007–2010," October 2012. [Online]. Available: http://www.cdc.gov/nchs/data/series/sr_11/sr11_252.pdf
- [55] M. A. Minor and R. Mukherjee, "Dexterous articulated linkage for surgical applications," US Patent 6 309 403, Oct 30, 2001.
- [56] H. Yamashita, N. Hata, M. Hashizume, and T. Dohi, "Handheld laparoscopic forceps manipulator using multi-slider linkage mechanisms," *Lecture Notes in Computer Science*, vol. 3217, no. 1, pp. 121–128, 2004.
- [57] C. Oldani and A. Dominguez, "Titanium as a biomaterial for implants," in *Recent Advances in Arthroplasty*. Boston, MA: InTech, 2012, ch. 9, pp. 150–153. [Online]. Available: <http://www.intechopen.com/books/recent-advances-in-arthroplasty/titanium-as-a-biomaterial-for-implants>
- [58] I. Mutlu and E. Oktay, "Biocompatibility of 17-4 pH stainless steel foam for implant applications," *Bio-medical materials and engineering*, vol. 21, no. 4, p. 223, 2011.
- [59] P. S. Steif, "Notes on elasticity and finite element analysis," 2005. [Online]. Available: <https://engineering-education.com/miniFEA/notes.pdf>

Appendix A

Diassembly Instructions

This appendix presents instructions for disassembling the Palpatron:

Step 1: With the tool in operation mode (Figure A.1), move the jaws to the fully closed position (Figure A.2).



Figure A.1: Tool in operation mode.

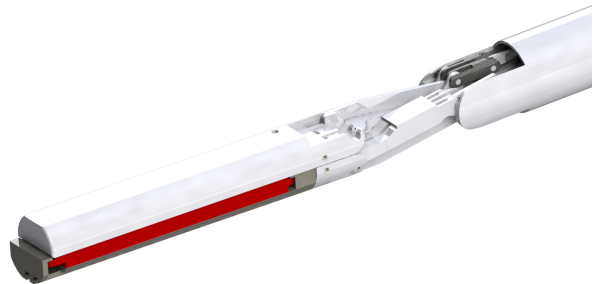


Figure A.2: Tool with jaws closed.

Step 2: Remove the set screws holding the jaws in place to later allow the sleeve to slide past the screw location (Figure A.3).

Step 3: Remove the sleeve retainer, allowing the sleeve to be rotated (Figure A.4).

Step 4: Rotate the sleeve clockwise, when looking from the end effector down towards the handle (Figure A.5).

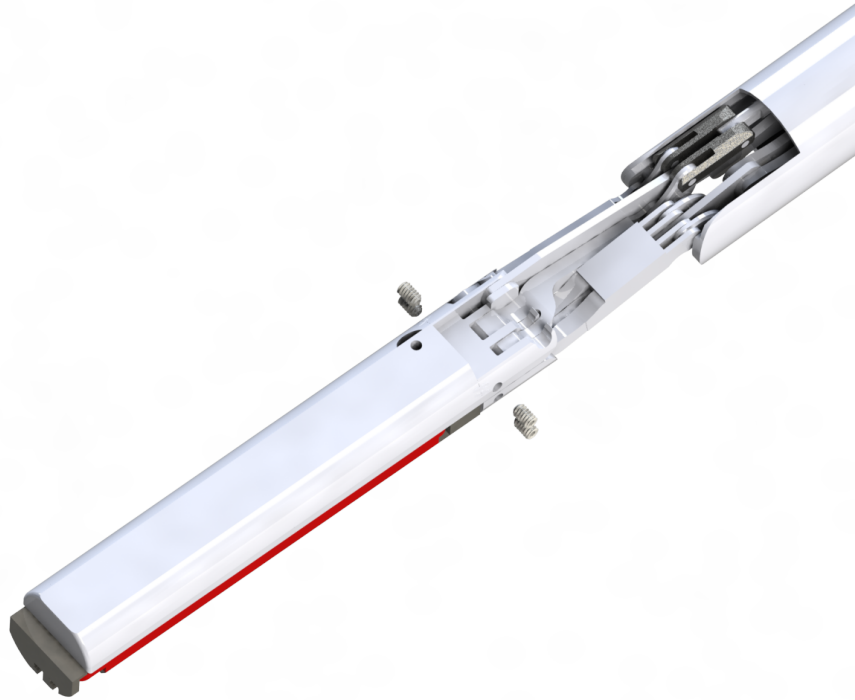


Figure A.3: Removal of set screws located at distal end of tool.



Figure A.4: Removal of sleeve retainer.

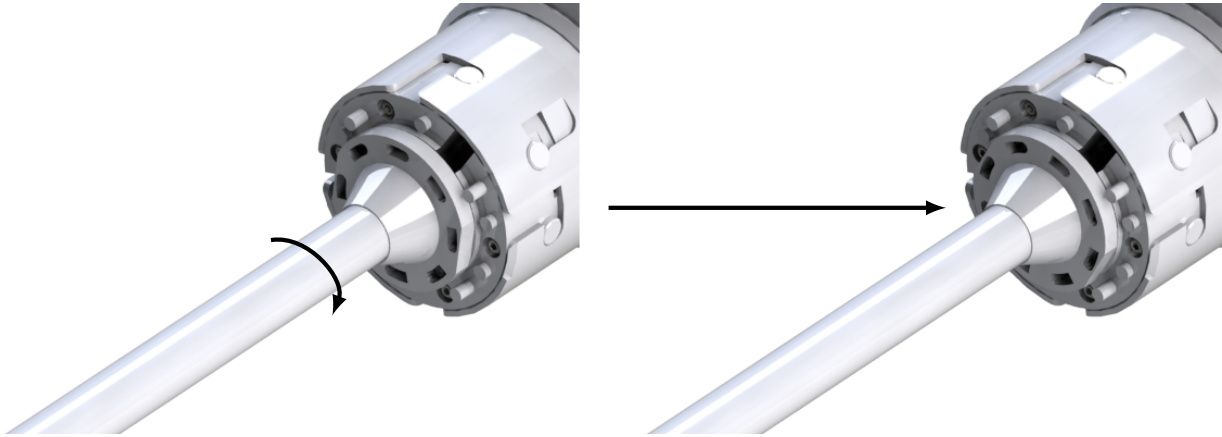


Figure A.5: Rotation of sleeve.

Step 5: Pull the sleeve out slightly and then rotate it approximately 90 degrees so that it covers any exposed wires (Figures A.6 and A.7).

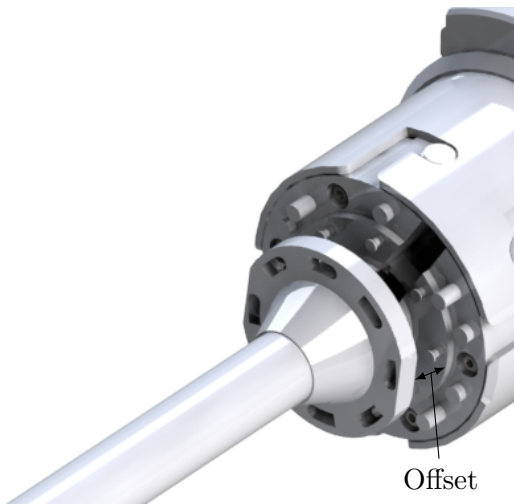


Figure A.6: Sleeve at a slight offset.

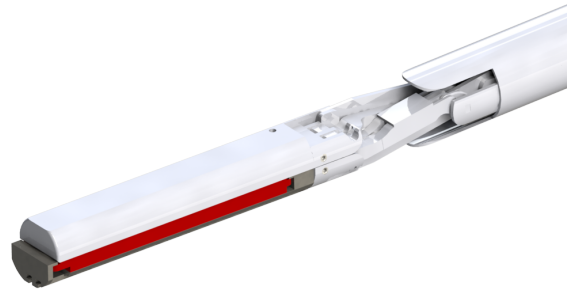


Figure A.7: Sleeve rotated so that wires are covered.

Step 6: Remove the sleeve to expose the internal shaft of the instrument (Figure A.8).

Step 7: Remove the top part of the internal shaft (Figure A.9).

Step 8: Remove the keyway covers by sliding them off of their retaining pins (Figures A.10).

Step 9: Remove the keys from the keyways (Figure A.11).

Step 10: Disconnect the distal end of the tool from the rest of the instrument.



Figure A.8: Removal of sleeve.



Figure A.9: Top cover is removed to allow removal of keyways.



Figure A.10: Keyway covers removed by sliding.

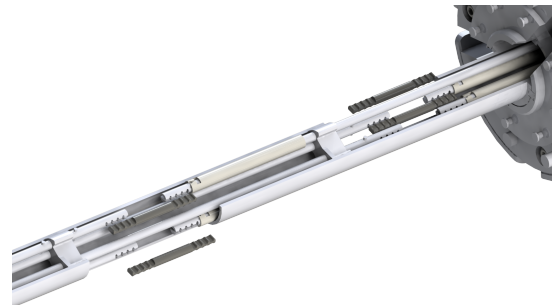


Figure A.11: Removal of keys.

Step 11: Four pieces are left from disassembly (Figures A.12).



Figure A.12: Disassembled device.

Appendix B

Finite Element Model Setup

B.1 Linkage FEA Model

The finite element analysis was conducted using a static SolidWorks simulation analysis. The geometry of the finite element model was constructed based on the configuration of the jaw during the testing phase of the project. The angle between the jaw and Link 8 was measured in the experimental setup and then implemented in the CAD model. To simplify the model, only one jaw with its links were used. A load of 7 N was applied in either a lateral (Figure B.1) or normal (Figure B.2) direction, at 12 mm from the tip of the jaw. This location corresponded to where weights were placed during testing. A global no penetration component contact, with no friction, was established between all of the parts. Such a constraint prevents all surfaces from intersecting one another while allowing the surfaces to freely slide on top of each other or separate. The main support pin was constrained at the locations where it is press fit into the base shaft of the Palpatron (Figure B.3). All rotational and translational degrees of freedom were constrained for the pin. On the other hand, the push rod links were only constrained in translational degrees of freedom and could still rotate at the connection with the push rods (Figure B.4). Finally, pins holding the links together were constrained to prevent them from sliding past the links (Figure B.5). The material used to model the links was Ti-6Al-2Sn-2Zr-2Mo-2Cr-0.25Si, which had the closest material properties to Grade 5 titanium.

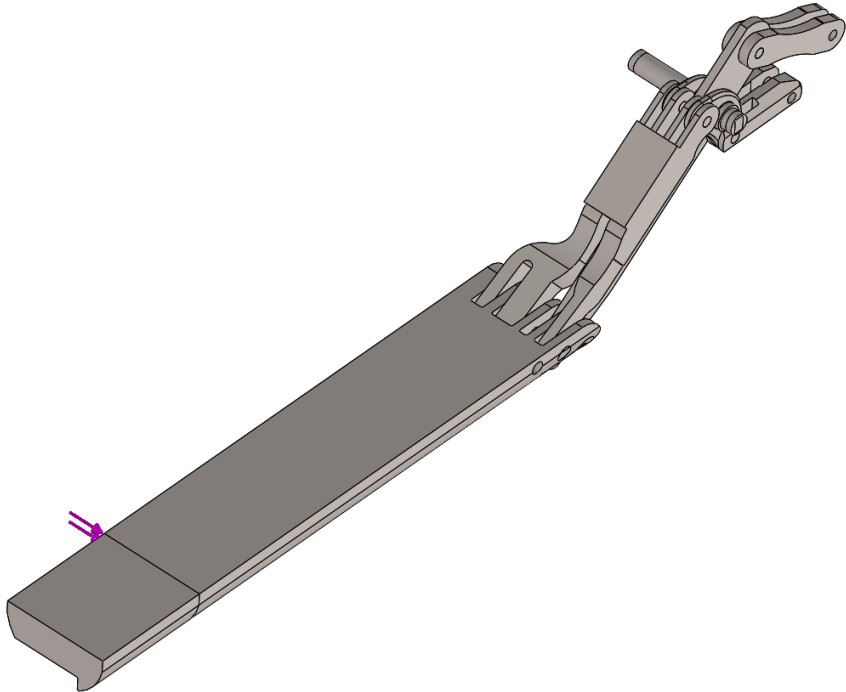


Figure B.1: Lateral load applied to jaw.

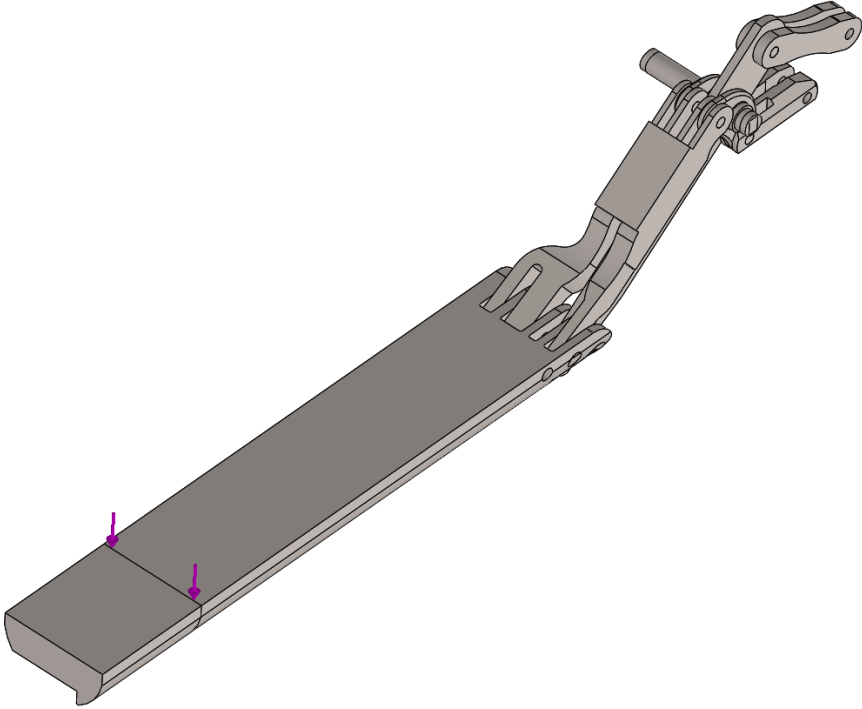


Figure B.2: Normal load applied to jaw.

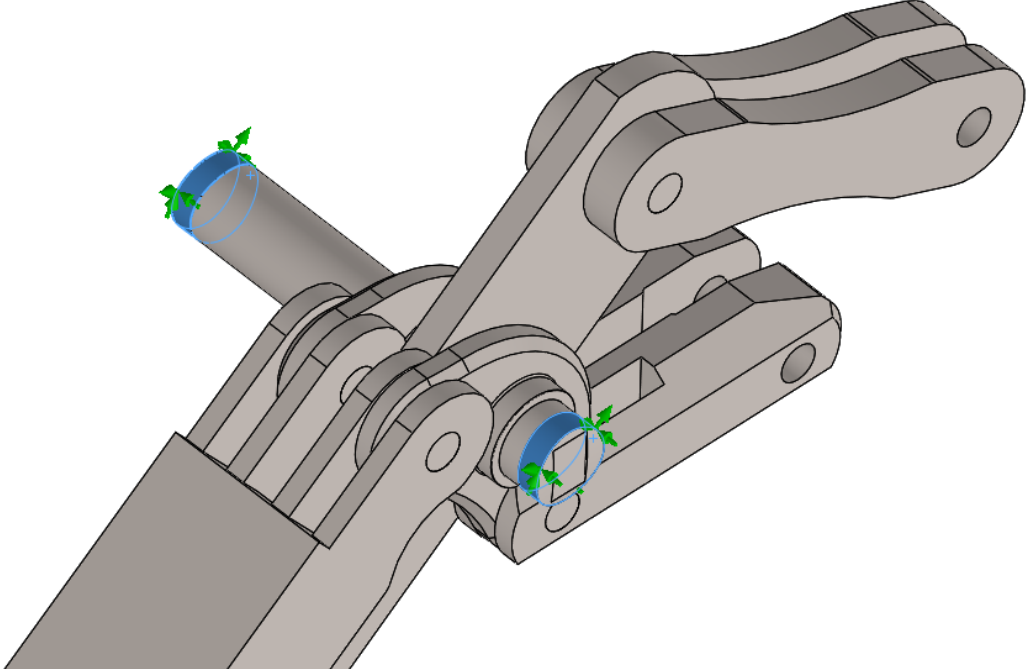


Figure B.3: Main pin constraints. Constrained areas are highlighted in blue.

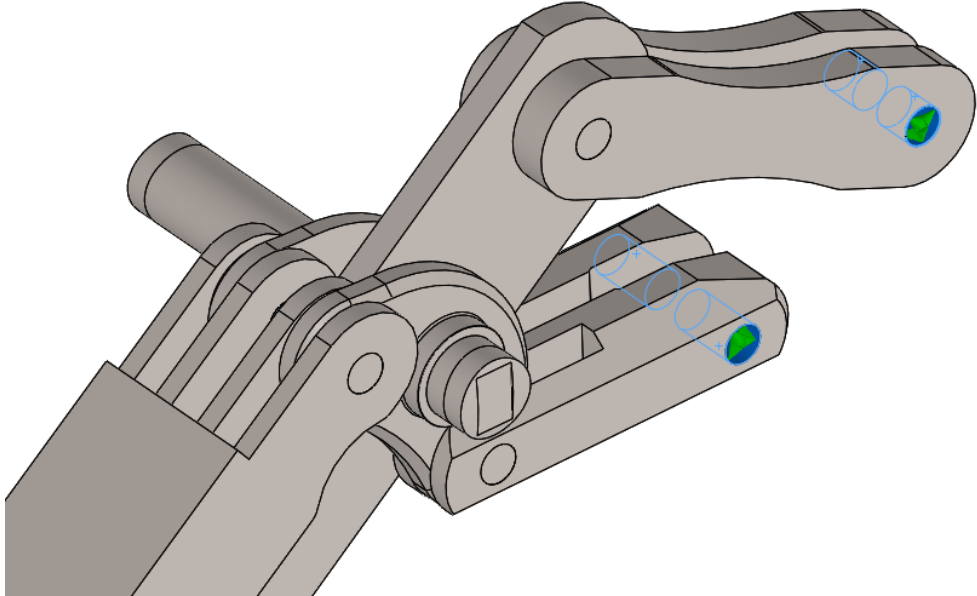


Figure B.4: Push rod links constraints. Constrained areas are highlighted in blue.

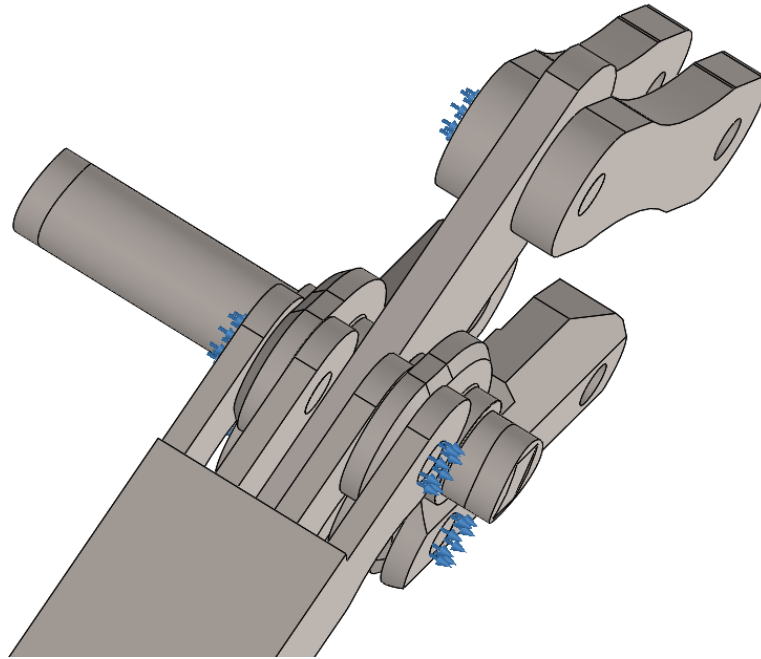


Figure B.5: Pin constraints that prevent lateral movement of the pins during simulation.

B.2 Support Shaft FEA Model

The FEA model was created by combining the sleeve, top cover, and base of the support shaft into one part. The shaft was constrained by applying a fixed geometry fixture at the end of the shaft where it would normally attach to the handle (Figure B.6). Loads were applied to the shaft using forces at the locations derived from FEA on the links. Stainless steel was used for the FEA model, and buckling and static simulations were completed using the same model constraints.

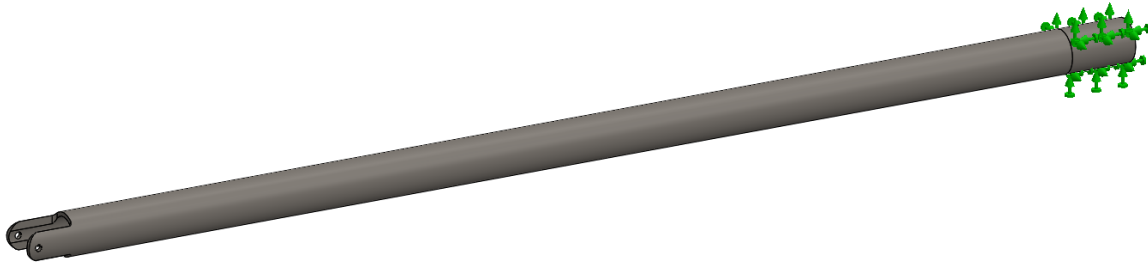


Figure B.6: Fixture location on the support shaft used in FEA.

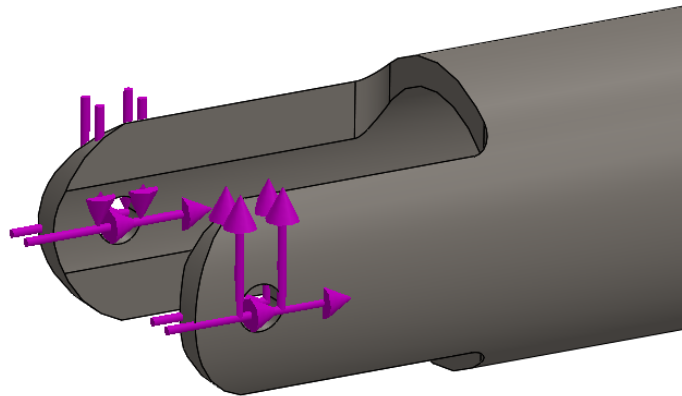


Figure B.7: Load direction and location on the support shaft.

B.3 Push Rod FEA Model

In order to properly model the push rod, split lines were used to divide the push rod surface into sections that correspond to the locations where guides support the rod. Figure B.8 shows the guide locations highlighted in blue. A cylindrical face fixture was applied at the guide locations to allow only translational and rotational motion along the center axis of the push rod, mimicking the support of the guides. The end of the push rod was fixed and loads calculated from the FEA on the links were placed at the pin location (Figure B.9). Stainless steel was used for the FEA model, and buckling and static simulations were completed using the same model constraints.

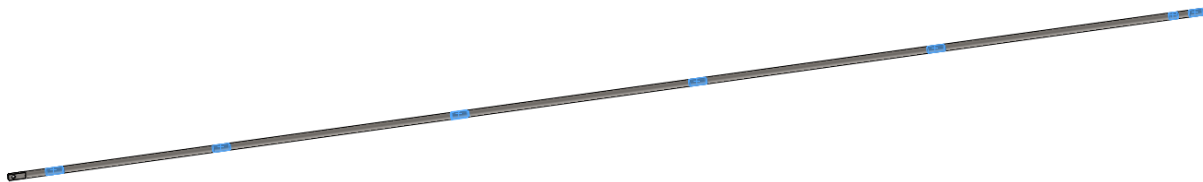


Figure B.8: Location of guides along the push rod (highlighted in blue).

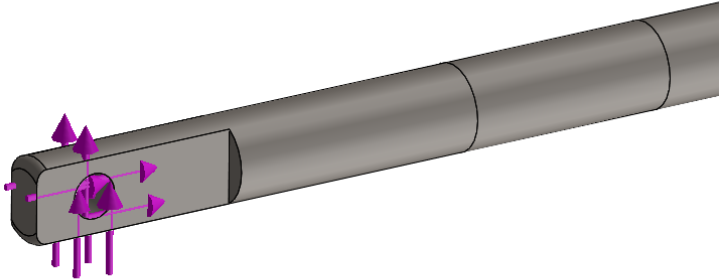


Figure B.9: Location and direction of loads applied to the push rod in the FEA.

Appendix C

Derivations for Kinematic Equations

C.1 Forward Kinematics

To derive the forward kinematics for jaw motion, a coordinate frame was constructed (Figure C.1), centered at the main support pin at the distal end of the instrument. Using lines to represent the links, a kinematic model for jaw position was created (Figures C.2 and C.3). For simplicity, only one jaw was modeled due to independent jaw movement.

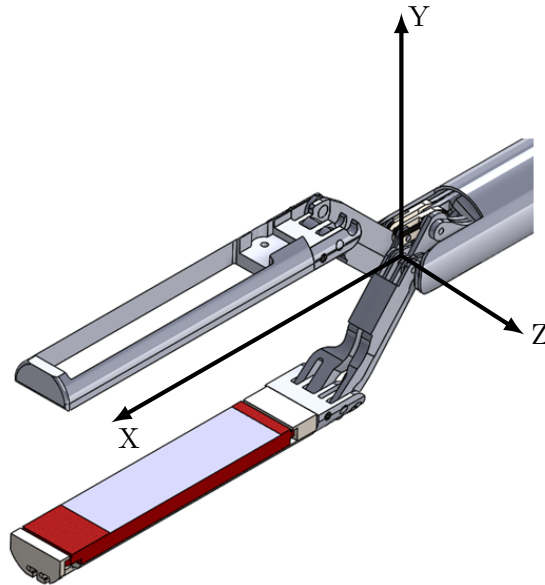


Figure C.1: Coordinate system for jaw mechanism.

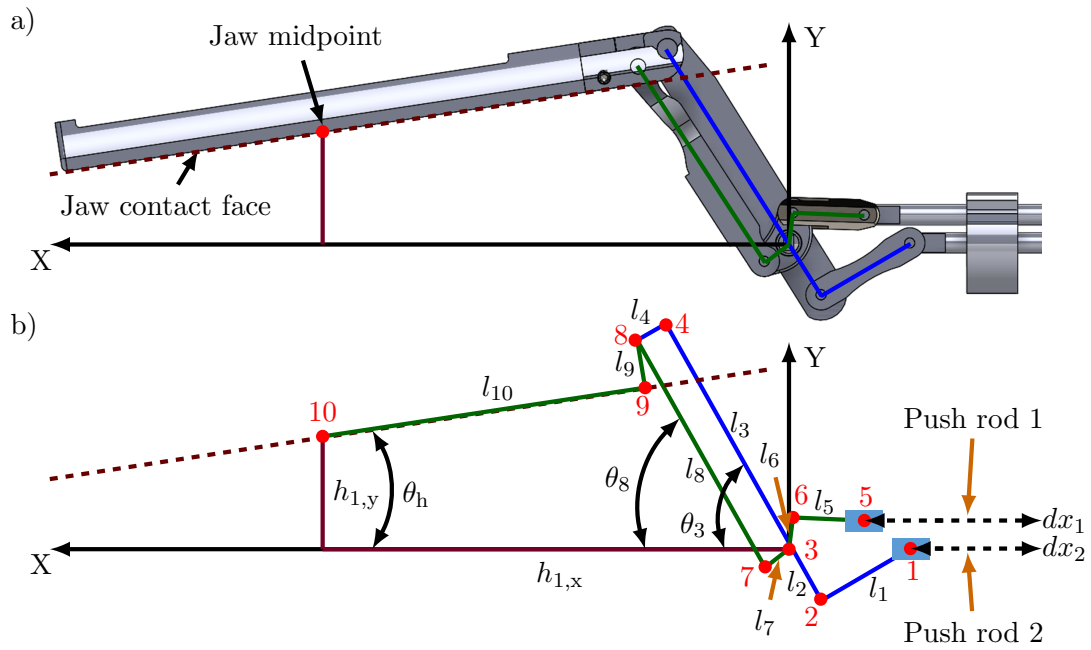


Figure C.2: Kinematic model of jaw mechanism: a) Conversion of the 3D link model to a 2D representation. b) Complete 2D kinematic model.

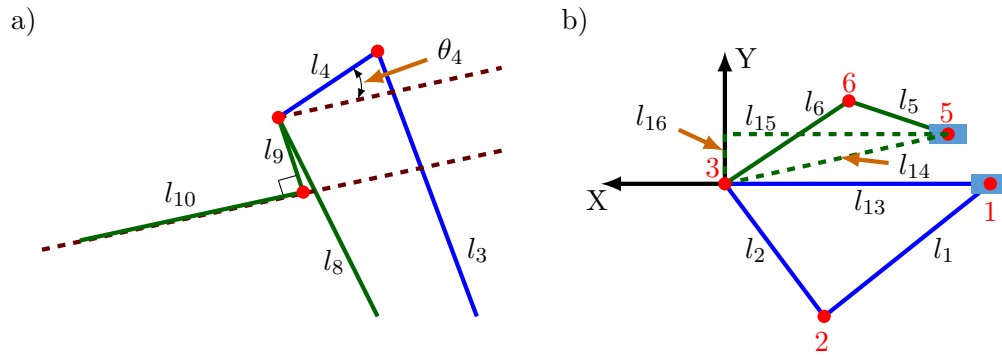


Figure C.3: a) Detailed view of Link 4 and 9 angles. b) Detailed view of push-rod links.

From the diagrams, the dependency of l_{15} on dx_1 and l_{13} on dx_2 can be determined:

$$l_{13} = 16 - dx_2$$

$$l_{15} = 9.6 - dx_1$$

To derive the forward kinematics equations, summation of the vertical components of vectors was conducted: $3 \rightarrow 4 \rightarrow 8 \rightarrow 9 \rightarrow 10$. The summation resulted in the following equation:

$$h_{1,y} = |l_3| \sin \theta_3 + |l_4| \sin (\theta_h - \theta_4) + |l_9| \sin (\theta_h - 90^\circ) + |l_{10}| \sin \theta_h$$

$$\therefore \theta_3 = \sin^{-1} \left(\frac{h_{1,y} - A \sin \theta_h + B \cos \theta_h}{|l_3|} \right) \quad (\text{C.1})$$

where $A = |l_4| \cos \theta_4 + |l_{10}|$, and $B = |l_4| \sin \theta_4 + |l_9|$. Using cosine law at node 1, we can derive an equation for $\theta_{1,13}$:

$$\theta_{1,13} = \cos^{-1} \left(\frac{l_{13}^2 + l_1^2 - l_2^2}{2l_1 l_{13}} \right) \quad (\text{C.2})$$

Next, using sine law at node 2:

$$\frac{\sin \theta_{1,2}}{l_{13}} = \frac{\sin \theta_{1,13}}{l_2}$$

$$\therefore \theta_{1,2} = 180^\circ - \sin^{-1} \left(\frac{\sqrt{4l_1^2 l_{13}^2 - (l_{13}^2 + l_1^2 - l_2^2)^2}}{2l_1 l_2} \right) \quad (\text{C.3})$$

From Equations (C.2) and (C.3), we are able to derive another equation for θ_3 :

$$\theta_3 = \theta_{2,13} = 180^\circ - \theta_{1,13} - \theta_{1,2}$$

$$\therefore \theta_3 = \sin^{-1}(D) - \cos^{-1}(C) \quad (\text{C.4})$$

where $C = \frac{l_{13}^2 + l_1^2 - l_2^2}{2l_1 l_{13}}$ and $D = \frac{\sqrt{4l_1^2 l_{13}^2 - (l_{13}^2 + l_1^2 - l_2^2)^2}}{2l_1 l_2}$. In order to relate the outputs to both inputs, summation along $3 \rightarrow 7 \rightarrow 8 \rightarrow 9 \rightarrow 10$ is required:

$$h_{1,y} = |l_7| \sin \theta_7 + |l_8| \sin \theta_8 + |l_9| \sin (\theta_h - 90^\circ) + |l_{10}| \sin \theta_h$$

$$\therefore \theta_8 = \sin^{-1} \left(\frac{h_{1,y} - |l_7| \sin \theta_7 + |l_9| \cos \theta_h - |l_{10}| \sin \theta_h}{|l_8|} \right) \quad (\text{C.5})$$

However, since θ_7 is a variable, it is required to determine its relationship to input dx_1 . Using simple trigonometry at node 3, we can derive the relationship between $\theta_{13,14}$ and the input:

$$\theta_{13,14} = \tan^{-1} \left(\frac{l_{16}}{l_{15}} \right) \quad (\text{C.6})$$

Using the cosine law at node 3, we can also derive the relationship between $\theta_{6,14}$ and input:

$$\theta_{6,14} = \cos^{-1}(E) \quad (C.7)$$

where $E = \frac{l_6^2 + l_{15}^2 + l_{16}^2 - l_5^2}{2l_6\sqrt{l_{15}^2 + l_{16}^2}}$. We can now use Equations (C.6) and (C.7) to find θ_7 :

$$\theta_7 = 180^\circ - \theta_{13,14} - \theta_{6,14} + 225^\circ$$

$$\therefore \theta_7 = 405^\circ - \tan^{-1}\left(\frac{l_{16}}{l_{15}}\right) - \cos^{-1}(E) \quad (C.8)$$

Substituting (C.8) into (C.5) yields our final answer for θ_8 :

$$\theta_8 = \sin^{-1}\left(\frac{h_{1,y} - |l_7| \sin \theta_F + |l_9| \cos \theta_h - |l_{10}| \sin \theta_h}{|l_8|}\right) \quad (C.9)$$

where $\theta_F = \theta_7 = 405^\circ - \tan^{-1}\left(\frac{l_{16}}{l_{15}}\right) - \cos^{-1}(E)$.

Before the equations can be solved, it is required to relate θ_8 to dx_2 . Horizontal components of vectors are summed: $3 \rightarrow 7 \rightarrow 8 = 3 \rightarrow 4 \rightarrow 8$

$$|l_3| \cos \theta_3 + |l_4| \cos(\theta_h - \theta_4) = |l_7| \cos \theta_7 + |l_8| \cos \theta_8$$

$$\therefore \theta_8 = \cos^{-1}\left(\frac{(|l_3| \cos \theta_3 + |l_4| \sin(\theta_h) \sin(\theta_4) + |l_4| \cos(\theta_h) \cos(\theta_4) - |l_7| \cos \theta_F)}{|l_8|}\right) \quad (C.10)$$

In order to obtain our first equation for $h_{1,y}$ we can equate (C.1) and (C.4):

$$\sin^{-1}\left(\frac{h_{1,y} - A \sin \theta_h + B \cos \theta_h}{|l_3|}\right) = \sin^{-1}(D) - \cos^{-1}(C)$$

$$\therefore h_{1,y} = |l_3| \sin \theta_G + A \sin \theta_h - B \cos \theta_h \quad (C.11)$$

where $\theta_G = \theta_3 = \sin^{-1}(D) - \cos^{-1}(C)$.

To get our second equation, we can equate (C.9) and (C.10):

$$\sin^{-1}\left(\frac{h_{1,y} - |l_7| \sin \theta_F + |l_9| \cos \theta_h - |l_{10}| \sin \theta_h}{|l_8|}\right) = \cos^{-1}\left(\frac{(|l_3| \cos \theta_3 + |l_4| \sin(\theta_h) \sin(\theta_4) + |l_4| \cos(\theta_h) \cos(\theta_4) - |l_7| \cos \theta_F)}{|l_8|}\right)$$

$$\therefore h_{1,y} = \sqrt{l_8^2 - (|l_4| \sin \theta_h \sin \theta_4 + |l_4| \cos \theta_h \cos \theta_4 + I)^2} - |l_9| \cos \theta_h + |l_{10}| \sin \theta_h + H \quad (C.12)$$

where $H = |l_7| \sin \theta_F$ and $I = |l_3| \cos G - |l_7| \cos \theta_F$. We can now equate (C.11) and (C.12) to achieve a relation for θ_h :

$$|l_3| \sin \theta_G + A \sin \theta_h - B \cos \theta_h = \sqrt{l_8^2 - (|l_4| \sin \theta_h \sin \theta_4 + |l_4| \cos \theta_h \cos \theta_4 + I)^2} - |l_9| \cos \theta_h + |l_{10}| \sin \theta_h + H$$

$$\therefore 0 = \sqrt{l_8^2 - (M \sin \theta_h + N \cos \theta_4 + I)^2} - K \sin \theta_h + I \cos \theta_h + J \quad (\text{C.13})$$

where $J = H - |l_3| \sin \theta_G$, $K = |l_{10}| - A$, $L = B - |l_9|$, $M = |l_4| \sin \theta_4$, and $N = |l_4| \cos \theta_4$. With expressions for $h_{1,y}$ and θ_h we can determine the horizontal position of the jaw midpoint, $h_{1,y,x}$, by adding vectors

3 → 4 → 8 → 9 → 10:

$$h_{1,x} = |l_3| \cos \theta_3 + |l_4| \cos (\theta_h - \theta_4) + |l_9| \cos (\theta_h - 90^\circ) + |l_{10}| \cos \theta_h$$

$$\therefore h_{1,x} = O \sin \theta_h + P \cos \theta_h + Q \quad (\text{C.14})$$

where $O = |l_4| \sin \theta_4 + |l_9|$, $P = |l_4| \cos \theta_4 + |l_{10}|$, and $Q = |l_3| \cos \theta_3$. The midpoint of the jaw was arbitrarily selected for purposes of kinematic equation derivation. Any point along the surface of the jaw can be selected.

C.1.1 Forward Kinematic Model Summary

The work in this section shows the derivation of three main equations that can be used to model jaw motion:

$$\sqrt{l_8^2 - (M \sin \theta_h + N \cos \theta_4 + I)^2} - K \sin \theta_h + I \cos \theta_h + J = 0$$

$$h_{1,y} = |l_3| \sin \theta_G + A \sin \theta_h - B \cos \theta_h$$

$$h_{1,x} = O \sin \theta_h + P \cos \theta_h + Q$$

Table C.1 provides a summary of all the constants and variables.

Table C.1: Summary of variables and constants that can be used to solve the kinematic equations.

Constants		Variables	
Symbol	Value	Symbol	Expression
l_1	10.09 mm	l_{13}	9.6 mm - dx_1
l_2	6.00 mm	l_{15}	16 mm - dx_2
l_3	22.50 mm	C	$\frac{l_{13}^2 + l_1^2 - l_2^2}{2l_1 l_{13}}$
l_4	3.36 mm	D	$\frac{\sqrt{4l_1^2 l_{13}^2 - (l_{13}^2 + l_1^2 - l_2^2)^2}}{2l_1 l_2}$
l_5	7.00 mm	E	$\frac{l_6^2 + l_{15}^2 + l_{16}^2 - l_5^2}{2l_6 \sqrt{l_{15}^2 + l_{16}^2}}$
l_6	3.00 mm	θ_F	$405^\circ - \tan^{-1}\left(\frac{l_{16}}{l_{15}}\right) - \cos^{-1}(E)$
l_7	3.00 mm	θ_G	$\sin^{-1}(D) - \cos^{-1}(C)$
l_8	22.80 mm	H	$ l_7 \sin \theta_F$
l_9	1.73 mm	I	$ l_3 \cos \theta_G - l_7 \cos \theta_F$
l_{10}	31.47 mm	J	$H - l_3 \sin \theta_G$
l_{16}	2.75 mm	Q	$ l_3 \cos \theta_G$
θ_4	22.75°		
A	34.57 mm		
B	3.03 mm		
K	-3.10 mm		
L	1.30 mm		
M	1.30 mm		
N	3.10 mm		
O	3.03 mm		
P	34.57 mm		

C.1.2 Forward Kinematic Model Validation

The governing equations for jaw motion were validated using a graphical solution created in SolidWorks. The following parameters were defined in SolidWorks to produce the jaw configuration in Figure C.4: $dx_1 = 2$, and $dx_2 = 1$.

Solving for all the variables (Table C.2) yields the following form of Equation C.13:

$$0 = \sqrt{(519.84 - (1.30 \sin \theta_h + 3.10 \cos \theta_h + 17.394)^2} - 3.10 \sin \theta_h + 1.30 \cos \theta_h - 12.15 \quad (C.15)$$

Numerically solving Equation (C.15) yields two sets of solutions:

$$\text{Solution 1: } \theta_h = [2(\pi n - 0.071) \left(\frac{180}{\pi}\right)]^\circ = -8.09^\circ, 351.91^\circ \dots$$

$$\text{Solution 2: } \theta_h = [2(\pi n + 1.077) \left(\frac{180}{\pi}\right)]^\circ = 123.34^\circ, 483.45^\circ \dots$$

where n is any real whole number.

We can further relate θ_h to dx_2 using the graphical solution, based on mechanical stops within the instrument, $7.87^\circ \leq \theta_3 \leq 66.10^\circ$. Therefore, all the possible positions for the jaw can be determined (Table C.3).

Furthermore, to prevent link collision, dx_2 needs to be limited to $0 \text{ mm} \leq dx_2 \leq 1.75 \text{ mm}$, while dx_1 needs to be limited to $0.20 \text{ mm} \leq dx_1 \leq 5.1 \text{ mm}$. Thus, θ_3 and θ_h are limited to:

$$14^\circ \leq \theta_3 \leq 66.10^\circ, \theta_h \leq 13.01^\circ, \theta_h \geq 332.55^\circ.$$

These limits still allow the palpation of tissue of 5 mm in thickness.

Based on the established limits, it can be concluded that the solution is: $\theta_h = 351.91^\circ$. We can now solve for $h_{1,y}$ using Equation (C.11) and $h_{1,x}$ using Equation (C.14): $h_{1,y} = 2.64 \text{ mm}$, and $h_{1,x} = 53.68 \text{ mm}$.

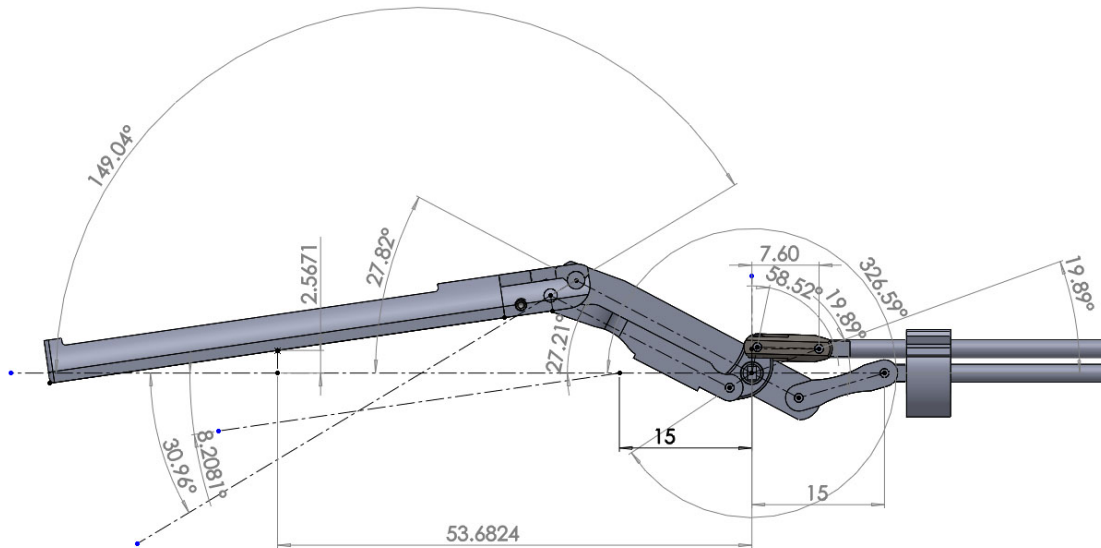


Figure C.4: Graphical solution in SolidWorks.

Table C.2: Summary of constants and variables used in kinematic model validation.

Variable	Expression	Value
l_{13}	$9.6 \text{ mm} - dx_1$	7.60 mm
l_{15}	$16 \text{ mm} - dx_2$	15.00 mm
C	$\frac{l_{13}^2 + l_1^2 - l_2^2}{2l_1 l_{13}}$	0.96
D	$\frac{\sqrt{4l_1^2 l_{13}^2 - (l_{13}^2 + l_1^2 - l_2^2)^2}}{2l_1 l_2}$	0.69
E	$\frac{l_6^2 + l_{15}^2 + l_{16}^2 - l_5^2}{2l_6 \sqrt{l_{15}^2 + l_{16}^2}}$	0.52
θ_F	$405^\circ - \tan^{-1}\left(\frac{l_{16}}{l_{15}}\right) - \cos^{-1}(E)$	326.59°
θ_G	$\sin^{-1}(D) - \cos^{-1}(C)$	27.82°
H	$ l_7 \sin$	-1.65 mm
I	$ l_3 \cos \theta_G - l_7 \cos \theta_F$	17.39 mm
J	$H - l_3 \sin \theta_G$	-12.15 mm
Q	$ l_3 \cos \theta_G$	19.90 mm

Table C.3: Range of angles and push rod positions.

dx_2 position (mm)	Angle range with varying θ_3
0–0.3	$336.07 \leq \theta_h \leq 347.07$
0.3–0.8	$175.45 \leq \theta_h, \theta_h \geq 341.32$
0.8–1.3	$175.45 \leq \theta_h, \theta_h \geq 350.05$
1.3–1.8	$14.04 \leq \theta_h, \theta_h \geq 358.95$
1.8–2.3	$8.21 \leq \theta_h \leq 25.81$
2.3–2.8	$6.44 \leq \theta_h \leq 47.90$

C.2 Inverse Kinematics

Using Equations (C.11), (C.12) and (C.13), derived in Section C.1, and the angular position and height of the jaw, push rod positions can be determined. Based on these equations, we have the following constants: A, B, K, L, M, N . We can then solve for θ_G using Equation (C.11):

$$\theta_G = \sin^{-1} \left(\frac{h_{1,y} + B \cos \theta_h - A \sin \theta_h}{|l_3|} \right) \quad (C.16)$$

We can use the equation for constant θ_G to create a numerical solution for l_{13} :

$$\begin{aligned} \sin^{-1} \left(\frac{h_{1,y} + B \cos \theta_h - A \sin \theta_h}{|l_3|} \right) &= \cos^{-1} \left(\frac{\sqrt{4l_1^2 l_{13}^2 - (l_{13}^2 + l_1^2 - l_2^2)^2}}{2l_1 l_2} \right) + \sin^{-1} \left(\frac{l_{13}^2 + l_1^2 - l_2^2}{2l_1 l_{13}} \right) \\ \therefore \frac{h_{1,y} + B \cos \theta_h - A \sin \theta_h}{|l_3|} &= \frac{\sqrt{4l_1^2 l_{13}^2 - (l_{13}^2 + l_1^2 - l_2^2)^2} \left(l_{13}^2 + l_1^2 - l_2^2 - \sqrt{4l_1^2 l_2^2 - 4l_1^2 l_{13}^2 + (l_{13}^2 + l_1^2 - l_2^2)^2} \right)}{4l_1^2 l_2 l_{13}} \end{aligned} \quad (C.17)$$

To solve for l_{15} , I and J are substituted into (C.13) and the equation is numerically solved for θ_F :

$$0 = \sqrt{(l_8^2 - (M \sin \theta_h + N \cos \theta_h + |l_3| \cos \theta_G - |l_7| \cos \theta_F)^2)} + K \sin \theta_h + L \cos \theta_h + |l_7| \sin \theta_F - |l_3| \sin \theta_G \quad (C.18)$$

With a value for θ_F , the expression for θ_F from Table C.2 can be used to determine l_{15} :

$$\begin{aligned} \theta_F &= 405^\circ - \tan^{-1} \left(\frac{l_{16}}{l_{15}} \right) - \cos^{-1} \left(\frac{l_6^2 + l_1 5^2 + l_1 6^2 - l_5^2}{2l_6 \sqrt{l_{15}^2 + l_{16}^2}} \right) \\ \therefore 0 &= \left(\left(\frac{l_{16}}{l_{15}} \right)^2 + 1 \right) (l_6^2 + l_{15}^2 + l_{16}^2 - l_5^2)^2 \\ &\quad - 4l_6^2 (l_{15}^2 + l_{16}^2) \left(\left(\frac{l_{16}}{l_{15}} \right) \sin(405^\circ - \theta_F) + \cos(405^\circ - \theta_F) \right)^2 \end{aligned} \quad (C.19)$$

C.2.1 Inverse Kinematic Model Validation

To validate the inverse kinematic equations, the calculated θ_h and $h_{1,y}$ from Section C.1.2 were used to determine the input parameters dx_1 and dx_2 . Using these values, the variable θ_G can be calculated and Equation (C.17) can be used to determine l_{13} . Numerical approximation of the solution results in two possible solutions, 9.2 mm and 15 mm. Based on motion limits discussed in Section C.1.2, the minimum value for l_{13} is 10.9 mm, thus our solution for l_{13} is 15 mm. Next, Equation (C.18) is solved to acquire the following numerical solutions:

Solution 1: $2(\pi n - 0.292)$, or $-33.4^\circ, 326.6^\circ \dots$

Solution 2: $2(\pi n + 0.659)$, or $75.5^\circ, 435.5^\circ \dots$

where n is any real whole number. From the graphical solution, it was determined that the range of θ_7 is: $311.26^\circ \leq \theta_7 \leq 346.16^\circ$. Therefore the answer can be reduced to 326.6° .

Lastly, using Equation (C.19), the value of l_{15} can be numerically calculated. The numerical approximation yields two solutions: 3.48 mm and 7.6 mm. Since l_{15} ranges from 6.5 mm to 8.55 mm, our final answer is 7.6 mm. Therefore, the derived inverse kinematic equations can be accurately solved to determine push rod positions based on a desired jaw orientation.

VITA

Name: Doran Avivi

Post-secondary Education and Degrees: The University of Western Ontario
London, Ontario, Canada
2010–2014 B.E.Sc.,
Mechanical and Materials Engineering

Honours and Awards: NSERC Canada Graduate Scholarship Masters (CGS-M)
Western University
2014-2015

NSERC Undergraduate Student Research Award (USRA)
Western University
2012-2013

Related Work Experience: Teaching Assistant
MME 2204 – Thermodynamics I
MME 2259 – Product Design and Development
MSE 2202 – Mechatronic System Design
MSE 4499 – Mechatronics Design Project
The University of Western Ontario
2014–2015

Undergraduate Research Assistant
CSTAR
The University of Western Ontario
2012–2014